2018

Dynamic behavior of multifunction structural panels for multi-hazard mitigation

Hao Wu
Iowa State University

Dynamic behavior of multifunction structural panels for multi-hazard mitigation

by

Hao Wu

A dissertation submitted to the graduate faculty

in partial fulfillment of the requirements for the degree of

DOCTOR OF PHILOSOPHY

Major: Civil Engineering (Structural Engineering)

Program of Study Committee:
An Chen, Co-major Professor
Simon Laflamme, Co-major Professor
Jiehua Jay Shen
Bora Cetin
Liming Xiong

The student author, whose presentation of the scholarship herein was approved by the program of study committee, is solely responsible for the content of this dissertation. The Graduate College will ensure this dissertation is globally accessible and will not permit alterations after a degree is conferred.

Iowa State University

Ames, Iowa

2018

TABLE OF CONTENTS

Page

LIST OF FIGURES

Page

LIST OF TABLES

Page

NOMENCLATURE

α_i cross-section area proportion that the i^{th} LCVA shares in the middle horizontal column;
$\boldsymbol{\alpha}$ column spacing vector;
γ the vertical/horizontal length ratio;
η uniform head loss coefficient;
η_i head loss coefficient due to the i^{th} orifice;
μ head loss coefficient due to friction;
υ cross-section ratio of vertical columns to the horizontal column;
$\xi_s = c_s / 2m_s\omega_s$ the damping ratio of the structure;
ρ_l liquid density;
$\rho = \omega_f / \omega_s$ excitation frequency ratio;
γ mass ratio of TLMCD to the structure
$\chi_i = \omega_i / \omega_s$ the i^{th} tuning ratio of a TLMCD;
ψ orifice blocking ratio;
ψ_i blocking ratio of the i^{th} orifice between columns;
ω_f external excitation frequency;
ω_s the natural frequency of the SDOF structure;
ω_i the i^{th} natural frequency of a TLMCD.
A cross-section area of vertical columns;
$\mathbf{B}_d$ the force location matrix on the primary strucutre;
c_s the damping coefficient of the primary structure if it is SDOF;
$\mathbf{C}$ the mass matrix of the TLMCD-structure system;
$\mathbf{C}_C$ the damping matrix of the TLMCD;
$\mathbf{C}_C^{'}$ the linearized damping matrix of the TLMCD;
$\mathbf{C}_S$ the damping matrix of the primary structure;
$\mathbf{F}$ the force matrix acting on the primary structure;
g gravity acceleration;
h the initial liquid height of a TLMCD or LCVA;
H_1 transfter function for the SDOF structure dispalcement;
k_s the stiffness of the primary structure if it is SDOF;
$\mathbf{K}$ the stiffness matrix of the TLMCD-structure system;
$\mathbf{K}_C$ the stiffness matrix of the TLMCD;
$\mathbf{K}_S$ the stiffness matrix of the primary structure;
l the total horizontal length of a TLMCD or LCVA;
l_e the effective length of the i^{th} LCVA inside a TLMCD;
l_i the length of the i^{th} spacing between vertical columns;
m the number of DOFs in the primary structure;
m_d the total mass of TLMCD;
m_s the mass of the primary structure if it is SDOF;
$\mathbf{M}$ the mass matrix of the TLMCD-structure system;
$\mathbf{M}_C$ the mass matrix of the TLMCD;
$\mathbf{M}_S$ the mass matrix of the primary structure;
N the number of vertical columns;

p_0	the amplitude of excitation harmonic force;
Q_i	the total nonconservative force acting on the i^{th} DOF;
Q_{ei}	the inertia force due to ground excitation acting on the i^{th} DOF;
Q_{fi}	the damping force due to friction acting on the i^{th} DOF;
Q_{oi}	the damping force due to orifices acting on the i^{th} DOF;
t	time;
T	kinematic energy of the TLMCD system;
V	the potential energy of the TLMCD system;
$\mathbf{v}$	vector related to liquid velocity
W_e	the work done by the outside excitation force;
W_f	the work done by the damping force due to friction;
W_o	the work done by the damping force due to orifices;
χ_i	real displacement of the liquid surface in the i^{th} column;
$\ddot{x}_g$	floor acceleration from the structure;
x_s	displacement of the structure;

ACKNOWLEDGMENTS

Firstly, my sincere thanks go to Dr. An Chen, for his dedicated support along my PhD program, without whom, this dissertation would not have been possible. His keen attitude towards research, overwhelming attitude to teaching, and kindness to people inspired me throughout my study. My heartfelt gratitude go to Dr. Simon Laflamme for his guidance and support. His vast knowledge, diligent mentoring and timely advice are responsible for completing my work.

I would like to thank my committee members, Dr. Jiehua Jay Shen, Dr. Bora Cetin, and Dr. Liming Xiong, for their insightful comments and encouragement throughout the course of this research.

I would like to thank Douglas Wood, Owen Steffens for their help in preparing testing specimens. I would like to thank Dr. Jialai Wang and the lab staff at University of Alabama for their help in providing shake table test facilities.

In addition, I would also like to thank my friends and colleagues at Iowa State University: Dr. Mostafa Yossef, Connor Schaeffer, David Morandeira, Ahmed Alateeq, Jin Yan, Elizabeth Miller, Mohammed Bazroun, Yinglong Zhang, Dr. Liang Cao, Nazik Citir, Yongqiang Gong, Alessandro Cancelli and Laura Micheli.

The funding of this research program is provided by National Science Foundation under Grant No. CMMI-1562992. Their support is greatly appreciated.

Last but not the least, I would like to thank my parents for their spiritual support throughout the writing of my dissertation and my life in general.

ABSTRACT

In this study, a novel multifunctional panel that can resist structural loads, control room temperature and dissipate vibration energy due to wind or seismic hazard is proposed. All these functions are enabled by a liquid-filled multi-capillary structure inside the panel. The free-flowing liquid in the capillaries can provide thermal exchange from external sources and liquid head loss generation when it flows through internal orifices.

Two types of multifunctional panels, including a pultruded glass fiber-reinforced polymer (GFRP) panel and a reinforced concrete panel, are manufactured to assess their damping performances. Shake table tests on the GFRP multifunctional panel show that it has high resistance to ground accelerations but relatively low energy dissipation capability. Filled-in water can greatly reduce the GFRP panel's vibration through liquid damping, with reduction effect increasing with the water amount. Dynamic tests of reinforced concrete multifunctional panel also proved that the oscillating liquid inside can enhance the total damping of the structure.

The liquid motion in the multi-capillary system can be described as a tuned liquid multiple columns damper (TLMCD) model, a nonlinear dynamic model that simulates the liquid surface movement in each capillary. The friction damping and head loss damping due to the internal orifices are identified as the sources of energy dissipation in this system. Numerical solutions of the dynamic model are validated through both computational fluid dynamic (CFD) simulation and a series of dynamic tests of the manufactured reinforced concrete multifunctional panel. The nonlinear dynamic model is further linearized using energy equivalent method. Optimum parameters of a TLMCD

attached to various primary systems can be obtained from the linearized model, and transfer functions indicate that optimized TLMCDs have better damping performance than single or multiple tuned liquid column dampers (TLCDs) when mitigating multiple-degree-of-freedom (MDOF) primary structures.

Semi-active TLMCDs with controllable valves are proposed as well. Sliding mode control method is employed to calculate the control forces in a TLMCD. Study of a benchmark building equipped with a semi-active TLMCD under stochastic wind hazards show significant damping improvement from the passive TLMCDs.

CHAPTER 1. INTRODUCTION

1.1 The Concept of a Novel Multifunctional Panel

Modern buildings and structures raise more critical demands for structural members. Structural components not only need to ensure safety, but also need to environmentally friendly, comfortable and even intelligent. In this dissertation, we propose a novel multifunctional panel that integrates structural load resistance, adjustment of building temperature, and mitigation of lateral wind or earthquake hazards. The concept of the multifunctional panel is illustrated in Figure 1.1: the panel has a multi-capillary hollow section that can be filled with liquid (typically water), which is evenly distributed across the wall surface and can be charged or discharged based on room temperature. In addition, the internal water system also functions as a damper system that generates liquid head loss damping to dissipate vibration energy when the main structure experiences wind or seismic hazards. The main functions of the panel are introduced as the following.

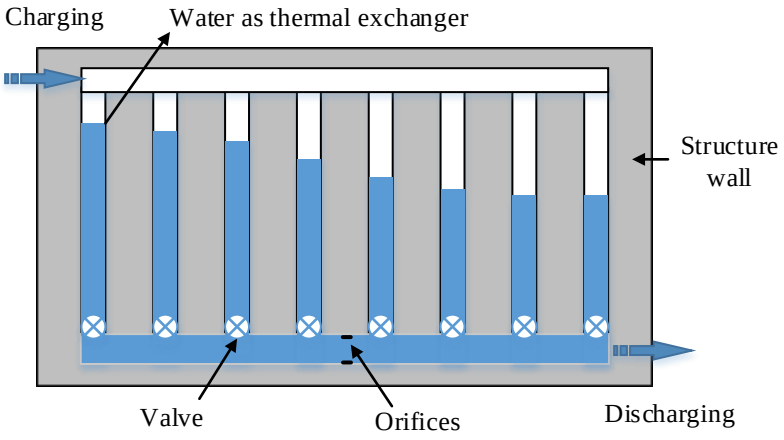

Figure 1.1 *The concept of a novel multifunctional panel*

1.1.1 Resisting structural load

Providing lateral and vertical load resistance is still the basic requirement of any load-bearing member in a structure. The novel multifunctional panel can function as a structure wall that resists dynamic and stationary structural loads including axial forces and shear forces transferred from other parts of the structure. The hollow multiple-capillary section design reduces the weight of panel and offers similar moment of inertia compared with a solid section of the same area at a cost of reduction of its strength and stiffness. Structural walls of similar sections, such as masonry walls constructed with hollow blocks (Thanoon et al. [1]), suggest that hollow sectioned walls can be both economical and efficient.

1.1.2 Preserving room temperature with water

Water has a much larger specific heat capacity than those of concrete and steel, which means that it will raise temperature slower than concrete and steel after absorbing the same amount of heat. This will make water an ideal type of thermal exchanger and storage. In fact, home heating by hot water circulation in a radiator is still practiced in some countries (Lu et al. [2]). The water that is charged/discharged based on room temperature can be heated or cooled by conventional heating/cooling equipment.

When the multifunctional panels are placed as the exterior walls, they can harvest on-site solar energy. Water-filled exterior walls can cool the house by absorbing the solar energy during the daytime and warm the room by releasing the stored solar energy at night. In fact, the idea of water-filled thermal walls can be probably dated back to 1947 when Hottel [3] and his students from Massachusetts Institute of Technology built a water wall with black-painted cans behind double pane glass. Since then commercial building systems featuring water wall have been developed (All-water ® Liquid-filled Walls [4], shown in Figure 1.2), claiming that the water system can shave up to 20 percent off a home's energy bills.

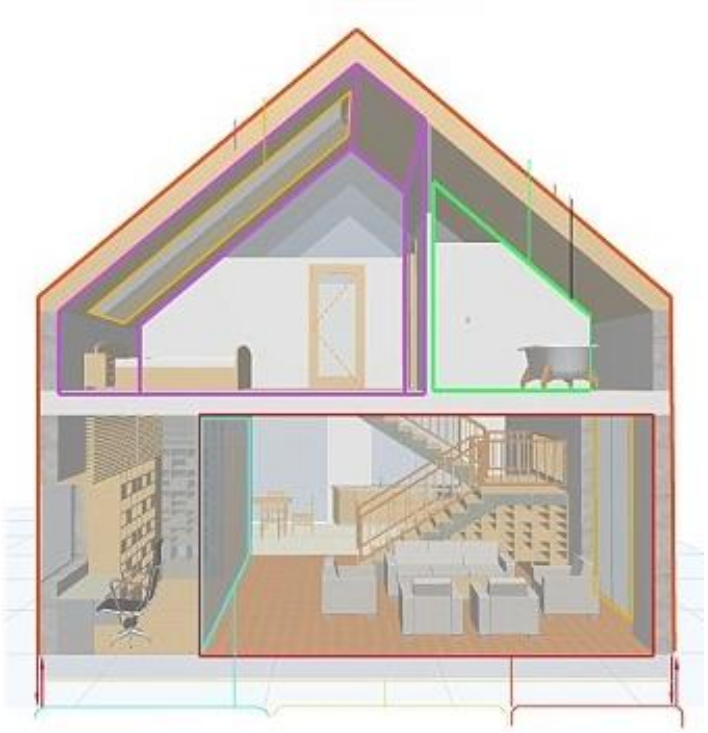

Figure 1.2 *All-water® Liquid-filled Walls [4]*

1.1.3 Suppressing structure vibration with liquid damping

Drastic changing of liquid flow will cause kinetic energy loss of the liquid, and the friction between liquid and its container could be another source of energy loss. Oscillating or sloshing liquid has been applied to dissipate vibration energy as early as 1966 when Abramson [5] used liquid damping to control motions in space satellites.

Attempts of including liquid dampers inside structural components came much later. In 2008, Ye et al. [6] proposed a novel cast-in-situ hollow floor slabs with an internal tuned liquid damper (TLD), which is illustrated in Figure 1.3. The design takes advantage of the high hollow volume ratio of modern hollow floor slabs and fills the hollow box with water. The water sloshing effect can raise the damping ratio of the structure by approximately 2%. Matia and Gat [7] studied an elastic beam embedded with a fluid-filled parallel-channel

network. Their findings indicate that solid-fluid interaction and the inertia effect will help eliminate the elastic beam's deformation caused by external dynamic forces.

The tuned liquid damping system in the multifunctional panel is different from the above ones. It involves water motion in a multi-capillaries system with relatively uniform liquid velocity profile in each capillary.

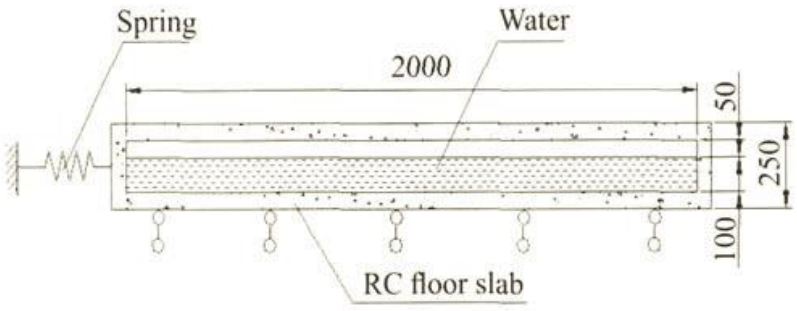

Figure 1.3 *Cast-in-situ hollow floor slabs with an internal tuned liquid damper (TLD) [6]*

1.2 Tuned Liquid Multiple Column Dampers

In design of multifunctional panels, it is vital to calculate the damping forces acting on the structures and predict the liquid motion in the internal multi-capillary system, which is also the most critical part of this dissertation.

The physical model describing the internal oscillating liquid system in the multifunctional panel can be termed as a tuned liquid multiple column damper (TLMCD), different from conventional TLCDs. Typical TLCDs are U-shaped tubes with filled-in oscillating liquid, and head loss damping is generated when liquid flow through the orifice in the horizontal part of the U-tube. TLCDs can resist horizontal vibrations transferred from the main structure due to wind or earthquake load. Compared to other mass dampers, TLCDs are easy to construct, have low maintenance cost and can provide a source of residential-use water [8]. Notable examples of TLCD in high-rise buildings include the 189 m One Madison

Park in New York City [9], the One Wall Center in Vancouver [10], and Elizabeth Street residential building in Melbourne [11], etc.

The main difference between a TLMCD and a TLCD is that a TLMCD has multiple vertical columns and multiple orifices in the horizontal column, which is depicted in Figure 1.4, compared to only two columns in a TLCD. The equations of motion for a TLMCD is more complex because it is a multiple-degree-of-freedom (MDOF) nonlinear system with coupling liquid motion in each vertical column. TLMCDs can offer more design parameters than TLCDs when they are tuned to specific main structures: a TLCD usually has only two parameters for design purpose while a N-column TLMCD has *2N*-1 parameters in total.

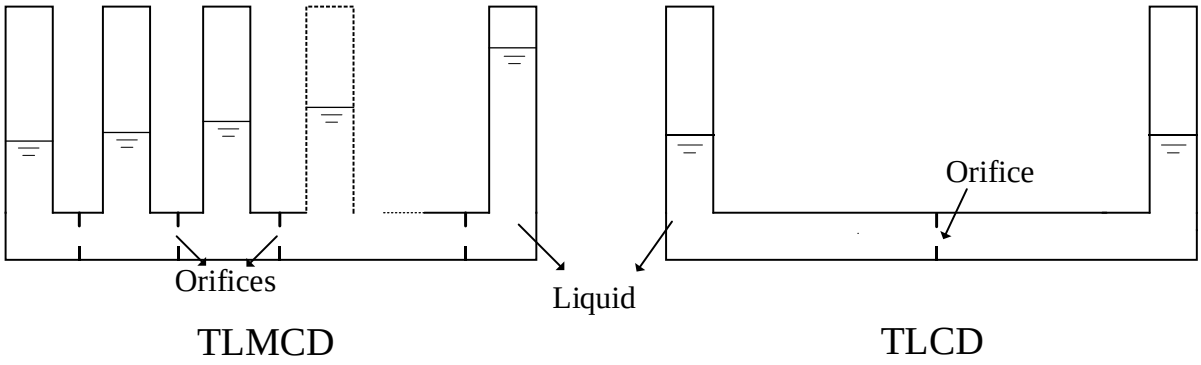

Figure 1.4 *Comparison between TLMCDs and TLCDs*

TLMCDs can address many shortcomings of conventional TLCDs:

(1) A TLCD has only one main natural frequency and thus only suppresses one vibration mode of the main structure. To reduce the vibration of more than one vibrations modes, multiple TLCDs (MTLCDs) are needed. Even MTLCDs may not be very efficient because only the TLCDs with frequencies that are within +/- 15% range of the external excitation frequency will be excited (Conner and Laflamme [12]), and all the other TLCDs

do not participate in suppressing the main structure's vibration. TLMCDs has multiple resonance frequencies and it can shift its frequencies to appropriate ranges accordingly when the vibration mode of the main structure changes.

(2) TLCDs often consume a large occupying space, which can be difficult to find in high buildings. TLMCDs' geometry indicate that it can insert more vertical columns between the two columns of a U-shaped TLCD, and consequently they can store more liquid within the same space (though at a slightly worse damping efficiency, this will be discussed in Chapter 6), which could be an advantage when the occupying space is concerned.

(3) TLCDs have a "detuning" problem. When the main structure's natural frequency is not accurately calculated or changes due to extreme hazards, the passive TLCD will not function very well since its effective frequency range is narrow. On contrast, a TLMCD has multiple resonance frequencies that can be provide wider effective frequencies ranges.

1.3 Objectives and Contributions

The objective of this study is to assess the dynamic load resistance and energy dissipation capability of the multifunctional panel. We manufactured two types of multifunctional panels: one is a pultruded GFRP panel with seven identical cells, and another is a reinforced concrete panel with an internal multiple tube system. Both panels have their own advantages. This dissertation consists of experimental tests on these two multifunctional panels and theoretical investigation of their damping performance that can model the liquid motion in each capillary as an individual movement.

The main contributions of this study include:

- Studied the seismic load resistance of hollow multi-capillary sectioned walls and compared it with that of conventional solid walls.

- Developed a nonlinear dynamic model that can describe liquid motion in a multi-capillary system; and validated this dynamic model through both shake table tests and numerical simulations;
- Developed a design procedure for optimum parameters of TLMCDs suppressing vibration of the primary structures.
- Extended the passive TLMCD design to semi-active cases where the orifice openings are controlled.

1.4 Dissertation Organization

The remaining dissertation is organized as the following:

Chapter 2 studies the dynamic behavior of a GFRP multi-capillary panel under seismic load through shaking table tests and Finite Element Analysis (FEA). A comparison of seismic performance between the GFRP panel and conventional solid reinforced concrete (RC) walls is conducted.

Chapter 3 investigates the enhanced damping effect of the same GFRP panel in Chapter 2 when it is filled water and adapted into a TLMCD. Different combinations of capillaries filled with water is tested under harmonic ground loadings.

Chapter 4 is the analytical modelling of the internal liquid motion in a multi-capillary system. The numerical solutions of the analytical model are verified by computational fluid dynamics (CFD) simulations.

Chapter 5 is a dynamic test of a fabricated RC multifunctional panel to further validate the analytical model in Chapter 4.

Chapter 6 is the theoretical investigation of the optimum parameters of TLMCDs suppressing primary structures' vibration.

Chapter 7 discusses the potential damping effect of the multifunctional panel when the orifices are semi-actively controlled.

Chapter 8 conclude the dissertation.

1.5 References

[1] Thanoon WA, Jaafar MS, Abdul Kadir MR, Abang Ali AA, Trikha DN, Najm AMS. Development of an innovative interlocking load bearing hollow block system in Malaysia. Constr Build Mater 2004;18:445–54. doi:10.1016/j.conbuildmat.2004.03.013.

[2] Lu Z, Zhang J, Chen Y, Zhao T, Liu H. Fuzzy control model and simulation of supply air system in a test rig of low-temperature hot-water radiator system. Energy Build 2010;42:386–92. doi:10.1016/j.enbuild.2009.10.006.

[3] Hottel, HC. The engineering utilization of solar energy. In Proc. of the American Academy of Arts and Sciences 1951,79(4): 313-318.

[4] http://www.dailymail.co.uk/sciencetech/article-3034093/The-house-WATER-Liquid-filled-walls-keeps-building-cool-warms-winter.html#ixzz5ElILNzDA

[5] Abramson, HN. The dynamics behavior of liquids in moving containers. NASA 1966, SP-106.

[6] Ye L, Lu X, Qu Z, Hou J. Distributed TLDs in RC floors and their vibration reduction efficiency. Earthq Eng Eng Vib 2008;7:107–12. doi:10.1007/s11803-008-0751-9.

[7] Matia Y, Gat AD. Dynamics of Elastic Beams with Embedded Fluid-Filled Parallel-Channel Networks. Soft Robot 2015;2:42–7. doi:10.1089/soro.2014.0020.

[8] Spencer BF, Nagarajaiah S. State of the Art of Structural Control. J Struct Eng 2003;129:845–56. doi:10.1061/(ASCE)0733-9445(2003)129:7(845).

[9] http://www.ctbuh.org/TallBuildings/FeaturedTallBuildings/Archive2010/OneMadisonParkNewYorkCity/tabid/2549/language/en-GB/Default.aspx

[10] https://www.canadianconsultingengineer.com/features/buildings-one-wall-centre-vancouver/

[11] https://www.wsp.com/en-GL/projects/450-elizabeth-street

[12] Connor J, Laflamme S. Structural motion engineering, Springer, New York, 2014.

CHAPTER 2. SEISMIC BEHAVIOR OF GALSS FIBER-REINFORCED POLYMER WALL PANELS

A paper published by *Composite Structures*

Hao Wu, An Chen, Simon Laflamme

2.1 Abstract

Glass fiber-reinforced polymer (GFRP) panels have been increasingly used for structural applications due to their light weight, corrosion resistance and construction-easiness. This study evaluates the seismic performance of GFRP wall panels based on comprehensive shaking table tests and Finite Element Analysis (FEA). A GFRP wall panel is experimentally subjected to harmonic ground motions of frequencies ranging from 10 to 15 Hz. A mass is attached to the top of the panel to simulate gravitational weight. The panel remains undamaged under a peak base acceleration of 2.1 g. Its FEA is conducted using Abaqus based on Rayleigh damping. There is a good correlation between the experimental and FEA results. Another FEA model is developed to study the seismic behavior of a Reinforced Concrete (RC) wall, which is validated by results from an existing study. The two FEA models are then used to compare the seismic performance of GFRP wall panels versus RC walls in terms of drift ratio and hysteretic behavior. It is found that while GFRP wall panels cannot replace RC walls in multi-story buildings due to their low stiffness, their performances are comparable to RC walls for low-rise buildings. Therefore, GFRP wall panels can be potentially used in low-rise buildings in seismic regions.

Keywords: Fiber-Reinforced Polymer (FRP), Wall panel, seismic behavior, shaking table test, finite element modeling, reinforced Concrete wall

2.2 Introduction

Fiber-reinforced polymer (FRP) materials have been widely used in civil engineering. While they are more commonly used to strengthen existing structures [1,2], FRP components have gained popularity in recent years because they are easy to retrofit and reduce the overall self-weight of the structure, yielding design flexibility. While early research work mainly focused on the static behavior of FRP (e.g., Clarke [3]; Davalos et al. [4]), there has been some recent studies on their dynamic behavior through analytical and experimental investigations [5–8]. In particular, Mosallam et al. [9] conducted a comprehensive study on the pultruded GFRP beam-to-column connections under both static and dynamic loads, suggesting that GFRP connections could be modeled as semi-rigid in frame analysis. Boscato and Russo [10–12] used the free vibration response of a large FRP space frame to identify its structural information including fundamental frequencies, mode shapes and damping coefficients. Yang et al. [13] researched the dynamic and fatigue performances of a pultruded FRP frame, concluding that FRP components showed no significant degradation after 2.1 million cycles of fatigue load. Bai and Keller [14] studied the dynamic structural response of an all-FRP pedestrian bridge under impact and human walking excitations with output-only identification techniques. More recently, Zhang et al. [15] investigated the cyclic performance of tubular FRP beam-column bonded sleeve connections, which could achieve good ductility and energy dissipation capacity; Ding et al. [16] applied a constant axial load and a cyclic lateral load to composite frames and achieved satisfactory seismic performance. While these studies represent pioneer work in furthering the understanding of the dynamic behavior of FRP components, to the best of the authors' knowledge, the seismic behavior of FRP panels as load-bearing walls is yet to be studied. Previously, FRP panels were mainly for bridge decks and building floors. For example, Zi et al. [17] proposed a GFRP deck panel

with rectangular holes filled with foam to improve deck strength and stiffness. Satasivam et al. [18–21] conducted research on modular FRP sandwich panels for building floors, which consisted of FRP pultruded boxes bonded with two GFRP plates. The authors demonstrated that foam filling, adhesive bonding, and bidirectional pultrusion orientation improved the flexural load-bearing capacity of the panels. The FRP sandwich panels could also be bolted to steel beams to form composite beam and slab systems. In this study, the authors investigate FRP panels as structural walls, where the axial and shear loading capacity of FRP panels is of interest. Reinforced Concrete (RC) shear wall is the most widely used wall type to resist lateral loads. Extensive research on the seismic performance of RC walls has been conducted experimentally [22,23] and numerically [24]. The inelastic seismic response of RC walls is complex because it includes multiple vibration modes in the nonlinear range, the post-elastic behavior of concrete and steel under dynamic loading, and the interactions among flexural, shear, and axial cyclic loadings. Compared to traditional RC walls, FRP wall panels have some advantages. Due to their high strength-to-weight ratio, easy application, and resistance to corrosion, FRP materials have been applied to enhance existing structural walls' strength and ductility [25]. However, unlike RC walls, FRP wall panels do not yield and have relatively low stiffness. A question arises whether FRP panels are suitable for seismic mitigation, and how their performance would compare with RC walls. Shaking table testing is often recognized as the most suitable experimental method for reproducing the effects of earthquakes on structural members. In this paper, the dynamic behavior of a pultruded GFRP wall panel exposed to seismic loads is experimentally studied through a shaking table test. Results from the laboratory tests are used to model the behavior of GFRP units, which are used to compare the seismic performance of GFRP wall panels with that of

structural RC shear walls. The rest of the paper is organized as follows. Section 2 describes the GFRP panel used in the laboratory and reports mechanical properties obtained experimentally from the static and free vibrations tests. Section 3 reports the results from the laboratory testing of a GFRP wall panel exposed to harmonic ground motions using a shaking table. Section 4 compares the dynamic characteristics of the wall obtained through free vibration and shaking table tests with the results from the FEA analysis. Section 5 creates and validates an FEA model of an RC wall, and uses this model to compare the response of RC walls with that of GFRP walls under seismic loads. Section 6 concludes the paper by discussing results and potential applications of GFRP structures.

2.3 GFRP Panel Properties

The panel used in this study is a Composolite® building panel provided by Strongwell®. It is 61 cm wide by 122 cm long made of glass fiber using a pultrusion process. The geometry of the panel is shown in Figure 2.1. The manufacturer's values of out-of-plane and in-plane moment of inertia are 6.62 $\times 10^2$ cm^4 and 176 $\times 10^2$ cm^4, respectively. The thickness of the GFRP panel is 0.297 cm for the outer wall, and 0.218 cm for the separation between the cells. The weight of the whole panel is 13.6 kg.

Two static tests are conducted to determine the lateral stiffness of the GFRP panel. The first test is a pushover test, as schematized in Figure 2.2a, where the bottom of the panel is fixed to the ground, and an increasing concentrated force is exerted at the top of the panel. The displacement at the top is recorded by a Linear Variable Differential Transformer (LVDT) with an MEGADAC data acquisition system at a sampling rate of 2000 Hz. The second test consists of a three-point bending test, as schematized in Figure 2.2b. The panel is configured as a simply supported beam, and a concentrated force is applied at mid-span,

where another LVDT is installed. The lateral and bending stiffnesses are calculated from the force-displacement relationship using Eqs. (1) and (2), respectively:

$$EI = \frac{Pl^3}{48\delta} \tag{2-1}$$

$$EI = \frac{Pl^3}{3\delta} \tag{2-2}$$

where EI is the in-plane stiffness calculated from the push-over test or three-point bending test, P is the force applied at the top or middle of the panel, δ is the displacement under that force, and L is the vertical length of the panel, as illustrated in Figure 2.2. Table 2.1 lists the results, compared with properties reported by the manufacturer. The test results are lower than manufacturer's data because the width versus length ratio of the panel is not small enough to be treated as a beam and the plain-section assumption may not be totally valid. Nevertheless, an average value of 5.56 GPa between the pushover and three-point bending test is taken as the component's stiffness. Other GFRP wall's structural characteristics including lateral strength, Young's elastic modulus, and Poisson's ratio are reported by the manufacturer as 169 MPa, 6.10 GPa, and 0.27, respectively.

The GFRP panel is viewed as a load-bearing wall. A steel block is connected by steel angles to the wall to simulate the seismic weight at the top, as illustrated in Figure 2.3. This seismic weight corresponds to a flat roof of a typical low-rise building, including the total dead load of the roof and 20% of snow load:

$$W = \frac{\left[DL + 20\%\left(SL\right)\right]A_t}{S_l^2} \tag{2-3}$$

where W is the attached seismic weight, DL is the dead load, SL is the snow load, A_t is the total tributary area, and S_l is the length scale factor, as listed in Table 2.2.

Free vibration tests are conducted to obtain the modal frequencies and damping ratios of the GFRP panel. The bottom of the wall panel is rigidly fixed to the ground, and a plastic hammer is used to excite the panel at random locations. An LVDT and an accelerometer are installed at the top of the panel to record its displacement and acceleration in the lateral direction. The sampling rate for all sensors is 2000 Hz. By analyzing the displacement reponse in the frequency domain, as illustrated in Figure 2.4, the first natural frequencies of the GFRP panel with and without the attached seismic weight can be identified as 47 Hz and 117 Hz, respectively. These results are consistent with analytical results obtained assuming the GFRP panel as a cantilever beam, which can be predicted by Equations (2.4) and (2.5) (Voltera and Zachmanoglou [26]) for the cases with and without seismic weight, respectively, where l is the vertical length of the panel, EI is the in-plane stiffness, m is the mass of the panel, and m_1 is the seismic weight on the top. The first vibration mode shape is similar to a uniform continuous beam under bending, where the deformation increases quadratically with the distance from the base.

$$f_1 = \frac{1}{2\pi}\frac{6.088}{l}\sqrt{\frac{EI}{(3m+12.355m_1)l}} = 48\text{Hz} \tag{2-4}$$

$$f_1^{'} = \frac{1}{2\pi}3.515\sqrt{\frac{EI}{ml^3}} = 128\text{Hz} \tag{2-5}$$

The damping ratio of the structure's first mode is determined by computing the decay of the top displacement after the first ten cycles. It is found to be 0.6%, which is relatively small compared to typical damping ratios for RC (5%) and steel structures (2%).

2.4 Shaking Table Test

The performance of the GFRP panel under seismic excitation is evaluated through a shaking table test. The configuration of the test is shown in Figure 2.5. The GFRP panel is

connected to the shaking table using bolts and angles to simulate a rigid connection. The size of the angles is 10 x 10 cm, and the bolt and angle system effectively constrains the rotation in the out-of-plane direction. Both tests with and without attached mass are conducted to evaluate the dynamic responses of the wall panel.

The shaking table can generate harmonic ground motions with a frequency ranging from 10 to 60 Hz. But in the test, the GFRP panel is subjected to two harmonic ground motions in the in-plane direction, as described in Table 2.3, since ground motions with frequencies higher than 15.1 Hz will generate accelerations greater than 3 g, which would be too high for simulating real seismic ground motions. Three accelerometers and LVDTs are installed at the bottom, middle, and top of the panel to measure the displacements and accelerations. Although the ground motion displacement and displacement at other locations of the panel are harmonic, as shown in Figure 2.6a and b, the independently measured ground acceleration is not perfectly harmonic due to that the tests are displacement-controlled instead of acceleration controlled, as shown in Figure 2.6c and d. Each excitation process lasts for more than 15 s, long enough to produce stable and consistent results.

Figure 2.7 shows the displacements at the top of the wall panel when subjected to different ground motions. Since the hollow sectioned GFRP panel is lightweight, the displacement at the top of the wall panel is close to that from the ground motion when only the GFRP wall panel is tested. In contrast, attaching seismic weight to the wall panel significantly increases the top displacement. Also, the displacement under 15.1 Hz ground motion is much greater than that under 10.1 Hz ground motion because 15.1 Hz ground motion provides considerably larger acceleration and is closer to the natural frequency of the GFRP wall. No damage occurred during the 15.1 Hz ground motion run where the

acceleration reached 2.1g. The maximum story drift of the GFRP panel recorded is 0.33%, which is smaller than allowed values of structural walls under extreme loads, mainly because of the high stiffness and the GFRP material's ability to remain linear under high strain.

2.5 Finite Element Analysis Simulation of GFRP Panel Tests

FEA models are constructed using Abaqus (v6.14). Shell element S4R is used to simulate the GFRP panel, as shown in Figure 2.8. In the vibration analysis, GFRP pultruded structural members can be treated as elastic materials using currently available theories and computational methods [8]. Using the material properties from the test results, the GFRP material is taken as linear elastic with an elastic modulus and Poisson's ratio of 5.6 GPa and 0.27. Rayleigh damping, which is also known as proportional damping, is included in the GFRP material properties (Kyriazoglou and Guild [27]). The mass proportional damping and the stiffness proportional damping factors can be calculated if both the first and the second modes are assumed to have the same damping ratio $\zeta = 0.6\%$. In the FEA model, the bottom of the GFRP panel is fixed except in the in-plane direction, which is used to apply the acceleration excitations. Table 2.4 compares natural frequencies obtained from the FEA models with those from shaking table tests. Satisfactory agreement is achieved, showing the linear structural characteristics of the panel.

Figure 2.9 are plots comparing the response time histories of the FEA models with those of the test results. The errors between the FEA models and tests are within 4% and 13% for the cases with and without the attached mass, respectively. There is also a slight difference in phase for the attached mass cases, which could be attributed to the ignored damping at the mass connection. The displacement amplitudes in the experimental results are slightly larger than predicted. The difference may be explained by that the stiffness of the

shaking table itself is not large enough to provide a perfect fixed boundary condition for the test specimen, and minor rotations in the in-plane direction might have happened in the dynamic tests. Overall, good agreement is found with the free vibration test and the shaking table test. The FEA result also shows that the maximum stress during the vibration is 40.2 MPa, which is smaller than the GFRP's strength 169 MPa, validating that the GFRP panel is intact during the testing.

2.6 Comparison of GFRP Wall Panel and RC Wall Under Seismic Ground Motion

Shaking table tests presented above demonstrated that the GFRP panel remained elastic under large ground accelerations. In order to further evaluate the performance of GFRP wall panel under seismic excitations, its performance is compared with structural RC walls under realistic ground motions. The selected RC wall is a 1:1.25 scale shear wall tested on a shaking table by Carrillo and Alcocer [28]. This specific RC panel is selected because it has the same thickness as the tested GFRP wall panel. In addition, the RC panel has the minimum reinforcement ratio, which is the ratio of the area of steel bars over the area of the web of the concrete cross-section, specified in ACI-318. It was originally used as a control specimen. The reinforcement layout and FEA model mesh of the 8-cm thick RC wall are illustrated in Figure 2.10. A single layer of No. 3 welded steel wires is placed in the middle of the RC wall web. Material properties from concrete cylinder tests and steel tension tests are summarized in Table 2.5. In the shaking table test, the RC wall is subjected to a recorded earthquake ground motion CA-71, which occurred in Caleta de Campos station, Mexico, on January 11, 1997 [moment magnitude (MW) = 7.1, peak ground acceleration (PGA) = 0.38 g], representing a large-amplitude earthquake event with high intensity and duration. The acceleration time history is shown in Figure 2.11. A seismic weight of 245 kN is selected to achieve a natural period of 0.1 s, matching the earthquake's dominating frequency.

An FEA model is created in Abaqus and compared to the experiment results in the RC wall research paper discussed above using its authors' test parameters. The concrete damaged plasticity model in Abaqus is adopted, which considers compression and tension damages to simulate the degradation of concrete stiffness. The steel's hysteretic behavior is modeled using kinematic plasticity. The C3D8R solid element and the T3D2 truss element are used to simulate concrete and steel bars, respectively. No slip between steel bars and concrete is considered. The concrete shear wall is rigidly fixed at the bottom and loaded in the in-plane direction with the CA-71 earthquake motion. Figure 2.12a shows the comparison between FEA and test results. From the time history of displacement in the dynamic explicit model, as showed in Figure 2.12b, the most significant concrete damage occurs at 12.9 s, forming a permanent deformation in the web of the RC wall. The FEA curve can predict the stiffness and the ultimate drift ratio of the shear RC wall under the earthquake excitation. The difference between the both data sets is caused by the approximation of concrete damage coefficients in the FEA of the concrete material model. The exact values could be only obtained through cyclic loading test of concrete specimen. However, this information was not mentioned in Ref [28]. The largest stress, as expected, appears in the web region, which has the lowest steel ratio. Concrete damage happens near the areas where the steel bars are embedded, as illustrated in Figure 2.13.

From the above results, it can be concluded that the FEA models of both RC and GFRP walls can accurately predict their dynamic behaviors. Next, to gain a better understanding of the GFRP panel's capability to resist seismic loads, a comparison of GFRP wall panel and RC wall is carried out by simulating the responses of both types of walls under earthquake motions. As mentioned above, the tested RC and GFRP walls have the

same thickness of 8 cm. In this comparison, we keep the GFRP panel's cross-section unchanged, but increase its 2-D dimensions to be identical to that of the RC wall, i.e., 192 cm x 192 cm. The CA-71 earthquake record is scaled to create four different ground motions, representing low, moderate, high and ultra-high intensity earthquake events, respectively.

In the first set of comparison, the same mass block of 245 kN, representing the seismic load from a multi-story building, is attached to the top of both RC and GFRP walls. Table 2.6 lists PGAs for each ground motion, and the maximum drifts and stresses during the excitations. The web region in the RC wall is found to be severely damaged under both high and ultra-high intensity earthquakes. Since the failure criterion of the GFRP panel is not specified in the FEA model, the maximum stress of the GFRP panel during the high intensity ground motion reaches 213.6 MPa, which exceeds its flexural strength of 162 MPa. Therefore, the GFRP panel fails in the high intensity earthquake. The time histories of the two walls are compared in Figure 2.14. Due to the difference in the stiffness, the GFRP wall produces larger drifts than the RC wall. However, this difference is smaller for high and ultra-high intensity earthquakes compared to those for low and moderate intensity earthquakes, indicating that the dynamic stiffness of the RC wall under severe earthquakes deteriorates more rapidly than that of the GFRP wall.

Based on the above comparison, it can be concluded that GFRP wall panels have less energy dissipation capacity than RC walls. The relatively low damping ratio of the GFRP and the lack of post-elastic behavior are its drawbacks when used as seismic-resistant structures. Another difference between the RC and GFRP walls is that the GFRP wall remains at its original position after the earthquake; while the RC wall yields, resulting in a permanent

lateral deflection. Generally, GFRP wall panels do not have enough stiffness to replace RC walls in multi-story buildings.

Since pultruded GFRP structures are often low-rise and carry significantly lower seismic weight, we make another comparison of the two walls carrying a much smaller seismic mass of 4.8 kN, which corresponds to the full dead load plus 20% of the snow load, as listed in Table 2.2, for a one-story building. In this case, the maximum stress and drift of the two walls become much smaller, as illustrated in

Table 2.7, showing that both walls are in elastic range. Generally, the maximum stress and drift are proportional to the seismic excitation acceleration. The maximum stress of GFRP wall is 5.4 MPa, which is much lower than its lengthwise flexural strength of 162 MPa. The RC wall still has lower stress and drift ratio due to its larger stiffness, as shown in Figure 2.15. However, the performances of the two walls are closer compared to those for multi-story buildings. Since the GFRP wall panel has much smaller self-weight and higher strength, it can be considered as a viable solution for low-rise buildings in seismic zones.

Parametric studies are conducted to better understand the GFRP wall panels' application. First, shell thicknesses are varied to investigate how much the GFRP panel's section increase is needed to match the RC wall's dynamic stiffness. In the FEA model, the shell thicknesses of GFRP panel are doubled and tripled, and then they are compared to the RC wall with a seismic load of 245 kN under the high intensity ground motion. The results listed in Table 2.8 show that the GFRP's shell thicknesses need to be increased three times to achieve similar deflection of RC walls. This may pose a challenge in FRP fabrication. Another parameter studied is the seismic weight attached on the top the panel. The maximum stresses and drifts under the high intensity ground motion are listed in Table 2.9, which

indicates that, in order for the GFRP panel's stress and drift to be within a reasonable range, the supported seismic weight on the panel should be less than 96 kN. This weight approximately corresponds to a three-story residential building.

2.7 Conclusions

Dynamic behavior of a pultruded GFRP wall panel is experimentally and numerically examined. Free vibration tests of the panel indicates their higher natural frequencies and lower damping ratios than other types of traditional structural walls. The GFRP panel in the shaking table tests exhibits good resistance to the seismic load due to its high strength and lightweight despite the high intensity of input ground motion, indicating that GFRP panels have a potential to be used as seismic-resistant structural walls.

FEA models are created to correlate the displacement time history of the GFRP panel from shaking table test. The same method is applied to model a traditional RC shear wall under earthquake excitations in literature. Both models achieve good correlations with experimental results. After comparing their performances under seismic loads, we can conclude that, when applied to multi-story buildings, RC walls tend to have smaller drift and higher energy dissipation capacity compared to GFRP walls. Therefore, RC walls remain a better option. However, when designed as shear walls for low-rise buildings, the deformation and the maximum stress of the RC and GFRP walls are closer compared to those for multi-story buildings. Parametric study shows that the GFRP walls can support seismic weight of buildings with no more than three stories. Due to its elastic behavior, the performance of the GFRP wall panel is more predictable. In addition, it has low self-weight and high strength and is easier for post-earthquake repair and replacement, which makes the GFRP wall panel a viable solution for low-rise buildings in seismic zones.

2.8 References

[1] Antoniades KK, Salonikios TN, Kappos AJ. Cyclic tests on seismically damaged reinforced concrete walls strengthened using fiber-reinforced polymer reinforcement. ACI Struct J 2003;100(4):510–8.

[2] Lu X, Zhou Y, Yan F. Shaking table test and numerical analysis of RC frames with viscous wall dampers. J Struct Eng 2008;134(1):64–76.

[3] Clarke JL. EUROCOMP design code and handbook. Structural design of polymer composites London: E & FN Spon; 1996.

[4] Davalos JF, Salim HA, Qiao P, Lopez-Anido R, Barbero EJ. Analysis and design of pultruded FRP shapes under bending. Compos B Eng 1996;27(3):295–305.

[5] Bank LC. Properties of pultruded Fiber Reinforced Plastic structural members. Transp Res Record 1989. 1223.

[6] Karbhari VM, Seible F, Kolozs RT. Experimental dynamic characterization of an FRP composite bridge superstructure assembly. Compos Struct 2001;54(4):427–44.

[7] Reising R, Shahrooz B, Hunt V, Lenett M, Christopher S, Neumann A, et al.

[8] Performance of five-span steel bridge with fiber-reinforced polymer composite deck panels. Transp Res Rec 2001;1770:113–23.

[9] Wight RG, Erki MA, Shyu CT, Tanovic R, Heffernan PJ. Development of FRP shortspan deployable bridge—experimental results. J Bridge Eng 2006;11(4):489–98.

[10] Mosallam Ayman S, Abdelhamid Mohamed K, Conway Jerroled H. Performance of pultruded FRP connections under static and dynamic loads. J Reinf Plast Compos 1996;13(5):386–407.

[11] Boscato G, Russo S. Free vibrations of pultruded FRP elements: mechanical characterization, analysis, and applications. J Compos Constr 2009;13(6):565–74.

[12] Russo S. Experimental and finite element analysis of a very large pultruded FRP

[13] structure subjected to free vibration. Compos Struct 2012;94(3):1097–105.

[14] Boscato G, Dal Cin A, Russo S. Dynamic identification of All-FRP pultruded structures. Int J Eng Technol 2015;7(2):81.

[15] Xiao Y, Bai Y, Luo JL, Zhao XL, Ding FX. Dynamic and fatigue performances of a large-scale space frame assembled using pultruded GFRP composites. Compos Struct 2016;138: 227–36.

[16] Bai Y, Keller T. Modal parameter identification for a GFRP pedestrian bridge. Compos Struct 2008;82(1):90–100.

[17] Zhang Z, Bai Y, He X, Jin L, Zhu L. Cyclic performance of bonded sleeve beam column connections for FRP tubular sections. Compos B Eng 2018;142:171–82.

[18] Ding FX, Yin GA, Jiang LZ, Bai Y. Composite frame of circular CFST column to steel–concrete composite beam under lateral cyclic loading. Thin-Walled Struct 2018;122: 137–46.

[19] Zi G, Kim BM, Hwang YK, Lee YH. An experimental study on static behavior of a GFRP bridge deck filled with a polyurethane foam. Compos Struct 2008;82(2):257–68.

[20] Satasivam S, Bai Y, Zhao XL. Adhesively bonded modular GFRP web–flange sandwich for building floor construction. Compos Struct 2014;111:381–92.

[21] [19] Satasivam S, Bai Y, Yang Y, Zhu L, Zhao XL. Mechanical performance of two-way modular FRP sandwich slabs. Compos Struct 2018;184:904–16.

[22] Satasivam S, Bai Y. Mechanical performance of bolted modular GFRP composite sandwich structures using standard and blind bolts. Compos Struct 2014;117:59–70.

[23] Satasivam S, Bai Y. Mechanical performance of modular FRP-steel composite beams for building construction. Mater Struct 2016;49(10):4113–29.

[24] Lestuzzi P, Bachmann H. Displacement ductility and energy assessment from

[25] shaking table tests on RC structural walls. Eng Struct 2007;29(8):1708–21.

[26] Ghorbanirenani I, Tremblay R, Léger P, Leclerc M. Shake table testing of slender RC shear walls subjected to eastern North America seismic ground motions. J Struct Eng 2011;138(12):1515–29.

[27] Mo YL, Zhong J, Hsu TT. Seismic simulation of RC wall-type structures. Eng Struct 2008;30(11):3167–75.

[28] El-Sokkary H, Galal K, Ghorbanirenani I, Léger P, Tremblay R. Shake table tests on FRP-rehabilitated RC shear walls. J Compos Constr 2012;17(1):79–90.

[29] Voltera E, Zachmanoglou EC. Dynamics of Vibrations. Columbus: Charles E. Merrill Books Inc; 1965.

[30] Kyriazoglou C, Guild FJ. Finite element prediction of damping of composite GFRP and CFRP laminates–a hybrid formulation–vibration damping experiments and

[31] Rayleigh damping. Compos Sci Technol 2007;67(11):2643–54.

[32] Carrillo J, Alcocer SM. Seismic performance of concrete walls for housing subjected to shaking table excitations. Eng Struct 2012;41:98–107.

Table 2.1 *Lateral stiffness of GFRP panel*

	Flexural modulus (lengthwise)	Difference from the data reported by manufacturer
From pushover test	5.52 GPa	9.5%
From three-point bending test	5.59 GPa	8.4%

Table 2.2 *Seismic load at the panel roof*

Dead load	Snow load	Transverse length	Total seismic weight per unit width	Panel width	Total weight	Scale	Scaled weight in test
501 Pa	300 Pa	4.5 m	2.50 kN	0.61 m	1.5 kN	1:2.5	0.24 kN

Table 2.3 *Ground motion parameters*

Ground motion	Frequency	Maximum displacement	Average acceleration amplitude
1	10.1Hz	1.83 mm	1.4 g
2	15.1Hz	1.94 mm	2.1 g

Table 2.4 *Comparison of natural frequencies obtained from free vibration test and FEA model*

	Without seismic mass attached		With seismic mass attached	
Natural frequencies	f_1 (Hz)	f_2 (Hz)	f_1 (Hz)	f_2 (Hz)
Free vibration test	117	196	47	70
FEA model	121	201	48	72
Difference (%)	3.4%	2.6%	2.1%	2.9%

Table 2.5 *Material property of the RC wall*

concrete	Elastic modulus (GPa)	Compression strength (MPa)
	14.8	24.8
	Nominal yield strength (MPa)	Ultimate strength (MPa)
steel bar	412	656
steel wire	435	659

Table 2.6 *Comparisons of maximum stress and drift under the seismic load of 245 kN*

Ground motion	PGA(g)	RC wall		GFRP panel	
		Maximum stress (MPa)	Maximum drift (mm)	Maximum stress (MPa)	Maximum drift (mm)
Low intensity	0.10	17.8	1.5	40.4	7.0
Moderate intensity	0.20	24.2	2.5	81.1	14.0
High intensity	0.40	24.8	10.2	172.8	26.8
Ultra-high intensity	0.60	24.8	17.8	213.6	44.2

Table 2.7 *Comparisons of maximum stress and drift under the seismic load of 4.8 kN*

Ground motion	PGA(g)	RC wall		GFRP panel	
		Maximum stress (MPa)	Maximum drift (mm)	Maximum stress (MPa)	Maximum drift (mm)
Low intensity	0.10	0.56	0.10	1.3	0.34
Moderate intensity	0.20	0.99	0.20	2.4	0.69
High intensity	0.40	1.97	0.41	4.1	1.35
Ultra-high intensity	0.60	2.92	0.61	5.4	1.97

Table 2.8 *Parametric study of the GFRP panel's shell thickness*

Specimen	Maximum stress (MPa)	Maximum drift (mm)
GFRP panel with original thickness	172.8	26.8
GFRP panel with double thickness	95.6	18.2
GFRP panel with triple thickness	60.3	10.6
RC wall	24.8	10.2

Table 2.9 *Parametric study of the supported seismic load on the top of the GFRP panel*

Supported seismic load	Maximum stress (MPa)	Maximum drift (mm)
4.8 kN	4.1	1.35
48 kN	38.7	9.6
96 kN	75.8	16.2
142 kN	111.6	21.4
245 kN	172.8	26.8

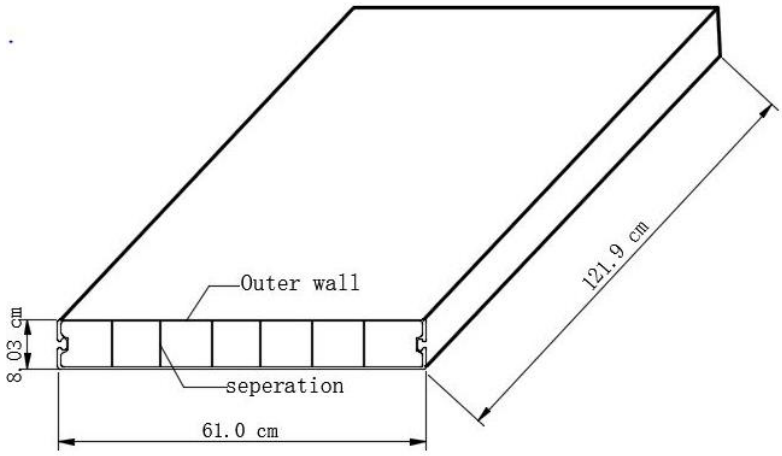

Figure 2.1 *Geometry profile of GFRP panel*

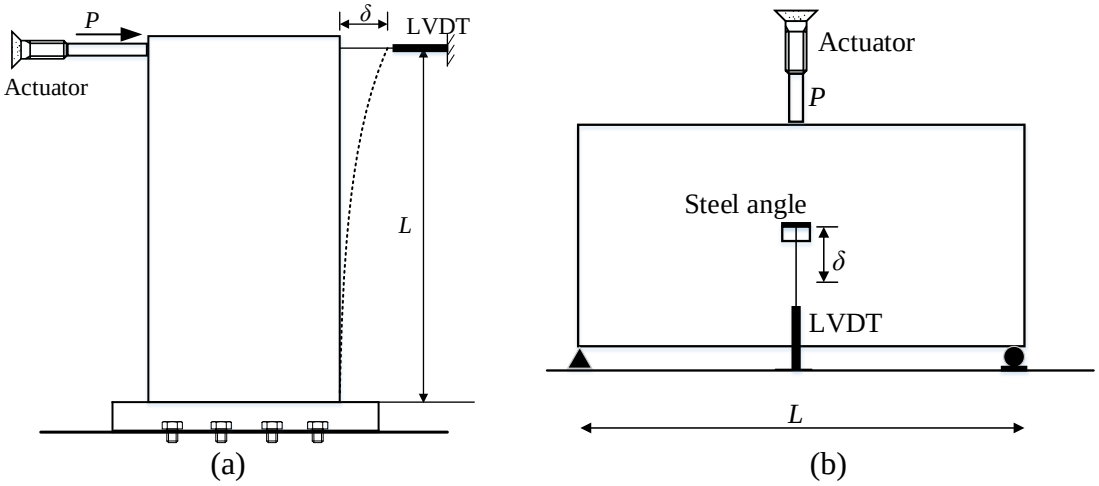

Figure 2.2 *Test configurations to establish lateral stiffness (a) Push-over test; (b) Three-point bending test.*

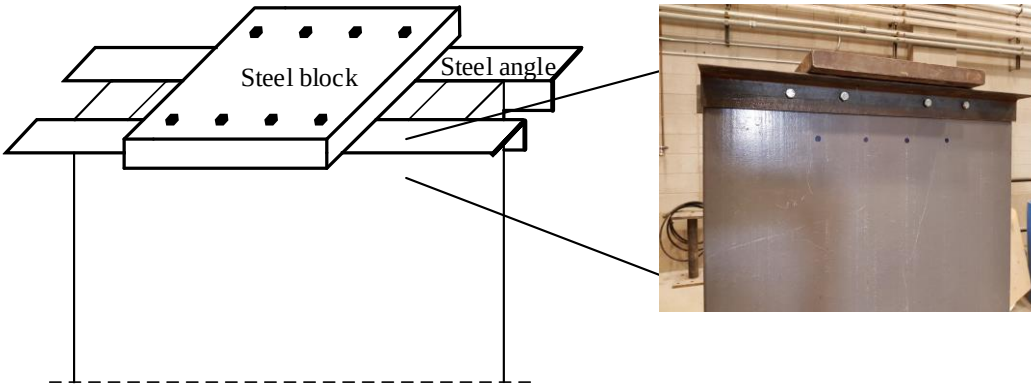

Figure 2.3 *Steel block on the GFRP panel wall*

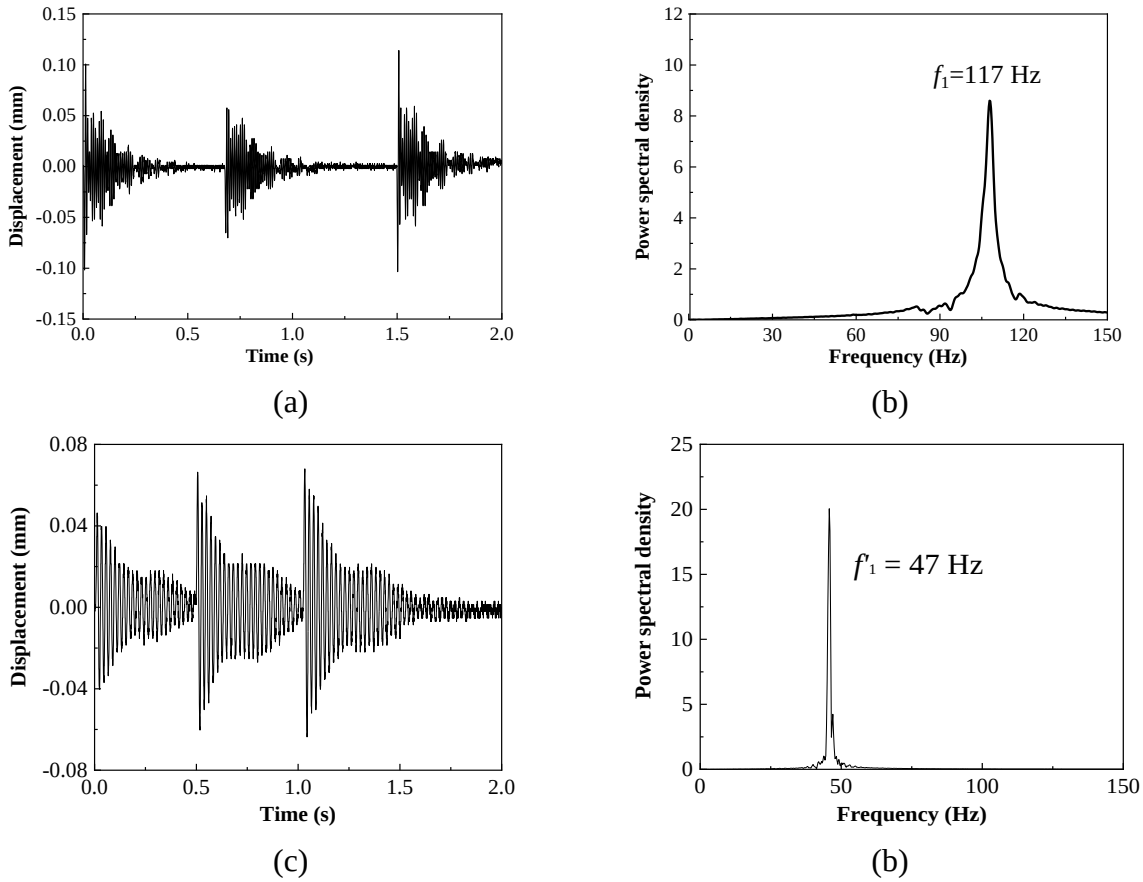

Figure 2.4 *Free vibration tests of the GFRP panel: (a) test without seismic mass; (b) power spectral density of (a); (c) test with seismic mass; (d) power spectral density of (c)*

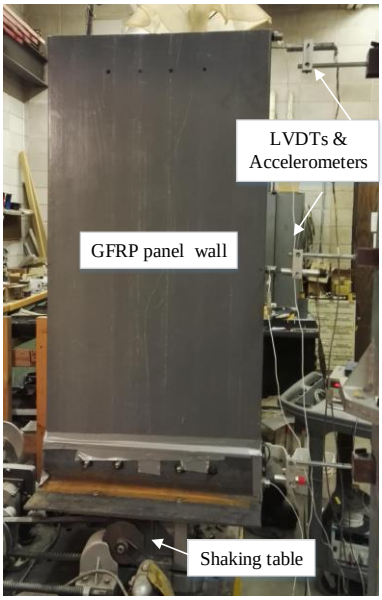

Figure 2.5 *Shaking table test configuration*

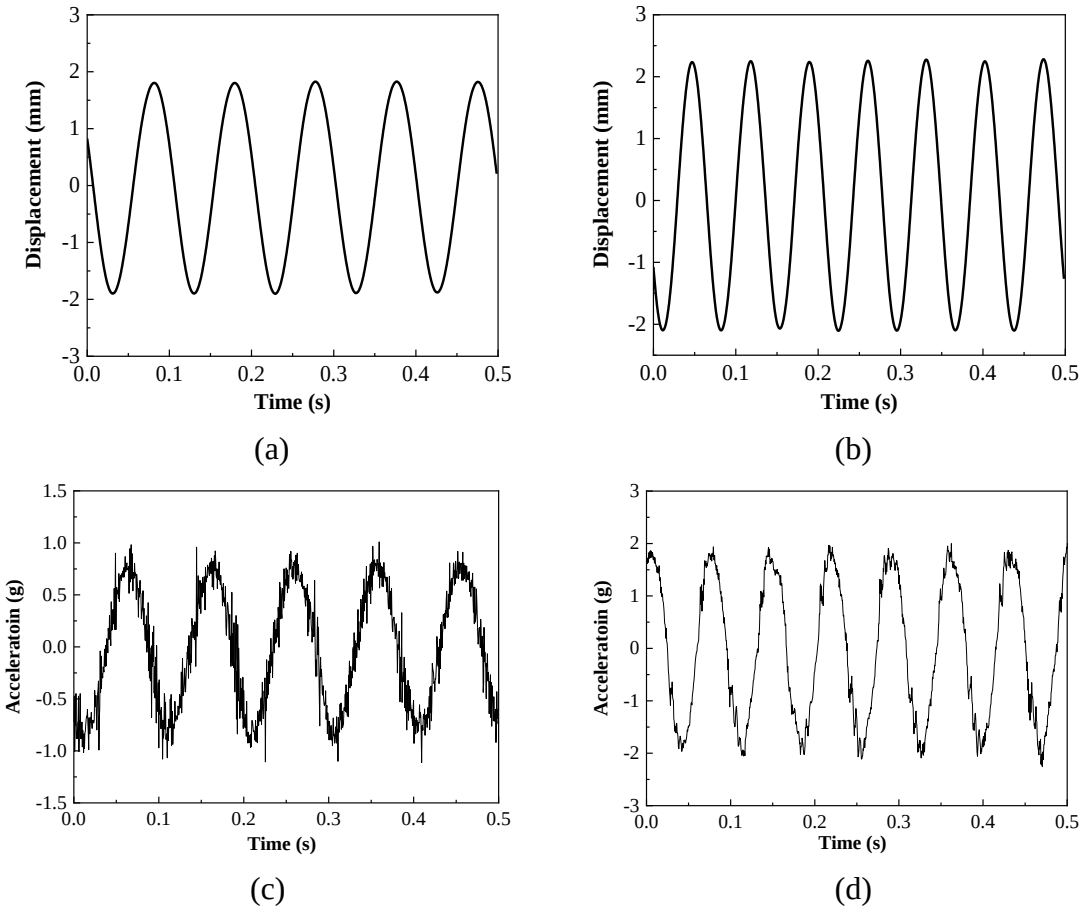

Figure 2.6 *Shaking table test ground motions: (a) 10.1 Hz ground motion displacement; (b) 15.1 Hz ground motion displacement; (c) 10.1 Hz ground motion acceleration; (d) 15.1 Hz ground motion acceleration*

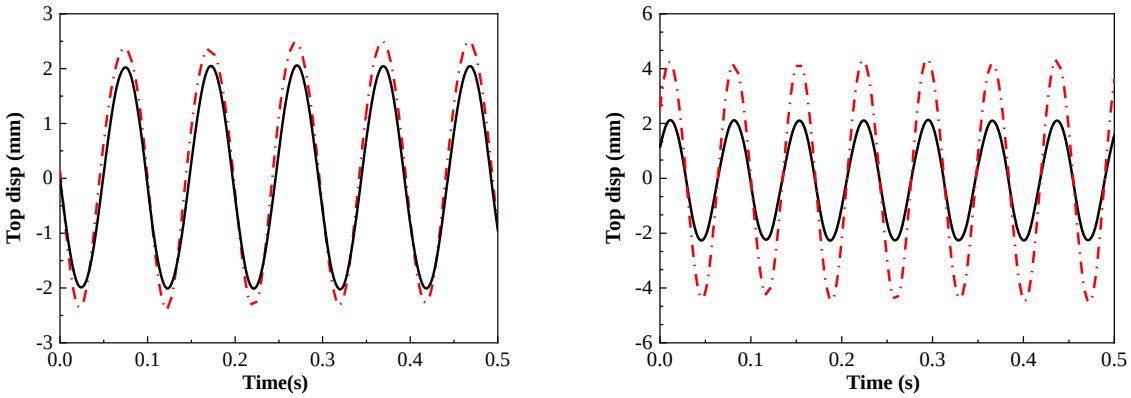

(a) (b)

Figure 2.7 *Shaking table test results (solid line: without mass; dashed line: with mass): (a) 10.1 Hz test displacement;(b) 15.1 Hz test displacement*

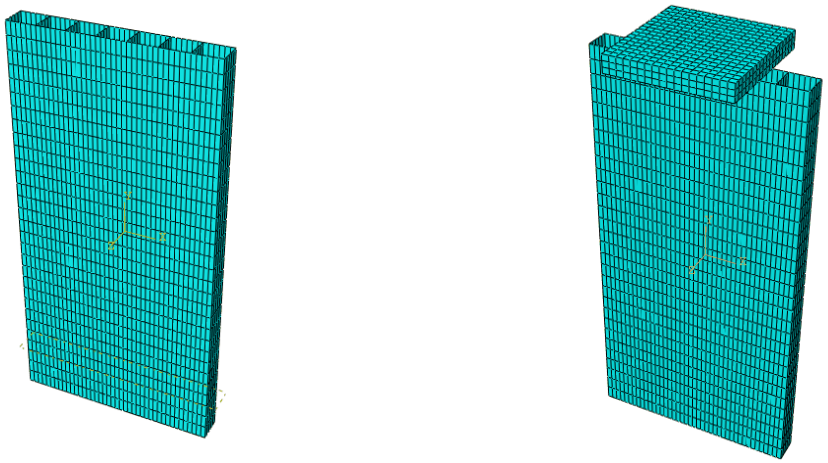

(a) (b)

Figure 2.8 *Mesh of FEA model: (a) GFRP panel without mass; (b) GFRP panel with mass*

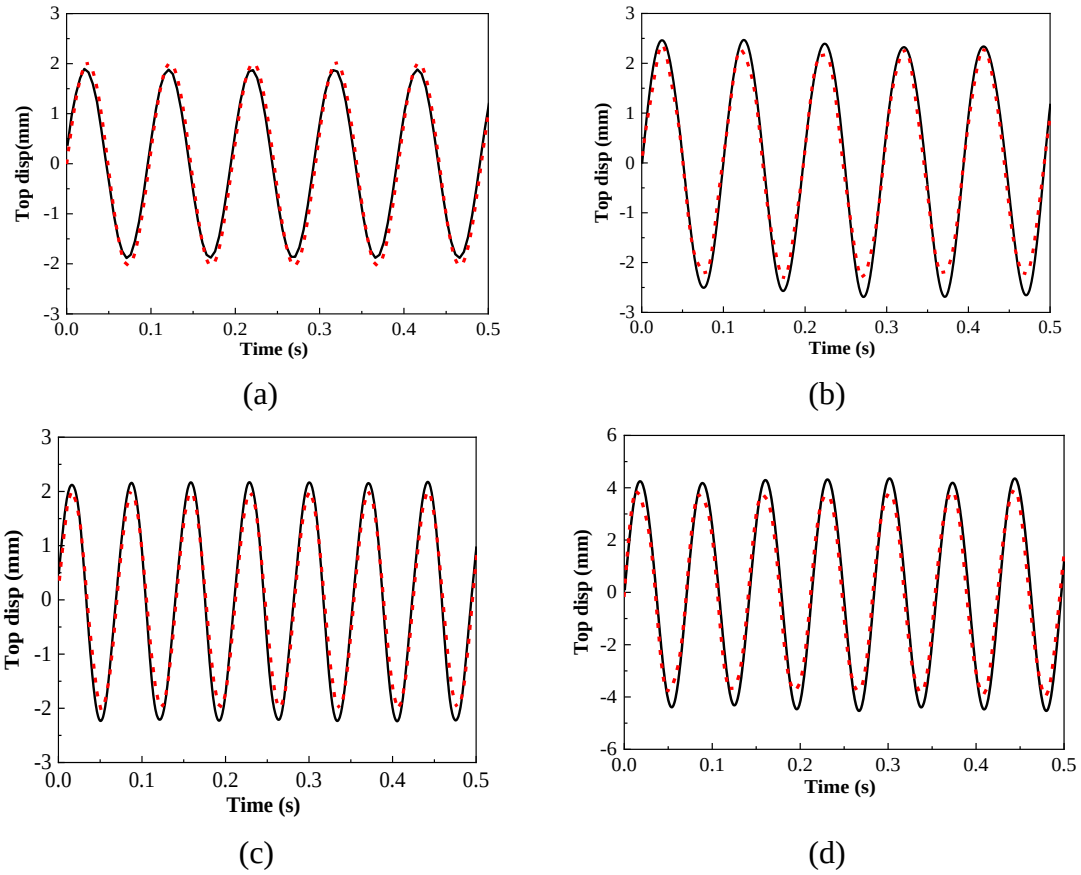

Figure 2.9 *GFRP panel FEA simulation results (solid line: experimental; dashed line: FEA simulation): (a) 10.1 Hz simulation without mass; (b) 10.1 Hz simulation with mass; (c) 15.1 Hz simulation without mass; (d) 15.1 Hz simulation with mass*

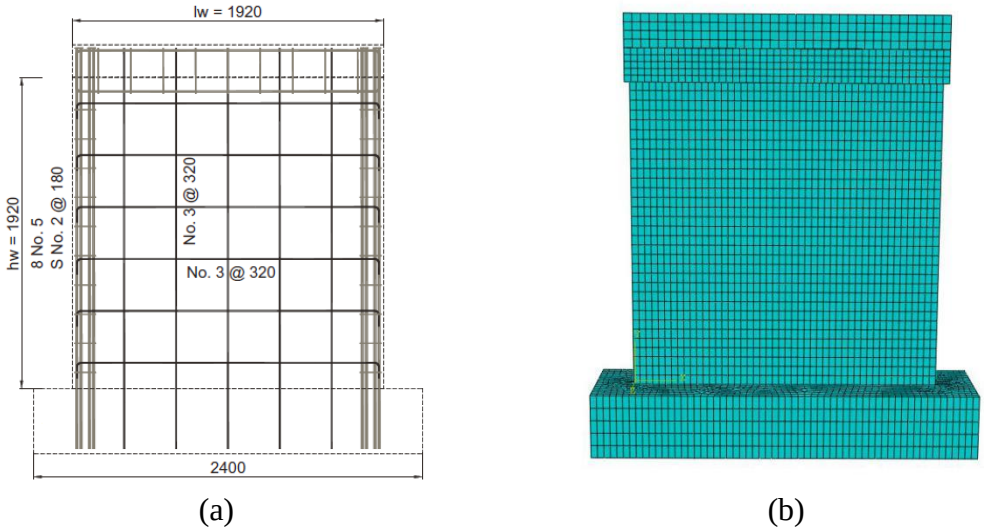

Figure 2.10 *Reinforcement layout and FEA model of the concrete specimen: (a) Configuration in test (mm) [22]; (b) FEA model in Abaqus*

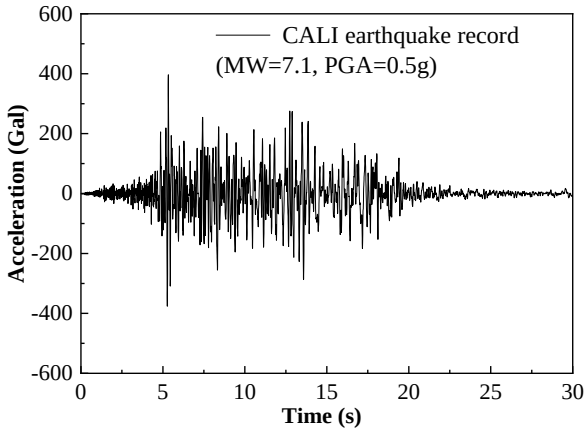

Figure 2.11 *Time series of input seismic ground motion*

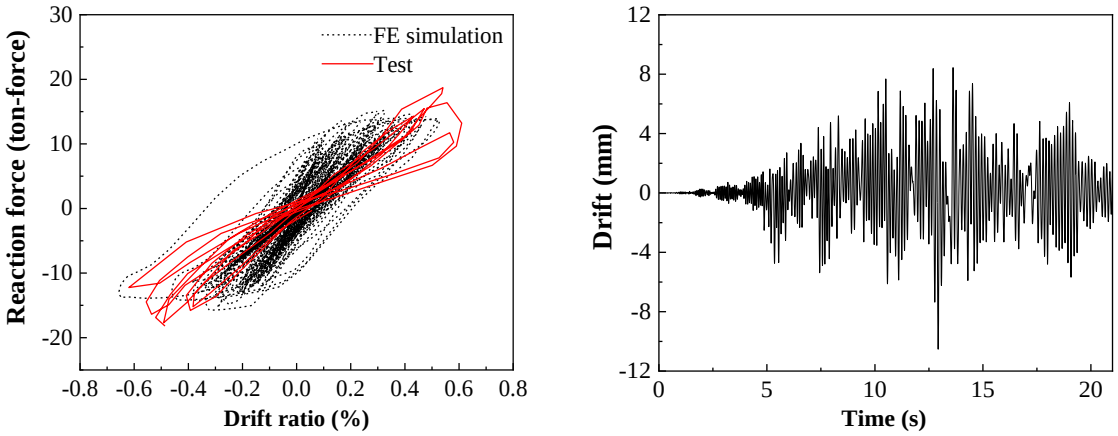

(a) (b)

Figure 2.12 *RC wall FEA simulation results: (a) Comparison of hysteretic curves of test and FEA;(b) Drift time history*

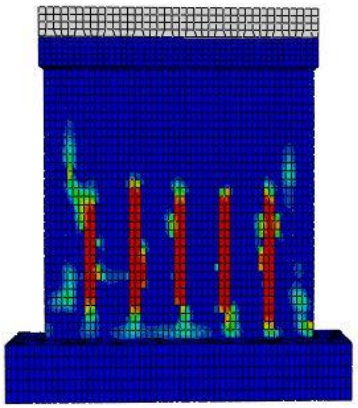

Figure 2.13 *Concrete damage at the end of FEA simulation (red regions represent damage)*

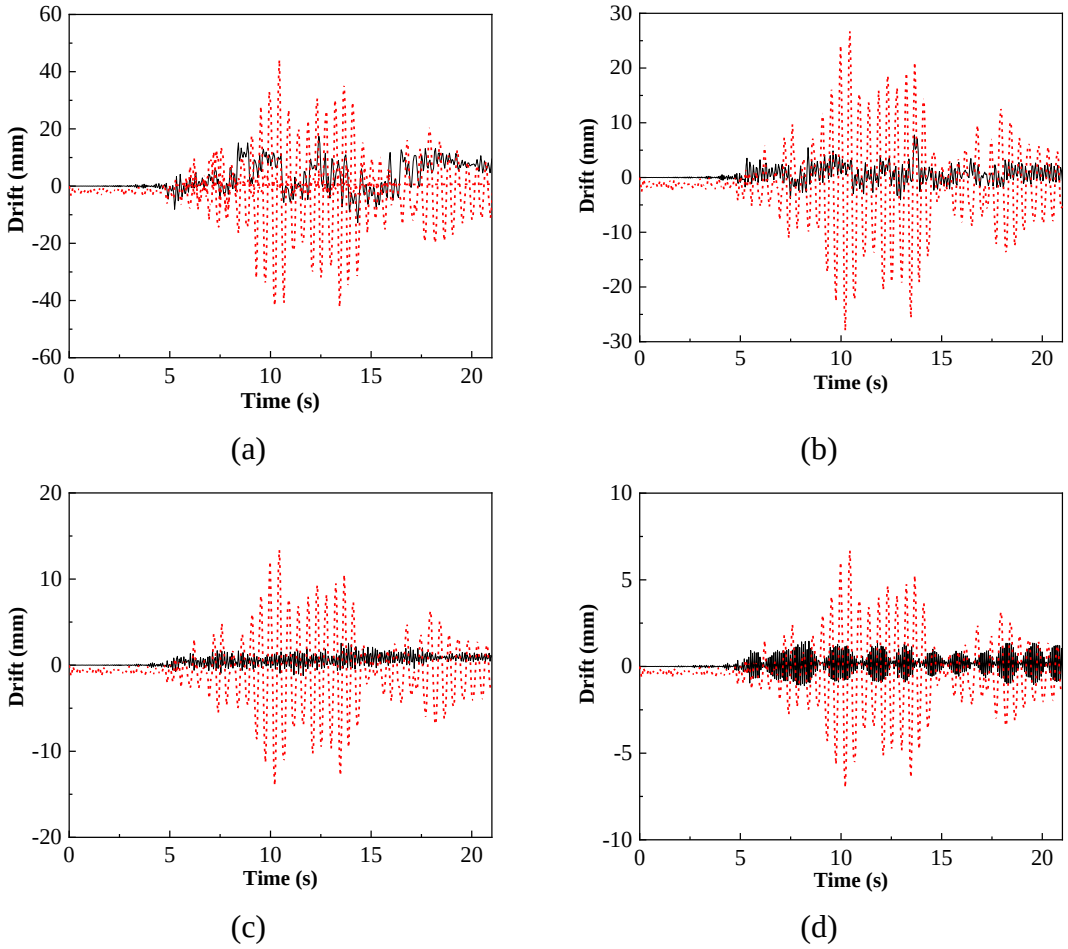

Figure 2.14 *Comparisons of time histories of drifts under the seismic load of 245 kN (solid line: the RC wall; dashed line: the GFRP panel wall): (a) under ultra-high intensity;(b)under high intensity;(c)under middle intensity;(d)under low intensity*

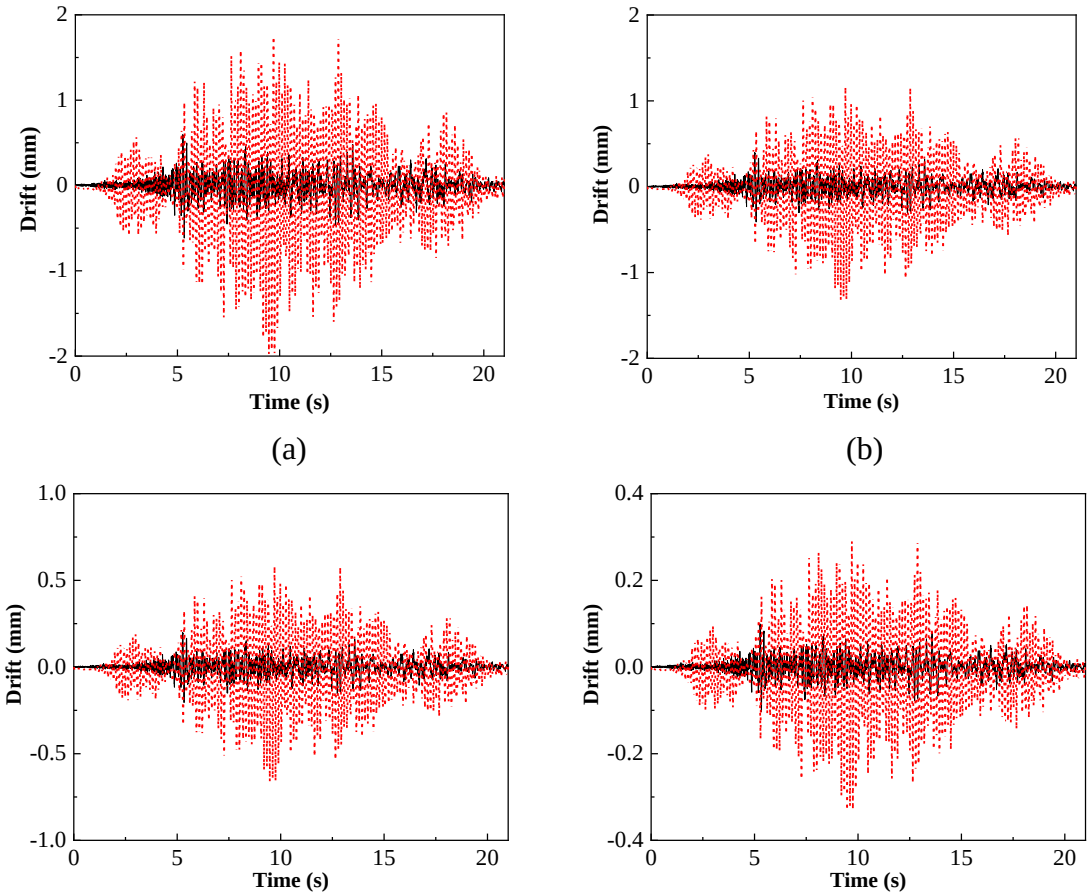

Figure 2.15 *Comparisons of time histories of drifts under the seismic load of 4.8 kN (solid line: the RC wall; dashed line: the GFRP panel wall): (a) under ultra-high intensity; (b) under high intensity;(c) under middle intensity;(d)under low intensity*

CHAPTER 3. BEHAVIOR OF GFRP WALL PANEL WITH AN INTERNAL TUNED LIQUID COLUMN DAMPER

A paper to be submitted to Composite Structures

Hao Wu, An Chen, Simon Laflamme

3.1 Abstract

Pultruded Glass Fiber-Reinforced Polymer (GFRP) structures have been increasingly used in buildings and civil infrastructure systems because of their high strength, lightweight, durability, and fatigue resistance. However, these structures are elastic and typically have low damping ratio, which limits their capability to dissipate vibration energy during earthquakes. Adding internal damping mechanisms to GFRP components can transform a traditional structure into one that is capable of mitigating the effect of lateral dynamic loads. This paper studies a multi-celled GFRP wall panel of a uniform cross-section equipped with a built-in tuned liquid column damper (TLCD). The panel is adapted to allow oscillation of water in its internal hollow cells, generating damping through liquid head losses. Different combinations of water heights and cell openings are evaluated using shaking table tests to study their capability to reduce vibration in the GFRP wall panel. For each combination, the natural frequency of TLCD can be predicted with a simple model. It is found that higher water volume inside the panel can achieve greater mitigation effect, and the panel's vibration amplitude is reduced as much as 26% due to liquid damping. A computational fluid dynamics (CFD) model is created to study the liquid motion inside the GFRP panel under harmonic ground excitations. Results from the CFD simulation are in good agreement with those from the test.

Keywords: Pultruded GFRP, Seismic resistance, Tuned liquid column damper, CFD simulation

3.2 Introduction

Pultruded GFRP structures have been widely studied, showing as good alternatives to steel and reinforced concrete (RC) solutions due to their high strength-weight ratio, easy installation, and corrosion resistance (Keller 2001 [1]). Common applications include low-rise buildings, bridge decks, space structures, towers, etc (Xin et al. 2015 [2]; Wu et al. 2016 [3]; Rao et al. 2017 [4]). Static tests demonstrated that GFRP components are viscoelastic and anisotropic (Ascione et al. 2011 [5]; Wattick and Chen 2017 [6]). Several other researchers studied the dynamic behavior of pultruded GFRP structures. Boscato and Russo (2009) [7] showed that GFRP structures tended to have low frequency and high deformability, which may be leveraged to mitigate seismic loading. While it was discussed that pultruded FRP does not suffer significant degradation after large numbers of cyclic loading (Yang et al. 2009 [8]), it was found that GRFP structures have low damping ratios (usually less than 2%), and their performance in dissipating vibration energy was not great (Russo 2012 [9]). It follows that the inclusion of damping mechanisms inside pultruded GFRP structures can result in a significant enhancement of their lateral load mitigation performance.

This study focuses on a GFRP panel structure with an internal liquid flow system. This system is intended as a circuit cooling/heating system using liquid as the thermal exchanger. However, we propose that internal liquid flow can also provide supplemental damping capability for this GFRP panel structure. The GFRP panel has an internal multi-capillary structure that allows oscillating liquid (typically water) to flow through a horizontal channel connecting all the capillaries. There are some other types of structures embedded with fluid systems that are intended to increase the overall damping. For example, Matia and Gat [10] proposed an elastic beam embedded with a fluid-filled parallel-channel network,

which can greatly reduce the dynamic deformation of the beam; Wang et al. [11] conducted a damping analysis of a flexible beam containing an internal channel filled with three types of high-viscosity fluid. However, there are no studies available on structural members resisting lateral vibration through liquid oscillation.

Dramatic liquid motion change, such as flow through orifices and sharp corners, can result in liquid head loss, dissipating kinetic energy. This internal damping mechanism inside this GFRP panel can be described as a tuned liquid column damper (TLCD), which is a special type of passive damping devices that utilize the liquid's gravity force as the restoring force and generate damping from the head loss around orifices and sharp corners. TLCDs have been effectively used in suppressing the vibration of tall buildings and long bridges under wind or earthquake hazards (Shum et al. 2008 [12]; Min et al. 2014 [13]). Both design procedures and experimental studies have been conducted on TLCDs suppressing structural motions (Connor and Laflamme 2014 [14]; Di Matteo et al. 2014 [15]). Min et al. (2014) [16] proposed a novel passive TLCD with multiple cells that can be opened or sealed after installation and provided a methodology to compute the natural frequencies of multi-celled liquid damper system. More recently, Computational Fluid Dynamics (CFD) method was introduced to numerically validate the liquid motion in TLCDs (Cammelli et al. 2016 [17]).

This paper first describes a shaking table test on the proposed GFRP panels with an internal TLCD, demonstrating that this damping system can reduce the panel's vibrations under harmonic ground excitations. Next, a simple model is presented to compute the TLCD's natural frequency and predict its motion. Lastly, CFD models are created to simulate the liquid motion and measure the damping forces generated by the internal damper.

3.3 Test Setup

The pultruded GFRP panel is a 7-celled geometry with a dimension of 121.1 cm × 61.0 cm × 8.1 cm (height × width × depth), as shown in Figure 2.1. The thickness of the outer and inner shells are 0.297 cm and 0.218 cm, respectively. The panel has a uniform cross-section across its length, with both in-plane and out-of-plane properties obtained from static tests summarized in Table 2.1 (Wu and Chen 2016 [18]).

The shaking table test is conducted in the Structural Engineering Research Laboratory at Iowa State University. The test setup is shown in Figure 2.2 a. A steel block is attached at the top of the GFRP panel to represent the seismic weight of the total dead load and 20% of the snow load. The panel itself is attached to the shaking table by steel bolts and to reproduce a fixed support at the bottom. Harmonic ground excitations generated by the shaking table are recorded by accelerometers and Linear Variable Differential Transformers (LVDTs) using MEGADAC data acquisition system at a sampling rate of 2000 Hz. The shaking table can generate harmonic ground motions with a frequency ranging from 10 to 60 Hz. Displacement and acceleration of for two harmonic ground motions of different frequencies are shown in Table 3.2 and Figure 3.2. Accelerometers and LVDTs are installed at the middle and top of the panel as well to record its acceleration and deformation at each location. Panel deformation caused by the seismic mass under dynamic load is used as a measurement of the panel vibration, and it can be obtained by calculating the difference between the panel's top and bottom displacements.

The GFRP panel is adapted to include a TLCD system. The interior of the TLCD system is shown in Figure 3.4 b, where 5 cm × 5 cm square orifices are cut at the bottom of the panel to allow water to flow freely in all the cells. To control the number of cells included in the TLCD, orifices are blocked/unblocked using hard foam to limit water motion in certain

cells, as illustrated in Figure 3.4 a. When blocked by the foam, water cannot flow through the blocked orifice and vice versa. Different water heights, i.e., 0 cm, 31 cm, 62 cm and 93 cm, are investigated as well, as illustrated in Figure 3.3 b. The combinations of the number of cells filled with water and the water heights create different scenarios.

The inclusion of water changes the total mass of the vibration system. The objective of this test to measure the effect of the increased damping on the panel vibration. Therefore, for each scenario, a companion test is conducted under the water distribution but with all the orifices blocked to exclude the influence of mass change of the vibration system (Figure 3.4 b). The difference of the vibration amplitude between the case where the separation exists and the case where the separation does not is used to quantify the damping effect of the TLCD.

3.4 Natural Frequency of TLCD

Due to the symmetry of water heights and cell openings, the natural frequencies of the TLCD can be estimated using a liquid column vibration absorber (LCVA) model proposed by Hitchcock et al. (1994) [19]. A LCVA is a variation of TLCD with unequal horizontal and vertical cross-section areas. Min et al. (2014) [16] suggested that adjacent cells can be combined by recalculating the effective length from centerlines (Figure 3.5):

$$\omega = \frac{1}{2\pi}\sqrt{\frac{2g}{B \cdot A_v / A_h + 2H}} \tag{3-1}$$

where A_v, A_h are the vertical and horizontal tube cross section areas, respectively, g is the gravitational acceleration, B is the effective length between tube centerlines, and H is the water height. Based on this model the TLCD's natural frequencies under investigation range from 0.457 Hz to 0.716 Hz.

The equation of motion for a LCVA is also available using an energy method (Hitchcock et al. 1994):

$$\rho A_v (2H + B \cdot A_v / A_h)\ddot{x} + \frac{1}{2}\rho \frac{A_h}{A_v^2}\eta |\dot{x}| \dot{x} + 2\rho A_v g x = \rho A_v B \ddot{x}_g \tag{3-2}$$

where x is the liquid surface displacement in the vertical tube, ρ is liquid density, η is the head loss coefficient caused by orifices, and $\ddot{x}_g$ is the horizontal acceleration transferred to the LCVA.

3.5 Test Results and Discussion

The GFRP panel's displacement amplitudes with different combinations of cell number, liquid heights and ground motions are summarized in Table 3.3. Since the ground motions are harmonic accelerations, the amplitude of displacement disparity between the top and the base is a good indication of the panel deformation during shaking table tests. The test results analysis focuses on the influence of water height and the number of cells filled with water on the panel deformation under harmonic ground motions. Note that not all combinations of cell numbers and liquid heights were attempted in this shake table test due to a shake table test breakdown.

3.5.1 Comparisons of cases when is no separation between cells

The added water increases the total lateral inertia forces of the water-panel system. As a result, the panel deformation also increases with the amount of water included in the panel system. The increasing amount is related to the volume of water inside the panel, which is determined by two factors: one is the number of cells involved and another one is the initial liquid height in filled cells, which is a uniform value in all cells due to the fact that all water is connected at the bottom area. The number of cells filled with water is always an even

number, i.e., 2 cells, 4 cells and 6 cells since we intend to keep the whole configuration symmetric due to the nature of the external excitation. The total mass of water inside the GFRP panel varies from 7.7 kg to 31 kg.

It is found that the enlarged inertia is caused by both the increasement of the cell number and the initial liquid height. For example, Figure 3.6a shows that the GFRP panel deformation increases as the more cells are filled water with a uniform water height of 61cm under Ground Motion 1: the 2 cells, 4 cells, and 6 cells filled water lead to averaged panel deformation increase of 0.105 cm, 0.142 cm, and 1.96 cm, respectively. When the cell number is fixed, the panel deformation also increases with the water height in these cells, as shown in Figure 3.6b where the panel is excited by Ground Motion 2 and 4 cells are filled with different water heights. The inertia increase is not linear to the rise of the water height, and the largest increase happens where the height rises from 31 cm to 62 cm.

3.5.2 Comparisons of cases with/without separation.

The concrete panel is intended as a multifunctional panel, which the inside water has the dual functions of adjusting the room temperature and mitigating structure vibration. The main objective of this study is evaluation of the increased damping effect due to the panel's liquid motion, it is significant for us to investigate the damping effect alone when the influence of the increased inertia force is excluded. By comparing the results between the tests where the water flows freely and their corresponding companion test where the water flow is blocked, the damping effect can be easily identified by the panel's vibration reduction percentage between these two tests.

From the test results, it can be observed that the GFRP panel's vibration is reduced when water flows freely between cells, indicating that the TLCD provides significant damping, as illustrated by Table 3.3. For example, as shown in the Figure 3.7 a and Figure

3.7 b, with the same number of cells filled with the same water heights, the vibration of the GFRP panel is subdued when there is no separation blocking water flow.

First, the percentage of the vibration amplitude reduction increases with the water height. For instance, when 4 cells are filled water, the water height of 0 cm (no water), 31 cm, 62 cm and 93 cm made the GFRP panel achieve 0%, 5.9%, 6.6% and 9.5% vibration amplitude reduction under ground motion 1, respectively. This is even more notable for 6 cells case under ground motion 1, when the 61 cm water height leads to a 26% reduction due to liquid damping, the largest reduction percentage observed in tests. Data of the case with a 93 cm water height in 6 cells was missing due to malfunction of the shake table, but the first three water heights show a similar trend as the 4 cells case.

The increased cell number also helps the GFRP panel to achieve a greater vibration reduction. Figure 3.7 b shows the comparisons of the GFRP panel's deformation when 2 cells are filled with 62 cm water height under ground motion 1. When the water can flow freely, the damping effect reduced 6.7 % of the total vibration. Under the same ground motion and water height, the 4 cells case achieved 12.8% reduction due to the water flow and the 6cells case achieved an even larger reduction percentage of 26.3%.

Generally, the comparisons under Ground Motion 1 has larger difference percentage than that under Ground Motion 2, mostly likely because the liquid velocity has a limit in a confined space and its increase is not proportional to the ground motion acceleration increase. It is noted that the frequency of the generated ground motion is higher than that of the TLCD configurations, which is due to the limitations of shaking table. More liquid in the GFRP panel will make the TLCD's natural frequency closer to the excitation, attributed to the effectiveness of the TLCD as well.

3.6 CFD Simulation

It is difficult to record the actual water flow during the shake table tests because that GFRP is non-transparent material and videos are not available to record the inside water motion. Instead, to illustrate the water flow inside the GFRP panel and the damping performance of the internal TLCD, a CFD approach is used to illustrate the liquid motion under the test ground motions using in the ANSYS 17.2 Fluent software.

The CFD model is solved using a standard k-ε solver, which is widely used to simulate turbulent flow (Versteeg and Malalasekera 2007 [20]). The GFRP panel is set as the boundary of the liquid domain, and accelerations are applied to the boundaries to excite the liquid. Only the liquid domain is analyzed, and no liquid-solid interaction is considered. The meshing of the liquid domain is shown in Figure 3.8. The maximum mesh size is limited as less than 0.5 cm, with much finer mesh around the orifices in the bottom area. Standard atmospheric pressure is exerted at the air-liquid interface, i.e., the location of liquid height in each cell, enabling the initial liquid surfaces in all the cells are even. Standard gravitational acceleration is included in the whole model.

Figure 3.9 shows the water motion under harmonic Ground Motion 1 when half the panel is filled with water. For the 2 cells case, the water surface fluctuates over a range of 8 cm. The 4 cells case shows a smaller water surface oscillation amplitude of 3 cm. For the 6 cells case, the liquid oscillation further decreases to an amplitude of 2.5 cm. And it is observed that there is not only water flow between different cells, but also water sloshing phenomenon within each individual cell as well. This trend is that more cells of the panel is filled with water, the slower is the liquid motion in vertical cells. It can be explained by that all the water flow has to pass through the orifices at the bottom tube, where the water velocity remains almost constant under the same ground motion. As a result, the water flow

in each cell has lower kinematic energy as they are all split from the same liquid flow in the bottom tube.

The CFD method can also be used to evaluate the damping forces of the internal TLCDs by computing the total lateral dynamic pressure acting on the GFRP panel. The time series of damping force, plotted in Figure 3.10, can be obtained by subtracting the inertia force to the lateral reacting force of the GFRP panel. The magnitudes of the damping forces for the 2 cells, 4 cells and 6 cells are 27 N, 33 N, and 56 N, respectively, corresponding to the amplitude reduction percentage trend from the shaking table test. Simulation results show that the largest damping forces produced are comparable to the GFRP panel's self-weight, and this may help reduce GFRP structure's vibration during seismic events.

3.7 Conclusions

In this paper, a multi-celled GFRP panel was modified by integrating a TLCD system to address GFRP structures' shortcoming of low energy dissipation capability. The cells of the panel are opened in the bottom area to allow liquid exchange between cells. Shaking table tests are conducted to evaluate the effectiveness of the internal TLCD system.

Test results show that the vibration amplitude of the GFRP panel wall can be reduced by leveraging the flow of water. This reduction percentage generally increases with the increase of the water height and the number of cells filled with water. CFD models show that the damping forces generated from TLCDs have the same trend as those from the experimental tests. Simulation results also show that the internal water flow can generate damping forces as large as that the GFRP panel's self-weight. The damping mechanism can be a promising technique to promote wider applications of pultruded GFRP structures in seismic regions.

3.8 References

[1] Keller T. Recent all-composite and hybrid fibre-reinforced polymer bridges and buildings. Progress in Structural Engineering and Materials. 2001 Apr;3(2):132-40.

[2] Xin H, Liu Y, He J, Fan H, Zhang Y. Fatigue behavior of hybrid GFRP-concrete bridge decks under sagging moment. Steel and Composite Structures. 2015;18(4):925-46.

[3] Wu C, Zhang Z, Bai Y. Connections of tubular GFRP wall studs to steel beams for building construction. Composites Part B: Engineering. 2016 Jun 15;95:64-75.

[4] Rao NP, Rokade RP, Balagopal R. Failure investigation of GFRP communication towers. Engineering Failure Analysis. 2017 Sep 1;79:397-407.

[5] Ascione L, Berardi VP, D'Aponte A. A viscoelastic constitutive law for FRP materials. International Journal for Computational Methods in Engineering Science and Mechanics. 2011 Sep 1;12(5):225-32.

[6] Wattick JA, Chen A. Development of a prototype fiber Reinforced Polymer–Concrete Filled wall panel. Engineering Structures. 2017 Sep 15;147:297-308.

[7] Boscato G, Russo S. Free vibrations of pultruded FRP elements: Mechanical characterization, analysis, and applications. Journal of Composites for Construction. 2009 Nov 13;13(6):565-74.

[8] Yang X, Bai Y, Luo FJ, Zhao XL, Ding F. Dynamic and fatigue performances of a large-scale space frame assembled using pultruded GFRP composites. Composite Structures. 2016 Mar 15;138:227-36.

[9] Russo S. Experimental and finite element analysis of a very large pultruded FRP structure subjected to free vibration. Composite structures. 2012 Feb 1;94(3):1097-105.

[10] Matia, Y., and Gat, A. D. (2015). Dynamics of elastic beams with embedded fluid-filled parallel-channel networks. Soft robotics, 2(1), 42-47.

[11] Wang, Y., Masoumi, M., and Gaucher-Petitdemange, M. (2015). Damping analysis of a flexible cantilever beam containing an internal fluid channel: Experiment, modeling and analysis. Journal of Sound and Vibration, 340, 331-342.

[12] Shum KM, Xu YL, Guo WH. Wind-induced vibration control of long span cable-stayed bridges using multiple pressurized tuned liquid column dampers. Journal of wind engineering and industrial aerodynamics. 2008 Feb 1;96(2):166-92.

[13] Min KW, Kim J, Lee HR. A design procedure of two-way liquid dampers for attenuation of wind-induced responses of tall buildings. Journal of Wind Engineering and Industrial Aerodynamics. 2014 Jun 1;129:22-30.

[14] Connor J, Laflamme S. Structural motion engineering. Springer; 2014 Jun 26.

[15] Di Matteo A, Iacono FL, Navarra G, Pirrotta A. Experimental validation of a direct pre-design formula for TLCD. Engineering Structures. 2014 Sep 15;75:528-38.

[16] Min KW, Park CS, Kim J. Easy-to-tune reconfigurable liquid column vibration absorbers with multiple cells. Smart Materials and Structures. 2015 May 18;24(6):065041.

[17] Cammelli S, Li YF, Mijorski S. Mitigation of wind-induced accelerations using Tuned Liquid Column Dampers: Experimental and numerical studies. Journal of Wind Engineering and Industrial Aerodynamics. 2016 Aug 1;155:174-81.

[18] Wu H, Chen A. Seismic Behavior of Glass FRP Wall Panels, 8th International Conference on FRP Composites in Civil Engineering, 2016, Hong Kong.

[19] Di Matteo A, Iacono FL, Navarra G, Pirrotta A. Experimental validation of a direct pre-design formula for TLCD. Engineering Structures. 2014 Sep 15;75:528-38.

[20] Versteeg HK, Malalasekera W. An introduction to computational fluid dynamics: the finite volume method. Pearson Education; 2007.

Table 3.1 *Material property of pultruded GFRP*

Directions	Elastic modulus	Poisson's ratio	Strength	Moment of Inertia
Out-of-plane	5.52 GPa	0.27	162 MPa	6.62×10^6 mm^4
In-plane	6.10 GPa	0.27	130 MPa	1.76×10^8 mm^4

Table 3.2 *Vibration amplitude of GFRP panel (mm)*

	Water height	0 cm	31 cm	62 cm	93 cm
Ground motion 1, 2 cells filled	without water flow	0.576	0.706	0.770	0.921
	with water flow	0.576	0.680	0.724	0.865
Reduction percentage (%)		0.00	-3.75	-6.34	-6.47
Ground motion 1, 4 cells filled	without water flow	0.576	0.726	0.902	0.109
	with water flow	0.576	0.712	0.889	0.104
Reduction percentage (%)		0.00	-5.88	-6.56	-9.46
Ground motion 2, 4 cells filled	without water flow	1.168	1.372	1.575	2.157
	with water flow	1.168	1.295	1.373	1.880
Reduction percentage (%)		0.00	-5.61	-12.84	-12.86
Ground motion 1, 6 cells filled	without water flow	0.584	0.711	0.838	0.965
	with water flow	0.584	0.635	0.660	-
Reduction percentage (%)		0.00	-12.00	-26.92	-
Ground motion 2, 6 cells filled	without water flow	1.168	1.321	1.956	2.261
	with water flow	1.168	-	-	2.056
Reduction percentage (%)		0.00	-	-	0.787

Note: Some data are missing due to a shake table breakdown.

Table 3.3 *Harmonic ground motions of shaking table tests*

Ground Motion	Frequency	Max displacement	Max acceleration
1	10.1Hz	1.85 cm	1.4g
2	12.6Hz	1.93 cm	2.5g

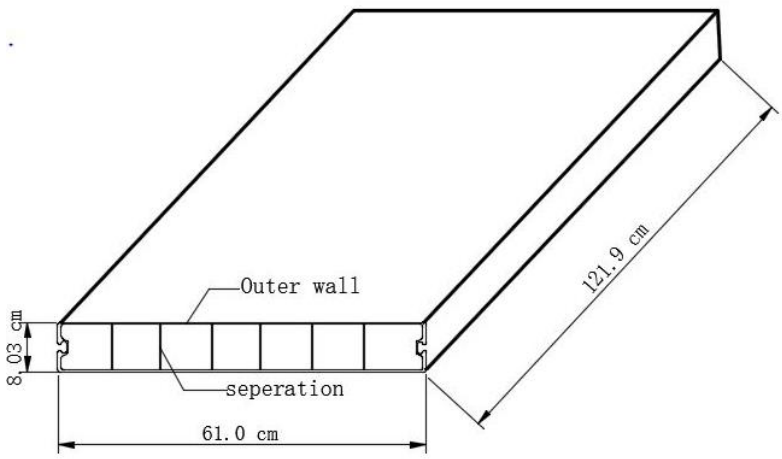

Figure 3.1 *Geometry of the pultruded GFRP panel*

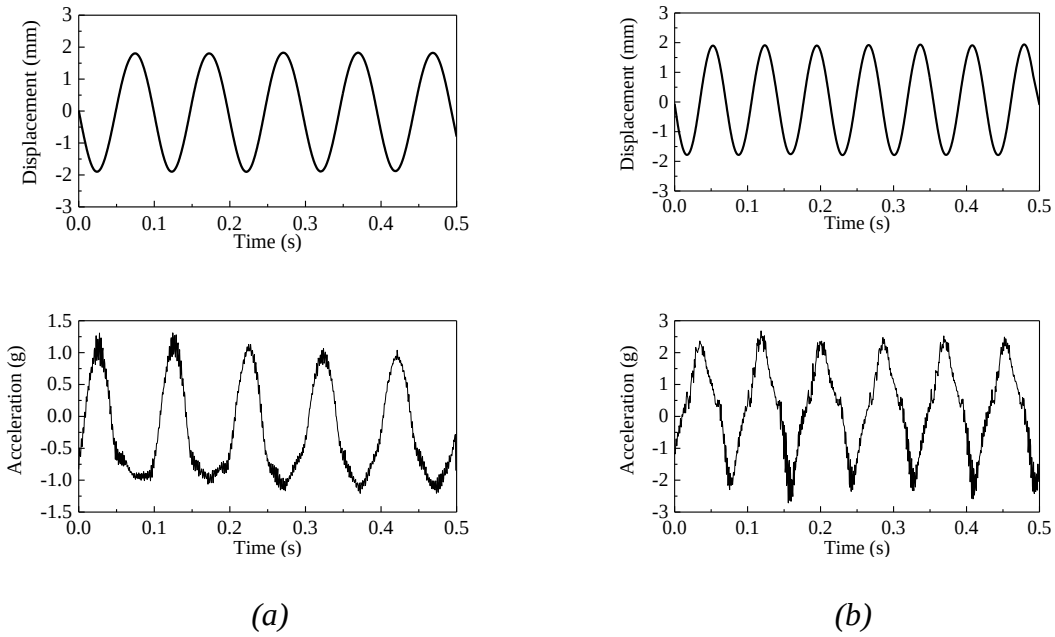

Figure 3.2 *Harmonic ground motions:(a) Ground motion 1; (b) Ground motion 2.*

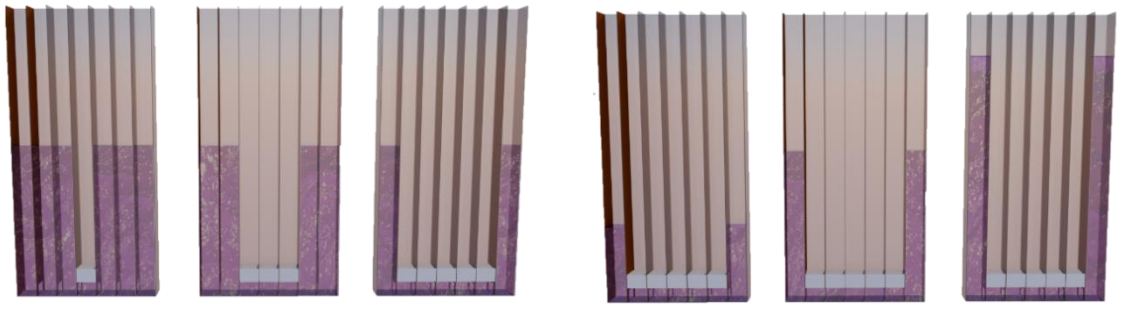

(a) (b)

Figure 3.3 *Combinations of water distribution inside the GFRP panel: (a)Different number of cells opened; (b) Different water heights.*

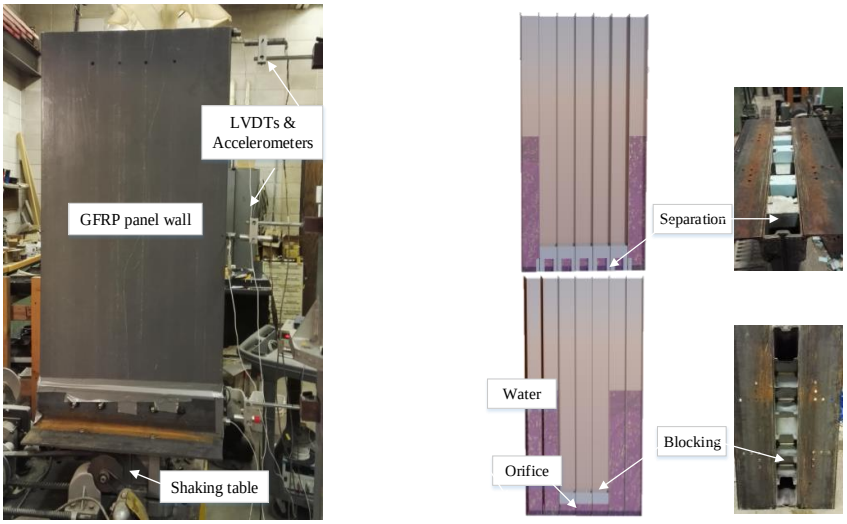

(a) (b)

Figure 3.4 *Shaking table test setup:(a) GFRP panel mounted on the shaking table; (b) Interior of the multi-celled GFRP panel.*

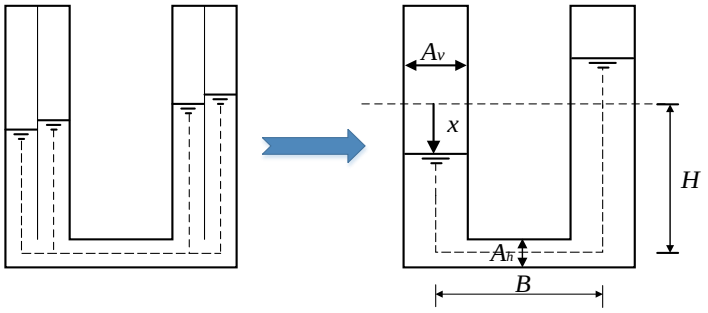

Figure 3.5 *Multi-cells LCVA model in the computation of natural frequencies*

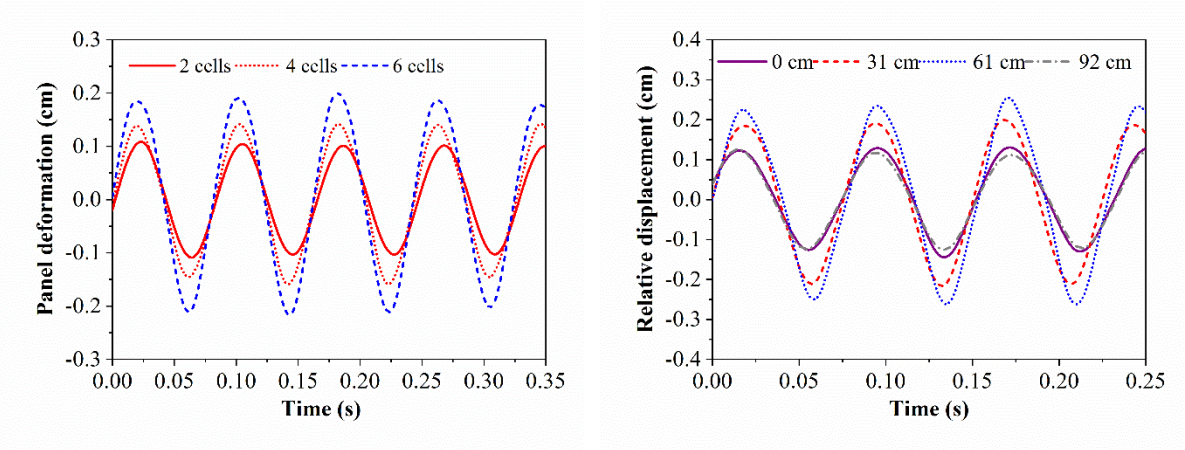

(a) (b)

Figure 3.6 *Comparison of vibration amplitude without separation (a) with different number of cells(Ground Motion 2, water height of 61 cm): (b) with different height of water (Ground motion 1, water in 4 cells).*

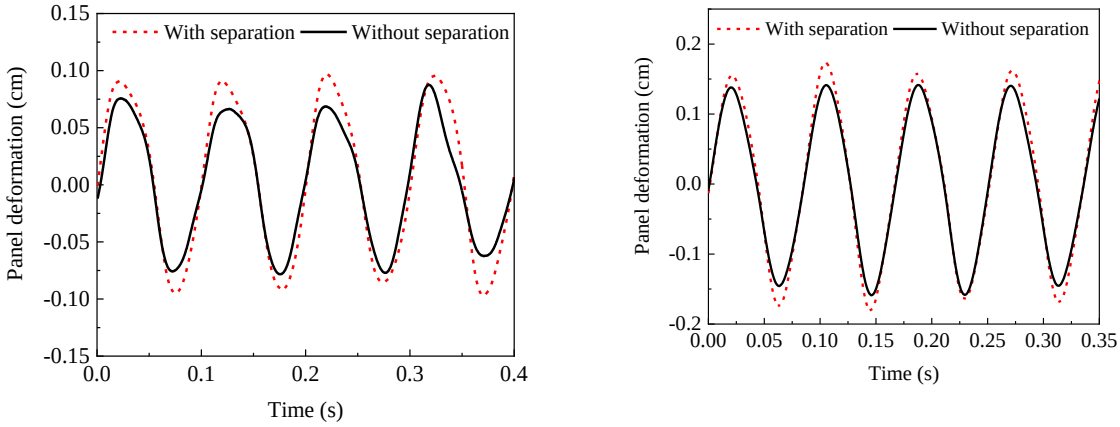

(a) (b)

Figure 3.7 *Comparison of cases without/with separation. (a) Ground motion 1, 4 cells, 61 cm water height; (b) Ground motion 2, 4 cells, 61 cm water height.*

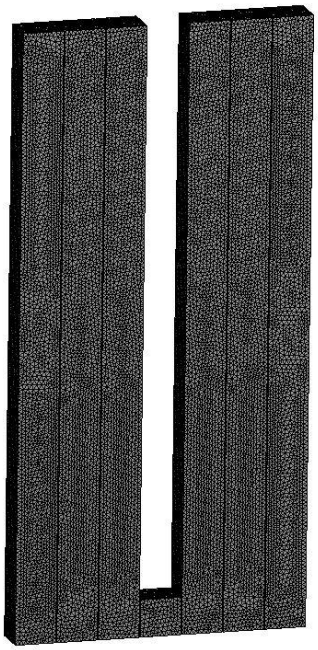

Figure 3.8 *Mesh of the liquid domain in ANSYS FLUENT.*

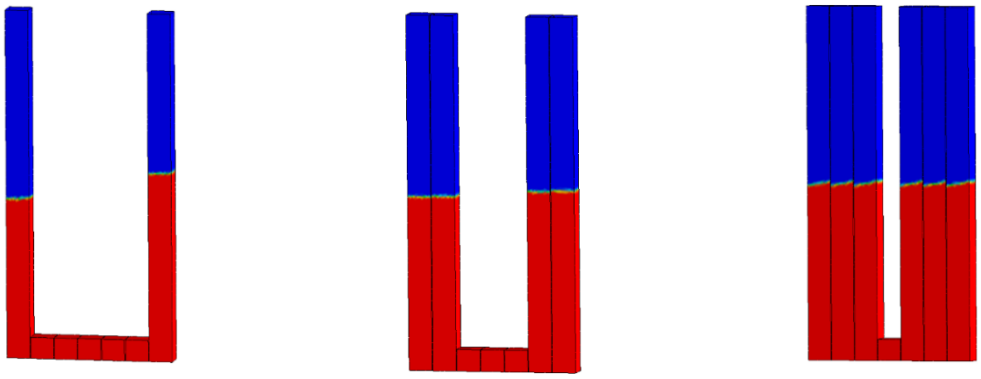

(a) (b) (c)

Figure 3.9 *CFD simulations of water motion (red represents water) (a) 2 cells, 62 cm water height; (b) 4 cells, 62 cm water height; (c) 6 cells, 62 cm water height.*

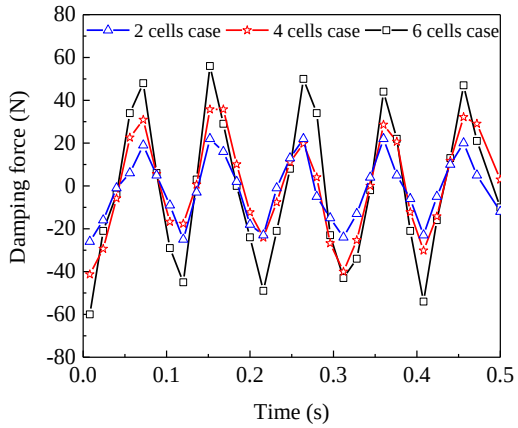

Figure 3.10 *Time series of damping force*

CHAPTER 4. A NONLINEAR DYNAMIC MODEL FOR TUNED LIQUID MULTIPLE COLUMNS DAMPER

A paper submitted to *Journal of Sound and Vibration*

Hao Wu, Liang Cao, Simon Laflamme, and An Chen

4.1 Abstract

The tuned liquid column damper (TLCD), a passive damping device consisting of a large U-tube with oscillating liquid, has been shown to be effective at mitigating structural responses under natural hazards. Aside from their bandwidth-limited mitigation performances, a key limitation in TLCDs is in their large geometries that consume importance space often at prime locations. A solution is to implement multi-columned versions, termed tuned liquid multiple columns dampers (TLMCDs), which have the potential to be tuned to multiple frequencies and occupy less space through the leverage of multiple columns to allow fluid movement. However, mathematical models characterizing their dynamic behaviors must be developed enabling proper tuning and sizing in the design process. In this paper, a new analytical model characterizing a TLMCD as a multiple degree of freedom coupled nonlinear system is presented. The natural frequencies and vibration modes of a TLMCD are identified in close-formed formulations. Results are validated using computational fluid dynamic simulations and show that the analytical model can predict the damper's liquid surface movements as well as its capability to reduce structural vibration when the structure is subjected to motion. A parametric study is conducted to investigate the effect of head loss coefficients, column spacing, cross-section area ratios and column numbers on mitigating structural response. It is found that, while TLMCDs are less effective than traditional TLCDs under an equal liquid mass, they can provide enhanced performance under geometric restrictions.

Keywords: Tuned liquid column damper, structure control, damping system, modal analysis, computational fluid dynamics

4.2 Introduction

Advances in construction methods and materials have led to more flexible structures, thereby raising the demand on reducing vibrations caused by natural hazards. Such vibrations can be mitigated through the incorporation of supplemental damping devices, including passive (Nespoli et al. [1], De et al. [2]), semi-active (Oliveira et al. [3], Cao et al. [4]) and active (Ubertini [5], Wang et al. [6]) systems,. Of interest in this paper are passive systems, which have been widely accepted by the field due to their mechanical robustness and mitigation performance without necessitating power (Symans et al. [7]). Amongst passive systems are tuned mass damper (TMD), which dissipate energy by leveraging inertia. TMDs are typically effective at +/- 15% of their tuned frequency, making them ideal at mitigating wind-induced vibrations (Connor and Laflamme [8]). A variation of TMDs is the tuned liquid column damper (TLCD), which consists of a large U-shaped tube with oscillating liquid. TLCDs leverage gravity in the vertical tubes as the restoring forces and generate damping from the liquid head loss induced by an internal orifice located in the horizontal section of the U-shaped tube. TLCDs have low installation and maintenance costs, high mechanical robustness, and can be used as storage of water (Spencer and Nagarajaiah [9]).

In TLCD modeling, liquid surface displacements are frequently used to represent liquid motion in vertical columns, because the column cross-section sizes are relatively small compared to their lengths. In civil engineering applications, liquid compression is often negligible and ignored, whereby a TLCD with two free liquid surfaces can be modeld as a single degree-of-freedom (SDOF) system. Sakai et al. [10] analytically modeled the liquid motion of a TLCD using a weakly nonlinear equation with nonlinear damping provided by

the internal orifice in the horizontal column. Others have studied numerical solutions for TLCD-structure interactions [11-12]. Transfer functions have also been applied to predict the frequency response of an undamped SDOF structure equipped with a TLCD under harmonic or white noise excitations, assuming that the nonlinear damping term in the TLCD equation can be replaced with an equivalent linear one (Yalla and Kareem [13], Hochrainer [14] and Shum [15]).

Analogous to TMDs, TLCDs are only effective around a fixed frequency range. Variations of TLCDs have been proposed in the last few decades to address such limitation. One example is the bidirectional TLCD, first proposed by Hitchcock [16] and further developed by Razos et al. [17]. Bidirectional TLCDs consist of four vertical columns and function as two TLCDs installed orthogonally, useful at mitigating vibrations from orthogonal directions. Min *et al.* [18] proposed a multi-cell re-tuning passive TLCD, in which the two vertical columns are subdivided into a number of smaller cells that can be sealed or opened to adjust the damper's natural frequency after installation. Recently, the authors [19] introduced the concept of tuned liquid wall damper (TLWD), which is a small multi-capillary TLCD encased in concrete walls. The TLWD is designed to use the liquid for both thermal storage and structural damping. The TLWD is also a multi-cell TLCD. This type of TLCD system is here termed tuned liquid multiple columns dampers (TLMCDs). The critical advantage of TLMCDs is in their capability to be tuned at multiple frequencies, and availability of multiple columns enabling water flow allowing for smaller geometries. To holistically integrate these systems in a structural design, one must develop mathematical models to characterize their dynamic behaviors.

The extension of TLCD models to TLMCD is challenging due to the inherent nonlinear mass matrix in the TLMCD's equations of motion. Razos et al. [17] modeled bidirectional TLCDs through the assumption that both DOFs in the orthogonal directions were uncoupled. Min et al. [18] and Wu et al. [19] modeled TLMCDs by transforming the TLMCD into an equivalent TLCD of the same natural frequency. However, this approximation method introduces unnecessary constraints on the liquid motion by presuming a relationship between liquid surface displacements in different columns. All the above proposed dynamic models are derived from TLCD models, and do not accurately characterize the liquid motion coupling between multiple vertical columns in a TLMCD, where the liquid surface displacement in each column should be treated as an individual DOF. A TLMCD model is also fundamentally different from multiple tuned mass dampers (MTMDs) (Ubertini et al. [20]) or multiple tuned liquid column dampers (MTLCDs) (Gao et al. [21]) models, in which each individual damper is tuned to a different natural frequency to enhance robustness against frequency mistuning with the motion of each individual masses being uncoupled. A TLMCD is an MDOF damper and has multiple coupled natural frequencies and mode shapes. To the best knowledge of the authors, the closest work is that of Hirata and Craik [22], who developed a dynamic model describing the free liquid oscillation in a three-armed vertical columns. However, this model only describes the coupled liquid motion in an undamped and unforced system and cannot characterize nonlinear damping and inertia forces found in a TLMCD.

In this paper, the authors propose a new analytical model to characterize a damped and forced TLMCD system that can extend to unlimited DOFs. Unlike previous TLCD dynamic models, where the liquid damping force is only governed by a single head loss

coefficient, the proposed method captures essential features of the liquid damping forces by dividing them into two parts. The first one is induced by the friction phenomenon in the liquid motion. The second one is due to the head loss of fluid flowing through the orifices.

In the next section, the proposed dynamic model for a TLMCD is introduced. After, the time series of a 4-column and an 8-column TLMCD's liquid surface displacements calculated from the dynamic model are validated against computational fluid dynamics (CFD) simulation results. Subsequently a linearization method for TLMCDs is formulated and the modal shapes at resonance described. Before concluding, a parametric study of head loss coefficients, column spacing, cross-section area ratio and column number on the structural response reduction is conducted numerically. The effectiveness of TLMCDs and TLCDs are compared both under equal liquid mass and geometries.

4.3 Analytical Model

The TLMCD consists of a horizontal column joining multiple vertical columns. Figure 4.1 schematizes an N-column TLMCD, where $\ddot{x}_g$ is the acceleration transmitted from the floor, x_i is the liquid surface displacement in the i^{th} column, h is the initial vertical liquid surface height equal in every columns, l_i is the horizontal centre-to-centre distance between the i^{th} and $i+1^{\text{th}}$ columns, ψ_i is the i^{th} orifice blocking ratio, and Q_{oi}, Q_{fi}, Q_{ei} are the orifice damping force, the friction force between the liquid and column's inner surface, and the liquid inertia force acting on the i^{th} DOF, respecitvely. The Q_{oi}, Q_{fi}, and Q_{ei} are the nonconservative forces in the TLMCD system, which will be discussed later. The analytical model is built upon the following assumptions: 1) all vertical columns are identical; 2) liquid compression and liquid-air interface diffusion are negligible, resulting in a constant total liquid volume during vibrations; and 3) the cross-section sizes of columns are considerably smaller than the total length, resulting in a uniform motion of the liquid surface over the

cross section in each column. Under these assumptions, the N-column TLMCD can be treated as *N*-1 DOFs by allowing the displacement of the last column be dependent on the other motions.

The equations of motion for the TLMCD are derived using the Lagrange equations. Similar methods have also been adopted by Hitchcock [23], Sarkar et al. [24], and Rozas et al. [17] for some variants of TLCDs. Starting with

$$\frac{\mathrm{d}}{\mathrm{d}t}\left(\frac{\partial T}{\partial \dot{x}_i}\right)-\frac{\partial T}{\partial x_i}+\frac{\partial V}{\partial x_i}=Q_i,\quad (i=1,2,...,N-1) \tag{4-1}$$

where $\dot{x}_i$ denotes the liquid velocity in the i^{th} column, t is time, Q_i is the nonconservative force acting on the i^{th} DOF, and T and V are respectively the system's kinematic and potential energy, with

$$V=\frac{1}{2}\rho_l A\mathrm{g}\sum_{i=1}^{N}x_i^2 \tag{4-2a}$$

$$T=\frac{1}{2}\rho_l A\left\{\sum_{i=1}^{N}\dot{x}_i^2\left(h+x_i\right)+\sum_{i=1}^{N-1}\upsilon l_i\left(\sum_{j=1}^{i}\dot{x}_j\right)^2\right\} \tag{4-2b}$$

where ρ_l is the liquid density, A is the column's cross-section area, g is gravitational acceleration, and υ is the cross-section area ratio of the vertical tubes to the horizontal tube. Substituting Eq. (2) into Eq. (1) gives:

$$\begin{aligned}&\rho_l A\left\{\sum_{j=1}^{i}\left(\sum_{k=1}^{N-1}x_k-h-\sum_{k=i}^{N-1}\upsilon l_k\right)\ddot{x}_j+\sum_{j=i+1}^{N-1}\left(\sum_{k=1}^{N-1}x_k-h-\sum_{k=j}^{N-1}\upsilon l_k\right)\ddot{x}_j-\left(h+x_i\right)\ddot{x}_i+\frac{1}{2}\left(\sum_{k=1}^{N-1}\dot{x}_k\right)^2\right.\\&\left.-\frac{1}{2}\dot{x}_i^2-gx_i-g\sum_{k=1}^{N-1}x_k\right\}=Q_i,\ i=1,2,...,N-1\end{aligned} \tag{4-3}$$

The non-conservative force Q_i includes three parts: 1) the damping force Q_{oi} induced by the orifices in the horizontal column; 2) the friction force Q_{fi} between the liquid and column's inner surface; and 3) the liquid inertia force Q_{ei} due to $\ddot{x}_g$.

The damping force Q_{oi} is typically assumed to be proportional to the square of the liquid velocity (Gao *et al*. [11]). The relationship between the head loss coefficient η and orifice blocking ratio ψ has been experimentally studied by Idelchik and Fried [25], Min et al. [26], and Wu et al. [27]. Idelchik and Fried's formula is selected because it models the effect of the orifices and excludes the friction head loss that is modeled separately in our study

$$\eta = \left(\psi + 0.707\psi^{0.375}\right)^2 \left(1-\psi\right)^{-2} \tag{4-4}$$

It should also be noted that the above empirical equation may not be accurate enough since the head loss coefficient is also influenced by external excitation's amplitude and type (white noise, harmonic, seismic signal, etc.), and orifice shapes (Min et al. [26], Colwell and Basu [28]). It is recommended to obtain the relationship experimentally case by case. For a small unit of time, work done by the orifice damping force can be written

$$\mathrm{d}W_o = \sum_{k=1}^{N-1} \rho_l A \left\{ \upsilon \eta_k \left| \sum_{j=1}^{k} \dot{x}_j \right| \left(\sum_{j=1}^{k} \dot{x}_j \right) \sum_{j=1}^{k} \mathrm{d}x_j \right\} \tag{4-5}$$

where η_k is the head loss coefficient for orifice k. The orifice damping force Q_{oi} acting on each DOF is given by:

$$Q_{oi} = \frac{\partial W_o}{\partial x_i} = \sum_{k=i}^{N-1} \rho_l A \left\{ \upsilon \eta_k \left| \sum_{j=1}^{k} \dot{x}_j \right| \left(\sum_{j=1}^{k} \dot{x}_j \right) \right\} \tag{4-6}$$

For laminar flows, the friction resistance is related to the Reynolds number of the flow and is largely insensitive to surface roughness. However, when the flow is turbulent, the

friction force becomes dependent on the roughness of the tube's inner surface. If the liquid in the TLMCD is designed to be contained by coarse pipes, the friction force can be considerably larger than the orifice damping force. For mathematical trackability, we assume that the friction force is proportional to the square of liquid velocity $\dot{x}^2$. An expression for the work done by the friction force over a small unit of time can be obtained:

$$\mathrm{d}W_f = \sum_{k=1}^{N} \rho_l A \left\{ \mu \left| \dot{x}_k \right| \dot{x}_k \left(h + x_k \right) \mathrm{d}x_k \right\} + \sum_{k=1}^{N-1} \rho_l A \left\{ \mu \upsilon l_k \left| \sum_{j=1}^{k} \dot{x}_j \right| \left(\sum_{j=1}^{k} \dot{x}_j \right) \sum_{j=1}^{k} \mathrm{d}x_j \right\} \tag{4-7}$$

where μ is the head loss coefficient due to friction. The friction damping force Q_{fi} acting on each DOF is given by:

$$Q_{fi} = \frac{\partial W_f}{\partial x_i} = \rho_l A \mu \left\{ \left| \dot{x}_i \right| \dot{x}_i \left(h + x_i \right) + \left| \sum_{j=1}^{N-1} \dot{x}_j \right| \left(\sum_{j=1}^{N-1} \dot{x}_j \right) \left(h - \sum_{j=1}^{N-1} x_j \right) + \sum_{k=i}^{N-1} \left(\upsilon l_k \left| \sum_{j=1}^{k} \dot{x}_j \right| \left(\sum_{j=1}^{k} \dot{x}_j \right) \right) \right\} \tag{4-8}$$

Other than the orifice blocking and friction force, any other drastic variations in the liquid velocity may result in additional head loss in the damping system. For example, some recent work (Di Matteo et al. [29]) experimentally found that the transition zone between the vertical columns and the horizontal column is another source of liquid head loss. However, direct formulas for computing this type of head loss are yet to be developed. This effect is not considered in the proposed TLMCD analytical model.

The last non-conservative force is the liquid inertia force Q_{ei} caused by the external acceleration. The work done by the excitation force on the vertical columns is zero, because the sum of vertical liquid masses is constant and the direction of inertia forces is perpendicular to the liquid velocity. The work done by the inertia force Q_{ei} is solely from the motion of the liquid in the horizontal column:

$$\mathrm{d}W_e = \rho_l A \sum_{k=1}^{N-1} \left(\ddot{x}_g l_k \sum_{j=1}^{k} \mathrm{d}x_j \right) \tag{4-9}$$

The inertia force Q_{ei} acting on each DOF is:

$$Q_{ei} = \frac{\partial W_e}{\partial x_i} = \rho_l A \ddot{x}_g(t) \sum_{k=i}^{N-1} l_k \tag{4-10}$$

And the total non-conservative force Q_i acting on the i^{th} degree of freedom is:

$$Q_i = Q_{oi} + Q_{fi} + Q_{ei} \tag{4-11}$$

Combining Eqs. (4-6), (4-8), (4-10) and (4-11), one obtains the equations of motion for a TLMCD:

$$\begin{aligned} &\sum_{j=1}^{i} \left(\sum_{k=1}^{N-1} x_k - h - \sum_{k=i}^{N-1} \upsilon l_k \right) \ddot{x}_j + \sum_{j=i+1}^{N-1} \left(\sum_{k=1}^{N-1} x_k - h - \sum_{k=j}^{N-1} \upsilon l_k \right) \ddot{x}_j - (h + x_i) \ddot{x}_i + \frac{1}{2} \left(\sum_{k=1}^{N-1} \dot{x}_k \right)^2 - \frac{1}{2} \dot{x}_i^2 \\ &-\mathrm{g} x_i - \mathrm{g} \sum_{k=1}^{N-1} x_k = \mu \left| \dot{x}_i \right| \dot{x}_i (h + x_i) + \mu \left| \sum_{k=1}^{N-1} \dot{x}_k \right| \left(\sum_{k=1}^{N-1} \dot{x}_k \right) \left(h - \sum_{k=1}^{N-1} x_k \right) + \sum_{k=i}^{N-1} \upsilon (\mu l_k + \eta_k) \left| \sum_{j=1}^{k} \dot{x}_j \right| \sum_{j=1}^{k} \dot{x}_j \\ &+ \ddot{x}_g(t) \sum_{k=i}^{N-1} l_k, \ (i = 1, 2, ..., N-1) \end{aligned} \tag{4-12}$$

which can be written in matrix form:

$$\mathbf{M}\ddot{\mathbf{x}} + \mathbf{K}\mathbf{x} + \mathbf{F} = \mathbf{0} \tag{4-13}$$

where **M** is a nonlinear mass matrix, **K** is a linear stiffness matrix, and **F** is a nonlinear matrix containing all the other nonlinear terms. The mass matrix $\mathbf{M} \in \mathbb{R}^{N-1 \times N-1}$ is given by:

$$\mathbf{M} = \left(h + \sum_{k=1}^{N-1} x_k \right) \mathbf{I} - \begin{bmatrix} x_1 + h + \upsilon \sum_{k=1}^{N-1} l_k & \upsilon \sum_{k=2}^{N-1} l_k & \upsilon \sum_{k=3}^{N-1} l_k & \cdots & \upsilon l_{N-1} \\ \upsilon \sum_{k=2}^{N-1} l_k & x_2 + h + \upsilon \sum_{k=2}^{N-1} l_k & \upsilon \sum_{k=3}^{N-1} l_k & \cdots & \upsilon l_{N-1} \\ \upsilon \sum_{k=3}^{N-1} l_k & \upsilon \sum_{k=3}^{N-1} l_k & x_3 + h + \upsilon \sum_{k=3}^{N-1} l_k & \cdots & \upsilon l_{N-1} \\ \vdots & \vdots & \vdots & \ddots & \vdots \\ \upsilon l_{N-1} & \upsilon l_{N-1} & \upsilon l_{N-1} & \cdots & x_{N-1} + h + \upsilon l_{N-1} \end{bmatrix} \tag{4-14}$$

where **I** is the identity matrix of appropriate size. From Eq. (12), it is noted that the cross-section area and liquid density are not directly related to the liquid motion, but they may have an indirect influence on the head loss coefficients, and the derivarion of a formulation for determining optimal tuning ratios and head loss coefficients for the TLMCD is complex, because the mass matrix is nonlinear and contains higher order terms.

4.4 Model Validation

In this section, the analytical model is validated against computational fluid dynamic (CFD) simulations on a 4-column and an 8-column TLMCD after a brief verification of the CFD methodology itself by comparing results on a TLCD against reported experimental data in literature.

4.4.1 CFD methodology verification

Computational fluid dynamic (CFD) models are created in ANSYS FLUENT 17.2 software and simulated using a standard k-ε solver, which is widely used to simulate turbulent flow (Versteeg and Malalasekera [30]). The top of the vertical columns is open to allow the liquid to flow freely. No liquid and air diffusion is included. To account for the unevenness of the liquid surface in the vertical columns, the liquid surface displacement is defined as the distance between the horizontal centerline of the liquid surface and its original steady state position.

The CFD methodology is first verified against experimental data published in Wu *et al.* [22]. In their study, a TLCD was directly attached to a shaking table and subjected to a harmonic ground acceleration $\ddot{x}_g = 4\sin(0.492t)\,\text{cm/s}^2$. The cross-section area of the TLCD tube was reported to be 15 x 15 cm^2, and the horizontal and vertical lengths were 85 cm and 63.5 cm, respectively. The orifice blocking ratio varied from 20% to 80% to obtain a relationship with the TLCD's head loss coefficient. The experimented system was modeled

by generating meshes with a maximum element length of 1 cm to capture features associated with liquid motion in transition areas such as elbows and tee sections. Since the TLCD material is unknown, the roughness height of the pipe was set to 0.002 mm. Results from the CFD simulation are compared against these experimental results in Table 4.1. Results show slightly lower maximum liquid surface amplitudes, but no more than 10%, showing an overall good agreement between both the experimental and CFD simulation results.

4.4.2 Validation of analytical model

The proposed analytical model in Section 4.2 is validated on 4-column and 8-column TLMCDs using the same CFD methodology as described in Section 4.4.1. The geometry parameters and damping coefficients of both systems are listed in Table 4.2. All the orifices have an identical blocking ratio of 20%, and the orifice head loss coefficient η is determined using Eq. (4). Liquid surface displacements are first calculated using the analytical model and then compared to the CFD results.

Two simulation cases are considered: free oscillation and forced vibration. Starting with the 4-column TLMCD under free oscillation, the initial condition on the liquid surface displacements in the four vertical columns are set at three quarters of the initial liquid surface height: $x_1(0) = x_2(0) = 0.385$ m, and $x_3(0) = x_4(0) = -0.385$ m. Figure 4.2 (a) and (b) plot time series data of the four columns' liquid surface displacements from the analytical model and the CFD simulations. There is good agreement between the model and simulations results. For the forced vibration case of the 4-column TLMCD, a harmonic floor acceleration $\ddot{x}_g = 0.37\sin(2.46t)\,\mathrm{m/s^2}$ is used as the forcing, where the vibration frequency is at the first natural frequency of the 4-column TLMCD, and the acceleration amplitude is selected arbitrarily to provide a reasonable fluid motion. Figure 4.3 shows the liquid motion amplitudes under this

harmonic excitation: the liquid heights in the four columns decrease almost linearly from one end to the other. Figure 4.4 (a) and (b) are plots of the forced vibration results for the liquid surface displacements for all the columns, also showing a good agreement between the model and simulation results.

The 8-column TLMCD is validated using the same methodology as used for the 4-column TLCD. For the free oscillation, the initial condition on the liquid surface displacements are set to $x_i(0) = 0.9$ m for $i = 1, 2, 3 \ldots 8$. Figure 4.5 plots the time series data comparing the results. The CFD simulation and analytical solutions of the liquid surface displacements match very well for the first 2 seconds. After that, as the system energy diminishes, the error slightly increases, but the analytical model can still capture the oscillation amplitude. In the forced vibration case, the TLMCD is subjected to a harmonic floor acceleration $\ddot{x}_g = 0.6\sin(0.934t)$ m/s^2, where the vibration frequency is close to the first natural frequency of the TLMCD, and the acceleration amplitude is selected arbitrarily to provide a reasonable fluid motion. The liquid motion is shown in Figure 4.6. Results show a good agreement between the model and simulation results. It can also be observed that the liquid motion is almost at the same phase in all columns, with a slight decrease in phase from the left-most to the right-most column.

4.5 Modal Analysis

4.5.1 Weak nonlinearity of TLMCD

The nonlinear mass matrix of the TLMCD model makes it difficult to extract natural frequencies analytically. For an undamped free vibration case, it is possible to calculate the system's natural frequencies using invariant points, where these frequencies are solely determined by the system energy regardless of initial phase conditions (Hirata and Craik

[20]). However, this method is not applicable to damped models and those under forced vibrations, because the system energy is time-varying and invariant points are not available.

The stability of a nonlinear system's natural frequencies can be measured by the fluctuation range of natural frequencies, and a small range indicates that frequencies are consistent under various situations. Mechanical systems with weak nonlinearity, in which the nonlinear terms in the differential equations of motion are much smaller than the linear ones, tend to have stable frequency response functions (Vakakis and Ewins [31]). Various numerical simulations suggest that a TLMCD is a weakly nonlinear system and has stable natural frequencies and mode shapes under different damping and excitation amplitudes. Natural frequencies of TLMCDs can be identified numerically through frequency response curves under a harmonic frequency sweep. For example, the vibration amplitudes of the displacements of the first two columns of 4-column TLMCD with an equal column spacing of 1 m and an initial liquid height of 1 m under harmonic vibrations are obtained using Equations (12). Figure 4.8 plots the frequency responses under various orifice blocking ratios ψ. It can be observed that increasing the orifice blocking ratios only reduces the natural frequencies of the TLMCD by less than 1%, as illustrated in Figure 4.10 (a). Another factor that may influence natural frequencies is the total energy of the system, because a TLMCD's natural frequencies may be input amplitude dependent given its nonlinearity. Figure 4.9 plots the frequency responses under various excitation inputs. It is found that increasing the acceleration input only affects the frequency response amplitude but not the natural frequencies themselves; both the two natural frequencies stay unchanged, as illustrated in Figure 4.10 (b). It can be concluded that a TLMCD is weakly nonlinear and its natural frequencies can be estimated within a reasonable range independently of damping and system

energy. The next section discusses how these natural frequencies and corresponding mode shapes can be analytically computed.

4.5.2 Linearization method

The nonlinearity of the TLMCD is attributed to the coupled liquid motion in multiple vertical columns. For a geometrically symmetric TLMCD, it is noticed from both numerical and CFD simulations that opposite columns have opposite liquid surface displacements. Based on this observation, the equations of motion for symmetrical TLMCDs can be linearized, and the number of natural frequencies of an N-column symmetrical TLMCD can be reduced to $N/2$. The linearized constant mass and stiffness matrices are:

$$\mathbf{M}_C = \begin{bmatrix} \upsilon\left(2\sum_{k=1}^{N/2} l_k - l_{N/2}\right)+2h & \upsilon\left(2\sum_{k=2}^{N/2} l_k - l_{N/2}\right) & \upsilon\left(2\sum_{k=3}^{N/2} l_k - l_{N/2}\right) & \cdots & \upsilon l_{N/2} \\ \upsilon\left(2\sum_{k=2}^{N/2} l_k - l_{N/2}\right) & \upsilon\left(2\sum_{k=2}^{N/2} l_k - l_{N/2}\right)+2h & \upsilon\left(2\sum_{k=3}^{N/2} l_k - l_{N/2}\right) & \cdots & \upsilon l_{N/2} \\ \upsilon\left(2\sum_{k=3}^{N/2} l_k - l_{N/2}\right) & \upsilon\left(2\sum_{k=3}^{N/2} l_k - l_{N/2}\right) & \upsilon\left(2\sum_{k=2}^{N/2} l_k - l_{N/2}\right)+2h & \cdots & \upsilon l_{N/2} \\ \vdots & \vdots & \vdots & \ddots & \vdots \\ \upsilon L_{N/2} & \upsilon L_{N/2} & \upsilon l_{N/2} & \cdots & \upsilon l_{N/2}+2h \end{bmatrix}_{N/2\times N/2} \tag{4-15}$$

$$\mathbf{K}_C = \begin{bmatrix} 2\mathrm{g} & 0 & \cdots & 0 \\ 0 & 2\mathrm{g} & \cdots & 0 \\ \vdots & \vdots & \ddots & \vdots \\ 0 & 0 & \cdots & 2\mathrm{g} \end{bmatrix}_{N/2\times N/2} \tag{4-16}$$

Notice that the mass and stiffness matrices are symmetrical as well, as a result, there exists $N/2$ real eigenvalues (natural frequencies). This linearized method is accurate for calculating the liquid motion when TLMCDs are subjected to harmonic or white noise accelerations, where the liquid motion is mostly decoupled between opposite column pairs.

To better describe the linearization method, the first mode shape of a TLMCD is shown in Figure 4.11. The fundamental natural frequency and mode shape of a TLMCD can be expressed physically using the natural frequency formula of liquid column vibration

absorbers (LCVAs). A LCVA is a variant of a TLCD where the cross-section area of the horizontal column is less than that of vertical columns (Watkins [32]). A TLMCD's motion can be simplified as a combination of several independent LCVAs with the same natural frequency. The effective length of a LCVA is given as (Hitchcock [23]):

$$l_e = \upsilon l + 2h \tag{4-17}$$

where l and h are the horizontal and vertical lengths of a LCVA, respectively. If an N-column symmetrical TLMCD is separated into $N/2$ individual LCVAs, their common natural frequency can be calculated using the following equations:

$$\sum_{j=1}^{N/2} \alpha_j = 1, \tag{4-18}$$

$$2h + \upsilon\left(\left(\sum_{i=j+1}^{N/2-1} 2l_i\right) + l_{N/2}\right)/\alpha_j + 2\upsilon l_j / (\sum_{i=1}^{j} \alpha_j) = l_e,\ j = 1, 2, ..., N/2 \tag{4-19}$$

$$\omega = \sqrt{\frac{2g}{l_e}} \tag{4-20}$$

where α_j is the j^{th} cross-section area proportion in the horizontal middle column, l_e is the effective length of all LCVAs, and ω is the fundamental natural frequency of the TLMCD. Solving the above equations for the fundamental frequency is straightforward if negative α_j values are always discarded. It is verified that the result obtained from above equations is the same as that solved using the matrices forms. In higher order vibration modes, α_j values can be negative and the calculation process is more complex.

Asymmetric TLMCDs have stronger nonlinearities, and the natural frequencies can only be obtained using an approximate method. If we neglect the nonlinear terms and the displacements in the mass matrix (Eq. (13)), the natural frequencies are stable since the mass and stiffness matrices become constant. In this situation, there are a total of N-1 natural

frequencies for an asymmetric N-column TLMCD. This method applies for small liquid displacements, and it should be used to approximately predict the natural frequencies, but not the actual liquid motion. Under this condition, the constant mass and stiffness matrices are:

$$\mathbf{M}_C = \begin{bmatrix} 2h+\upsilon\sum_{k=1}^{N-1} l_k & h+\upsilon\sum_{k=2}^{N-1} l_k & h+\upsilon\sum_{k=3}^{N-1} l_k & \cdots & h+\upsilon l_{N-1} \\ h+\upsilon\sum_{k=2}^{N-1} l_k & 2h+\upsilon\sum_{k=2}^{N-1} l_k & h+\upsilon\sum_{k=3}^{N-1} l_k & \cdots & h+\upsilon l_{N-1} \\ h+\upsilon\sum_{k=3}^{N-1} l_k & h+\upsilon\sum_{k=3}^{N-1} l_k & 2h+\upsilon\sum_{k=3}^{N-1} l_k & \cdots & h+\upsilon l_{N-1} \\ \vdots & \vdots & \vdots & \ddots & \vdots \\ h+\upsilon l_{N-1} & h+\upsilon l_{N-1} & h+\upsilon l_{N-1} & \cdots & 2h+\upsilon L_{N-1} \end{bmatrix}_{N-1\times N-1} \tag{4-21}$$

$$\mathbf{K}_C = \begin{bmatrix} 2\mathrm{g} & \mathrm{g} & \cdots & \mathrm{g} \\ \mathrm{g} & 2\mathrm{g} & \cdots & \mathrm{g} \\ \vdots & \vdots & \ddots & \vdots \\ \mathrm{g} & \mathrm{g} & \cdots & 2\mathrm{g} \end{bmatrix}_{N-1\times N-1} \tag{4-22}$$

4.5.3 Numerical examples

The linearization method for extracting natural frequencies and mode shapes is illustrated using the 4-column and the 8-column TLMCD examples described in Section 4.4.2.

The linearized mass and stiffness matrices for the 4-column TLMCD are:

$$\mathbf{M} = \rho_l A \begin{bmatrix} \upsilon(2l_1+l_2)+2h & \upsilon l_2 \\ \upsilon l_2 & \upsilon l_2+2h \end{bmatrix} \tag{4-23}$$

$$\mathbf{K} = \rho_l A \begin{bmatrix} 2\mathrm{g} & 0 \\ 0 & 2\mathrm{g} \end{bmatrix} \tag{4-24}$$

The resulting mode shapes are the eigenvectors are:

$$\begin{bmatrix} \phi_1 & \phi_2 \end{bmatrix} = \begin{bmatrix} -0.924 & -0.383 \\ -0.383 & 0.924 \end{bmatrix} \tag{4-25}$$

From this linearization method, the 4-column TLMCD is separated into two smaller LCVAs that share the same natural frequency. The cross-sectional area proportions of these two smaller horizontal columns, α_1 and α_2, respectively, can be obtained by equalizing the effective lengths of the two LCVAs (Eq. (4-19)). Two different sets of α_1 and α_2 values will be produced, corresponding to two natural frequencies of the 4-column TLMCD. Figure 4.12 shows the liquid flow inside the 4-column TLMCD when the damper is excited by a sinusoidal acceleration at its first and second natural frequencies, respectively. It is observed that α_2 is negative in the second mode shape, where the flow direction in the middle horizontal column is reversed and contrary to the fluid flow direction in the larger LCVA.

To validate the robustness and accuracy of the natural frequency analytical method, column spacings in the 4-column TLMCD are altered. Frequency response curves of the first column liquid surface displacement obtained using the numerical methods described in Section 4.2.2 are shown in Figure 4.13. It is found that there are two distinctive natural frequencies for symmetric cases (e.g., case 2 in Table 4.3) and three for the asymmetric cases (e.g., case 5 in Table 4.3). The comparison between the identified analytical and numerical frequencies under various column spacings show a good agreement, as the differences are all less than 2%.

Results for the equally spaced 8-column TLMCD (Case 7 in Table 4.3) show good agreement between the analytical and numerical frequencies, as illustrated in Figure 4.15. The first analytical mode shape, as illustrated in Figure 4.14, also correlates to that of the CFD simulation (see Figure 4.5). Higher order mode shapes can be described by the corresponding mode shape coefficients. Given the same total horizontal length, increasing the column number will significantly lower all the natural frequencies. If required, this can be

compensated, for example, by enlarging the horizontal tube's cross-section. The next section presents a parametric study to further the understanding of TLMCD alterations.

4.6 Parametric Study of Damping Performance on a SDOF Structure

The damping performance of a TLCD or a TLMCD is usually measured by its capability to reduce structural responses. In this section, the transfer function H_1, defined as the ratio of the dynamic displacement amplitude to the static structural response (Eq. (4-26)), is used to evaluate the TLMCD's damping capacity. The main mitigation objective is to lower the maximum H_1 value across all frequencies.

$$H_1 = \frac{(x_s)_{\max}}{p_0 / k_s} \tag{4-26}$$

where x_s is the SDOF structure displacement, p_0 is the floor harmonic excitation amplitude, and k_s is the structural stiffness. We apply harmonic ground motions to the TLMCD-structure system and evaluate the parametric effects, including tuning ratios, head loss coefficients, and column configurations, on H_1.

In literature on TLCDs, analytical transfer functions for structural response are only available after the nonlinear damping force due to the head loss is linearized. Because the system of interest is nonlinear, H_1 is numerically evaluated using the steady state of structural response. The equation of motion governing the SDOF system equipped with a TLMCD is written

$$m_s\ddot{x}_s + \rho_l A\left(Nh + \sum_{i=1}^{N-1} l_i / \upsilon\right)\ddot{x}_s + \rho_l A\sum_{i=1}^{N-1}\left(\ddot{x}_i \sum_{j=1}^{i} l_j\right) + c_s\dot{x}_s + k_s x_s = p_0 \sin(\omega_f t) \tag{4-27}$$

where c_s is the structural damping coefficient, ω_f is the excitation frequency. Eqs. (4-12) and (27) are numerically solved to estimate H_1.

In the following parametric studies, the configuration of the TLMCD, illustrated in Fig. 16, is as follows. The mass ratio γ is 1%, and the initial liquid heights in the vertical columns are set to a uniform value h = 0.853 m. The structural characteristics of the SDOF structure are taken as m_s = 386100 kg, ω_s = 1.1 rad/s, and $\xi_s = 0.05$. A harmonic force with an amplitude of $p_0 = 0.001 m_s g$ and with frequencies ranging from 80% to 120% of the TLMCD's first natural frequency, which can be identified using the method described in Section 4, is applied to the structure. The effect of column spacing l_i, cross-section area ratio υ, orifice head loss coefficient η, and column number N on the structural vibration responses are investigated.

4.6.1 Tuning ratios

The TLMCD's tuning ratio χ is defined as the ratio of the damper's undamped first natural frequency to the structure's natural frequency. There are two parameters that can be used to tuned the TLMCD's first natural frequency: the cross-section area ratio υ and the column spacing l_i.

To study the effect of column spacing, we set parameters υ, η and h constant and vary l_i. The relationship between l_i and υ and χ is estimated using the linearization method in Section 4.5 and plotted in Figure 4.17 (a), showing that as l_i increases χ decreases. The task is repeated for υ, with the behavior plotted in Figure 4.17 (b), exhibiting χ decreasing for υ increasing.

The effect of the variables on H_1 is investigated on a 4-column and an 8-column TLCD of parameters listed in Table 4.4. Define $\rho = \omega_f/\omega_s$ as the frequency ratio, Figure 4.18 plots H_1 versus ρ curves for various values of l_i, and Figure 4.19 plots H_1 versus ρ curves for various values of υ. Results show that there exists an optimal tuning ratio that can be obtained

through tuning either or both parameters. This optimal value is characterized by two peaks of equal height.

It can be noted that the 4-column TLMCD is more sensitive to variations in l_i and υ than the 8-column one, and that the 8-column TLMCD is less effective around resonance.

4.6.2 Head loss coefficients

Here, values for l_i and υ are fixed, taken at the optimal tuning ratios found in the previous section. Simulation parameters for the 4-column and 8-column TLMCDs are listed in Table 4.5. The head loss coefficient for each orifice is taken as identical and altered simultaneously. Their effects on H_1 are plotted in Figure 4.20. Two invariant points can be observed in the transfer functions that are independent of the head loss coefficients. It follows that the optimized head loss coefficients are those that result in the invariant points being the highest in H_1. It can also be noted that, because it has fewer orifices, the 4-column TLMCD requires larger head loss coefficients ($\eta = 2$) to minimize H_1 than does the 8-column TLMCD ($\eta = 0.5$).

4.6.3 Number of columns

The effect of the number of columns on the TLMCDs of parameters listed in Table 4.6 and Table 4.7 are compared against each other. The minimized H_1 under various column numbers are plotted in Figure 4.21 (a) for an equal mass and in Figure 4.21 (b) for an equal column size throughout the studied configurations. The minimized H_1 were obtained by adjusting υ to obtain two equal peaks in the transfer function, and then adjusting the head loss coefficients to minimize the height of the peaks.

Results show that, when the total mass of the TLMCD is maintained constant, reducing the number of columns provides a better mitigation performance around resonance, but a slightly worse one in other frequency ranges. This is attributed to more liquid mass

present in the horizontal column, making the device more effective (Gao *et al.* [22]). For a constant mass, a TLMCD will not over-perform a TLCD (2-column TLMCD). Conversely, when the mass ratio is allowed to vary but the size of the columns is maintained constant (Figure 4.21 (b)), increasing the number of columns provides better mitigation. This can be attributed to the larger mass ratio. In this case, a TLMCD could be designed to over-perform a TLCD. Overall, it can be concluded from results that, given a space constraint, a TLMCD could provide higher mitigation benefits compared with a TLCD. Remark that, not shown, it was observed that increasing the number of columns beyond 12 only had a non-significant effect to the overall response.

4.6.4 Structural mitigation using higher order modes of TLMCDs

The parameters of TLMCDs using the second vibration mode for structure mitigation are listed in Table 4.8. Higher order vibration modes of TLMCDs usually have smaller effective masses, and as a result, their damping ability is lower than the TLMCD's first vibration mode. Tuning higher order natural frequencies to the natural frequency of the structure also requires significantly increasing the υ value, resulting in reduction of the percentage of liquid mass in the horizontal column and deterioration of TLMCDs' damping capability. The H_1 curves of 4-column and 8-column TLMCDs with different cross-section ratios are shown in Figure 4.22, where $\upsilon = 5.7$ and $\upsilon = 4.9$ correspond to the minimized cases, respectively. Comparing to cases using the first vibration mode (Figure 4.19), the structure yields a larger displacement response. Note that the distances between higher order frequencies are much closer to each other than the first two frequencies, and the transfer functions curves are possibly influenced by multiple vibration modes.

4.7 Conclusions

In this paper, a nonlinear dynamic model for TLMCD is derived using Lagrange equations, which can characterize both nonlinear orifice and friction damping forces. Both the analytical model and CFD method are used to study two typical TLMCDs. Good correlations of liquid motion between the two results under both free oscillation and forced vibration prove the accuracy of the derived analyticla model. Numerical simulation shows that the analytical model of the TLMCD is weakly nonlinear, and the influence of damping and system energy on the natural frequencies of the TLMCD is limited. A simplified linearization method is developed to calculate the natural frequencies TLMCD, which is validated by the results from frequency response curves. The shape of the fundamental mode of TLMCD can be physically explained using the concept of the effective length from LCVAs.

A parametric study using the analytical model is conducted to evaluate the influence of various parameters on the reduction of structural vibration responses under harmonic excitations. It is found that the tuning ratio affects the shape of transfer function curve and can be adjusted to equalize the curve's two peaks by varying the column spacing or cross-section area ratio. Head loss coefficients control the damping force in TLMCD, which can be optimized for a fixed TLMCD configuration to minimize the structural response at resonance. The number of columns determines the portion of horizontal liquid mass in the TLMCD and indirectly influences the peak values of the transfer function curve.

It can be concluded that a two-column TLCD can be treated as a special type of TLMCD with the smallest number of columns. With the same mass ratio and liquid height, a TLMCD with more vertical columns is less effective than a TLCD, because the TLMCD has

smaller horizontal mass. However, when keeping the geometries constant, a TLMCD with more columns over-performs a TLCD, because the TLMCD has a larger mass ratio.

This study focused on structural mitigation using the first vibration mode of TLMCDs. Although higher order vibration modes have less effective mass and may not be as effective as the first mode, it is still possible to combine a TLMCD's multiple vibration modes to mitigate structural responses, which will be included in a future study.

4.8 References

[1] A. Nespoli, D. Rigamonti, M. Riva, E. Villa, F. Passaretti, Study of pseudoelastic systems for the design of complex passive dampers: Static analysis and modeling, Smart Mater. Struct. 25 (2016). https://doi:10.1088/0964-1726/25/10/105001.

[2] S. De, S.F. Wojtkiewicz, E.A. Johnson, Efficient optimal design and design-under-uncertainty of passive control devices with application to a cable-stayed bridge, Struct. Control Heal. Monit. 24 (2017). https://doi:10.1002/stc.1846.

[3] F. Oliveira, M.A. Botto, P. Morais, A. Suleman, Semi-active structural vibration control of base-isolated buildings using magnetorheological dampers, J. Low Freq. Noise, Vib. Act. Control. 0 (2017) 1461348417725959. https://doi:10.1177/1461348417725959.

[4] L. Cao, A. Downey, S. Laflamme, D. Taylor, J. Ricles, Variable friction device for structural control based on duo-servo vehicle brake: Modeling and experimental validation, J. Sound Vib. 348 (2015) 41–56. https://doi:10.1016/j.jsv.2015.03.011.

[5] F. Ubertini, Active feedback control for cable vibrations, Smart Struct. Syst. 4 (4) (2008) 407-428. https://doi:10.12989/sss.2008.4.4.407

[6] X. Wang, F. Blaabjerg, M. Liserre, Z. Chen, J. He, Y. Li, An active damper for stabilizing power-electronics-based AC systems, IEEE Trans. Power Electron. 29 (2014) 3318–3329. https://doi:10.1109/TPEL.2013.2278716.

[7] M.D. Symans, F.A. Charney, A.S. Whittaker, M.C. Constantinou, C.A. Kircher, M.W. Johnson, R.J. Mcnamara, Energy Dissipation Systems for Seismic Applications: Current Practice and Recent Developments, J. Struct. Eng. 134 (2008) 3–21. https://doi:10.1061/(ASCE)0733-9445(2008)134:1(3).

[8] J. Connor, S. Laflamme, Structural motion engineering, Springer, New York, 2014.

[9] B. F. Spencer Jr, S. Nagarajaiah, State of the art of structural control, J. Struct. Eng. 129 (2003) 845–856. https://doi:10.1061/(ASCE)0733-9445(2003)129:7(845).

[10] F. Sakai, S. Takaeda, T. Tamaki, Tuned liquid column damper-new type device for suppression of building vibrations, Int. Conf. on Highrise Buildings, 1999, 25-27.

[11] H. Gao, K.S.C. Kwok, B. Samali, Characteristics of multiple tuned liquid column dampers in suppressing structural vibration, Eng. Struct. 21 (1999) 316–331. https://doi:10.1016/S0141-0296(97)00183-1.

[12] K.W. Min, H.S. Kim, S.H. Lee, H. Kim, S. Kyung Ahn, Performance evaluation of tuned liquid column dampers for response control of a 76-story benchmark building, Eng. Struct. 27 (2005) 1101–1112. https://doi:10.1016/j.engstruct.2005.02.008.

[13] S.K. Yalla, A. Kareem, Optimum Absorber Parameters for Tuned Liquid Column Dampers, J. Struct. Eng. 126 (2000) 906–915. https://doi:10.1061/(ASCE)0733-9445(2000)126:8(906).

[14] M.J. Hochrainer, Tuned liquid column damper for structural control, Acta Mech. 175 (2005) 57–76. https://doi:10.1007/s00707-004-0193-z.

[15] K.M. Shum, Tuned vibration absorbers with nonlinear viscous damping for damped structures under random load, J. Sound Vib. 346 (2015) 70–80. https://doi:10.1016/j.jsv.2015.02.003.

[16] P.A. Hitchcock, K.C.S. Kwok, R.D. Watkins, B. Samali, Characteristics of liquid column vibration absorbers (LCVA) - I, Eng. Struct. 19 (1997) 126–134. https://doi:10.1016/S0141-0296(96)00042-9.

[17] L. Rozas, R. L. Boroschek, A. Tamburrino, M. Rojas, A bidirectional tuned liquid column damper for reducing the seismic response of buildings, Struct. Control Health Monit. 23 (2016) 621-640. https://doi: 10.1002/stc.1784

[18] K.W. Min, C.S. Park, J. Kim, Easy-to-tune reconfigurable liquid column vibration absorbers with multiple cells, Smart Mater. Struct. 24 (2015) 1–12. https://doi:10.1088/0964-1726/24/6/065041.

[19] H. Wu, L. Cao, A. Chen, S. Laflamme, A novel tuned liquid wall damper for multi-hazard mitigation, Proc. SPIE - Int. Soc. Opt. Eng. 10164 (2017). https://doi:10.1117/12.2261632.

[20] F. Ubertini, G. Comanducci, S. Laflamme, A parametric study on reliability-based tuned-mass damper design against bridge flutter, J. Vib. Control. 23 (2017) 1518–1534. https://doi:10.1177/1077546315595304.

[21] H. Gao, K.S.C. Kwok, B. Samali, Characteristics of multiple tuned liquid column dampers in suppressing structural vibration, Eng. Struct. 21 (1999) 316–331. https://doi:10.1016/S0141-0296(97)00183-1.

[22] K. Hirata, A.D.D. Craik, Nonlinear oscillations in three-armed tubes, Eur. J. Mech. B/Fluids. 22 (2003) 3–26. https://doi:10.1016/S0997-7546(02)00003-1.

[23] P. A. Hitchcock, K. C. S. Kwok, R. D. Watkins, B. Samali, The effectiveness of a multiple liquid column vibration absorber, Proc. of the 4th Workshop on Wind Engineering (1994) 81-86.

[24] A. Sarkar, O.T. Gudmestad, Pendulum type liquid column damper (PLCD) for controlling vibrations of a structure - Theoretical and experimental study, Eng. Struct. 49 (2013) 221–233. https://doi:10.1016/j.engstruct.2012.10.023.

[25] I. E. Idelchik, E. Fried, Handbook of hydraulic resistance, 2nd ed, Hemisphere Publishing Corp., Washington DC, 1986.

[26] K.W. Min, Y.W. Kim, J. Kim, Analytical and experimental investigations on performance of tuned liquid column dampers with various orifices to wind-excited structural vibration, J. Wind Eng. Ind. Aerodyn. 139 (2015) 62–69. https://doi:10.1016/j.jweia.2015.01.014.

[27] J.C. Wu, M.H. Shih, Y.Y. Lin, Y.C. Shen, Design guidelines for tuned liquid column damper for structures responding to wind, Eng. Struct. 27 (2005) 1893–1905. https://doi:10.1016/j.engstruct.2005.05.009.

[28] S. Colwell, B. Basu, Investigations on the performance of a liquid column damper (LCD) with different orifice diameter ratios, Can. J. Civ. Eng. 33 (2006) 588–595. https://doi:10.1139/l06-016.

[29] H. K. Versteeg, W. Malalasekera, An introduction to computational fluid dynamics: the finite volume method, 2nd ed, Pearson Education, New York, 2007.

[30] A. Di Matteo, F. Lo Iacono, G. Navarra, A. Pirrotta, Numerical validation of an approximate formulation for the design of TLCD, AIMETA13 (2013) 1061–1068.

[31] R.D. Watkins, Tests on tuned liquid column dampers for tall structures, Proc. Int. Conf. on Steel and Aluminium Structures, 1991.

[32] A.F. Vakakis, D.J. Ewins, Effects of weak non-linearities on modal analysis, Mech. Syst. Signal Process. 8 (1994) 175–198. https://doi:10.1006/mssp.1994.1015.

Table 4.1 *Comparison of liquid surface amplitudes (cm) between CFD and test results [22]*

Orifice blocking ratio ψ	0.2	0.4	0.6	0.8
Experimental results	15.8	13.1	9.2	4.3
CFD simulation results	14.3	12.2	8.3	4.3
Difference (%)	9.5	7.3	9.7	0

Table 4.2 *System parameters for 4-column and 8-column TLMCDs*

System Parameters	Cross-section Area	Orifice head loss coefficient	Friction head loss coefficient	Initial liquid surface height	Column Spacing
4-column	15 x 15 cm^2	0.54	0.2	0.5 m	0.50 m
8-column	30 x 30 cm^2	0.54	0.1	0.9 m	1.50 m

Table 4.3 *Comparison of numerical and analytical natural frequencies for TLMCDs with different column spacings*

Case	Column Spacing (m)				1st Freq. (rad/s)		2nd Freq.(rad/s)		3rd Freq.(rad/s)		4th Freq. (rad/s)	
	l_1	l_2	l_3	l_4	Num.	Anal.	Num.	Anal.	Num.	Anal.	Num.	Anal.
1	1	0.5	1	-	2.37	2.33	3.76	3.77	-	-	-	-
2	1	1	1	-	2.09	2.11	3.48	3.52	-	-	-	-
3	1	2.5	1	-	1.67	1.65	3.27	3.30	-	-	-	-
4	1	5	1	-	1.27	1.27	3.20	3.21	-	-	-	-
5	0.5	0.5	1	-	2.46	2.47	3.41	3.46	3.88	3.87	-	-
6	1	2	3	-	1.53	1.55	2.57	2.62	3.19	3.20	-	-
7	0.9	0.9	0.9	0.9	1.13	1.15	2.02	2.10	2.32	2.31	2.38	2.38

Table 4.4 *TLMCDs parameters for study of different tuning ratios*

Parameters		4-column case	8-column case
Liquid height (m)	h	0.853	0.853
Mass ratio (%)	γ	1.0	1.0
Orifice head loss coefficient	η	1.5	0.4
Column spacing (m)	l_i	(5.118)	(2.193)
Cross-section area ratio	υ	(1.017)	(0.615)

(The values in parentheses are those used when kept constant)

Table 4.5 *TLMCDs parameters for study of different head loss coefficients*

Parameters		4-column case	8-column case
Total length (m)	l	17.059	17.059
Liquid height (m)	h	0.853	0.853
Mass ratio (%)	γ	1.0	1.0
Column spacing (m)	l_i	5.118	2.193
Cross-section area ratio	υ	1.017	0.615

Table 4.6 *TLMCDs parameters for study of different column numbers*

Parameters		Column number				
		2	4	6	8	12
Total length (m)	l	17.059	17.059	17.059	17.059	17.059
Liquid height (m)	h	0.853	0.853	0.853	0.853	0.853
Mass ratio (%)	γ	1.0	1.0	1.0	1.0	1.0
Orifice head loss coefficient	η	10.2	2.3	1.0	0.5	0.22
Vertical column size (m^2)	A	0.295	0.237	0.175	0.137	0.099
Cross-section area ratio	υ	1.152	1.017	0.772	0.615	0.432

Table 4.7 *Parameters for TLMCDs with different column number under equal vertical column size*

Parameters		Column number				
		2	4	6	8	12
Total length (m)	l	17.059	17.059	17.059	17.059	17.059
Liquid height (m)	h	0.853	0.853	0.853	0.853	0.853
Mass ratio (%)	γ	1.0	1.5	2.0	2.6	3.7
Orifice head loss coefficient	η	10.2	3.0	1.7	1.2	0.7
Vertical column size (m^2)	A	0.295	0.295	0.295	0.295	0.295
Cross-section area ratio	υ	1.152	1.019	0.786	0.631	0.452

Table 4.8 *Parameters for TLMCDs using the second vibration mode for structural mitigation*

Parameters		4-column case	8-column case
Total length (m)	l	17.059	17.059
Liquid height (m)	h	0.853	0.853
Mass ratio (%)	γ	1.0	1.0
Column spacing (m)	l_i	5.118	2.193
Uniform head loss coefficient	υ	1.017	0.615

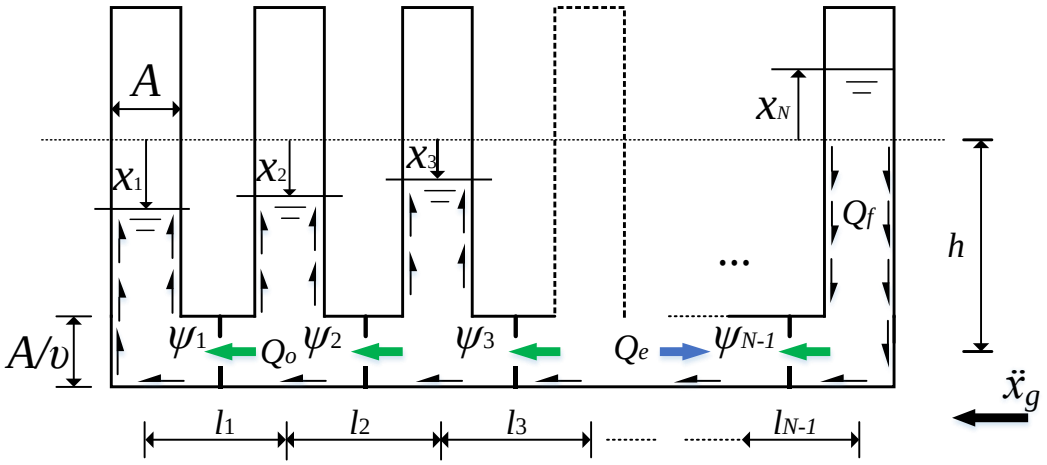

Figure 4.1 *Schematic of an N-column TLMCD*

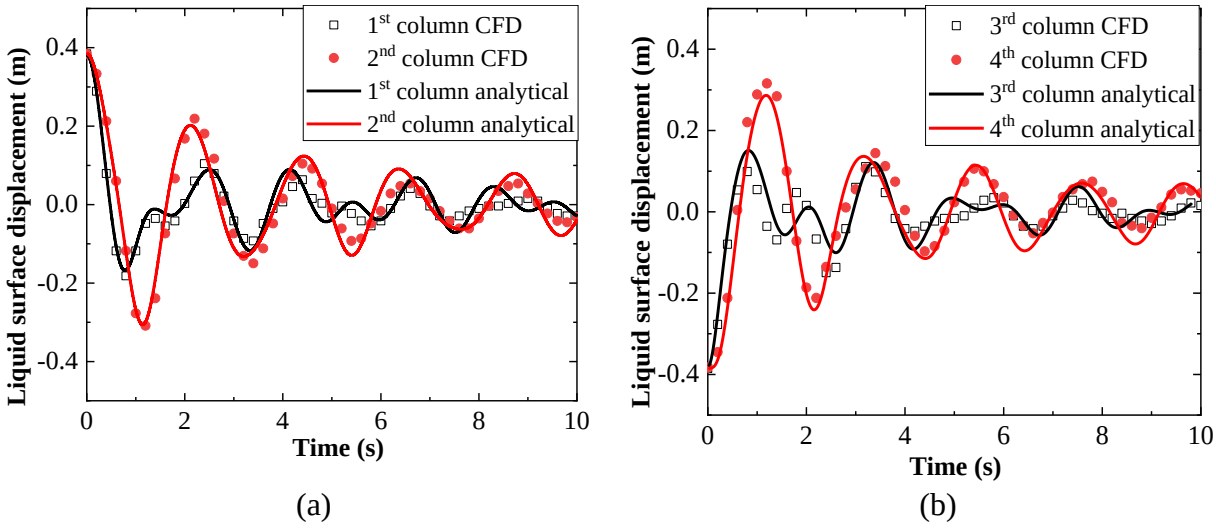

Figure 4.2 *Time series of column displacements under free oscillation. (a) columns x_1 and x_2; and (b) columns x_3 and x_4*

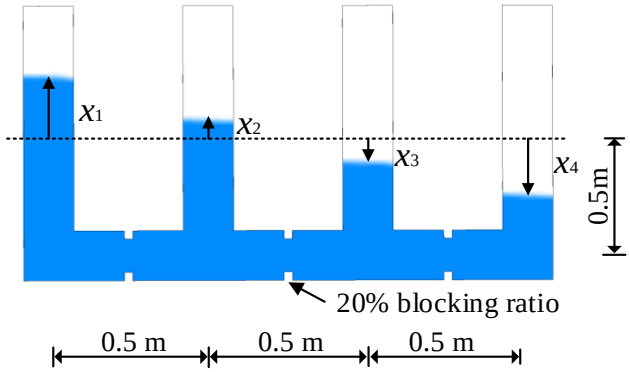

Figure 4.3 *CFD results of the 4-column TLMCD forced vibration, t = 7.8 s*

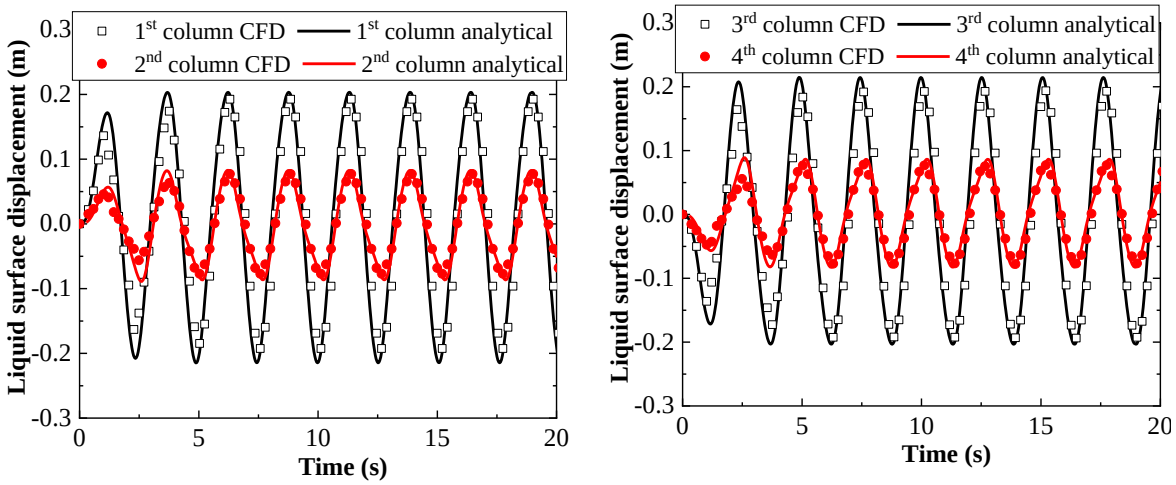

(a) (b)

Figure 4.4 *Time series of column displacements under forced oscillation. (a) columns x_1 and x_2; and (b) columns x_3 and x_4*

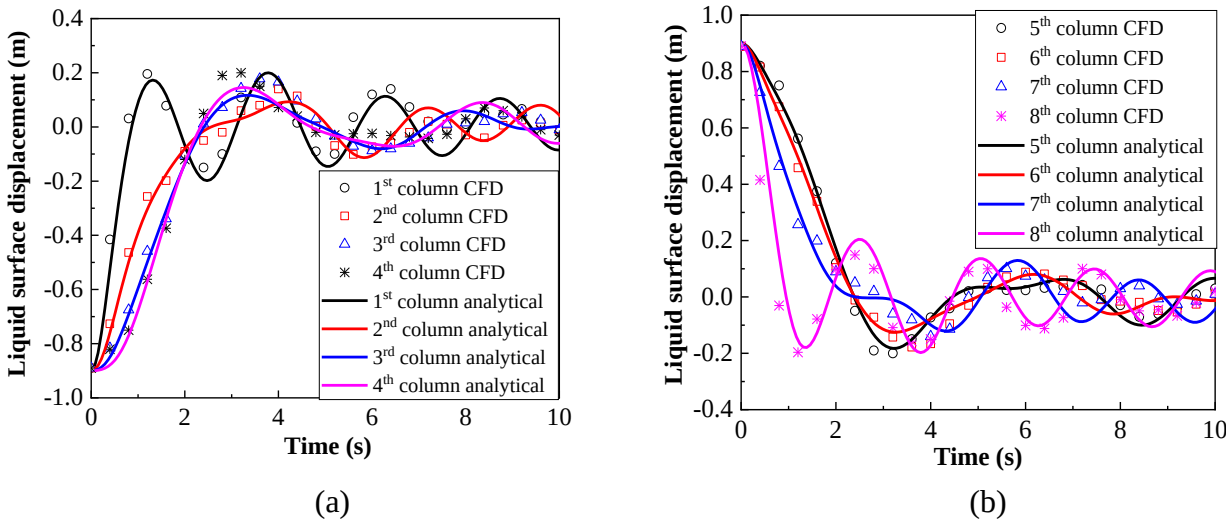

Figure 4.5 *Time series of the 4-column TLMCD free vibration*

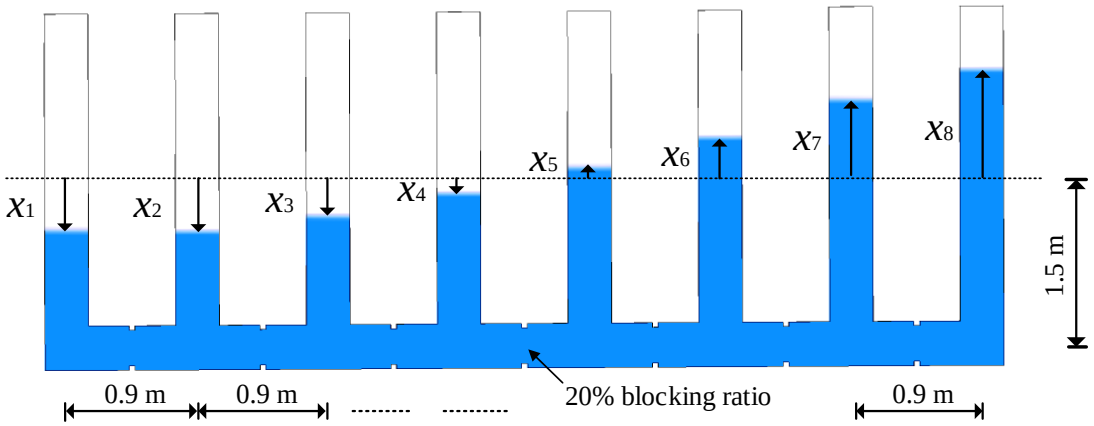

Figure 4.6 *CFD results of the 8-column TLMCD forced vibration, t =14.6 s*

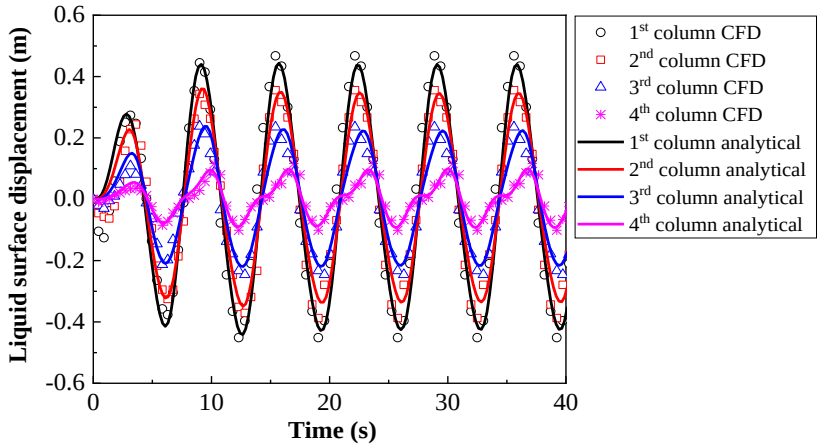

(a)

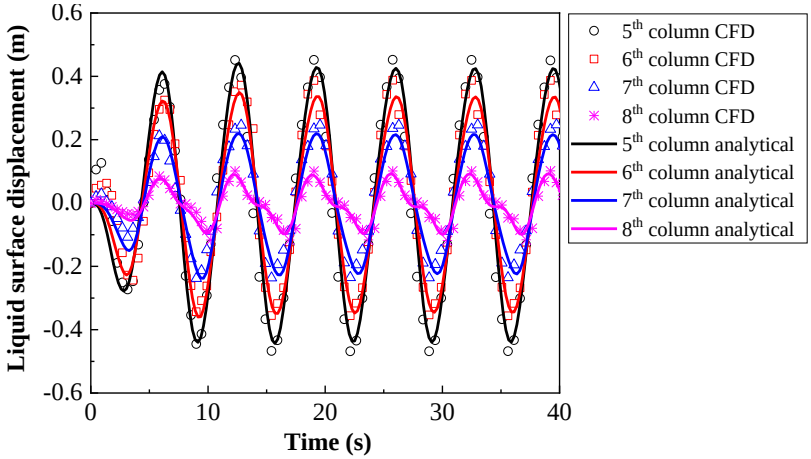

(b)

Figure 4.7 *Liquid displacements under harmonic acceleration: (a) columns x_1 to x_4; and (b) columns x_5 to x_8*

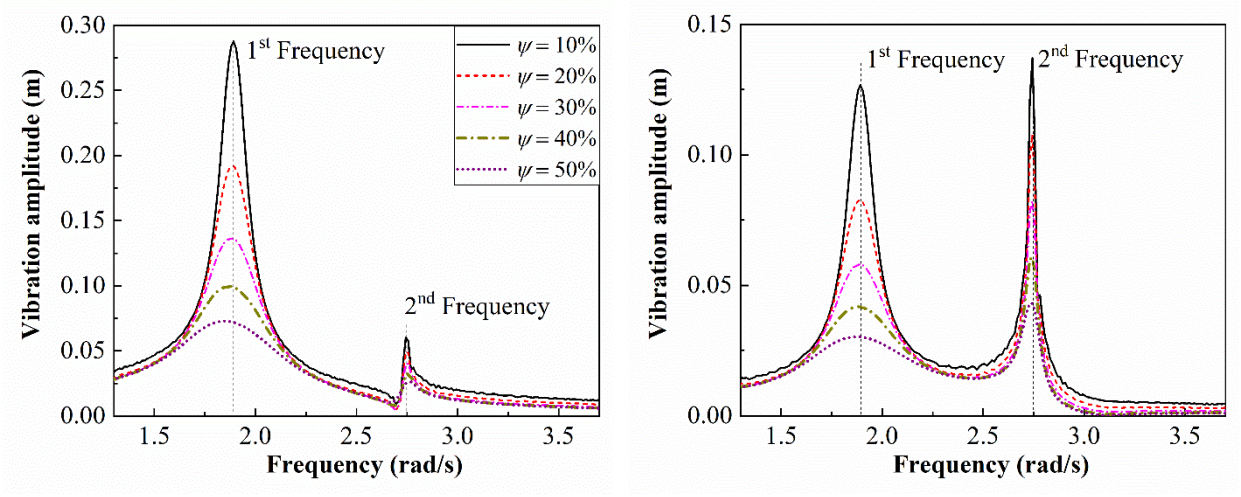

Figure 4.8 *Frequency responses of a 4-column TLMCD under various uniform orifice blocking ratios ($\ddot{x}_g$ = 0.1 m/s^2). (a) x_1 frequency response; (b) x_2 frequency response*

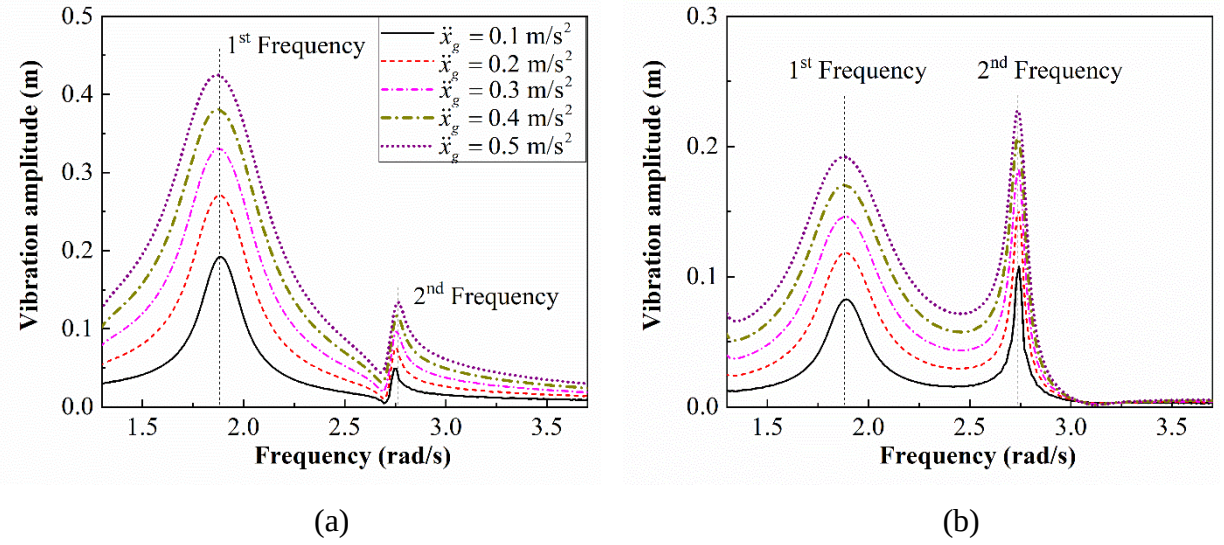

Figure 4.9 *Frequency responses of a 4-column TLMCD under various acceleration amplitudes (ψ = 20%). (a) x_1 frequency response; (b) x_2 frequency response*

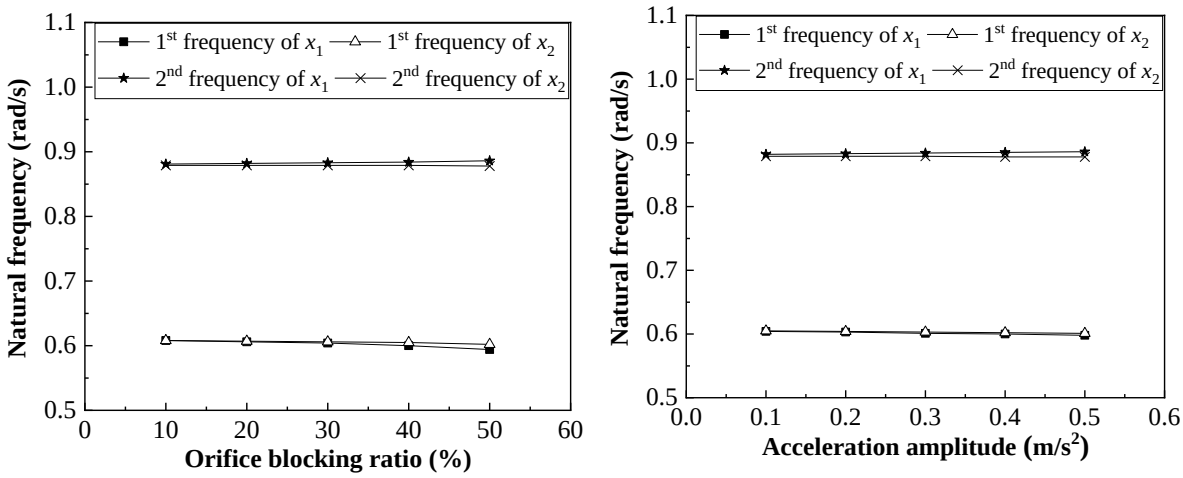

Figure 4.10 *The influence of orifice damping and floor acceleration amplitudes on the 4-column TLMCD's natural frequencies. (a) orifice blocking ratio; (b) acceleration amplitude*

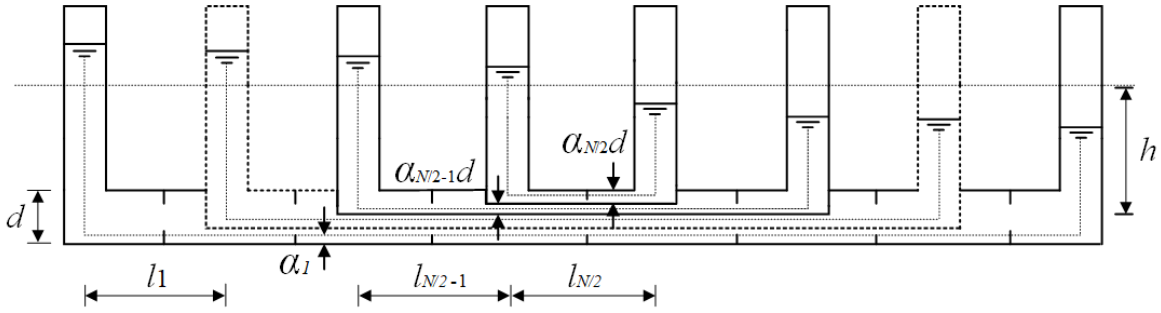

Figure 4.11 *Fundamental vibration mode for a symmetric TLMCD*

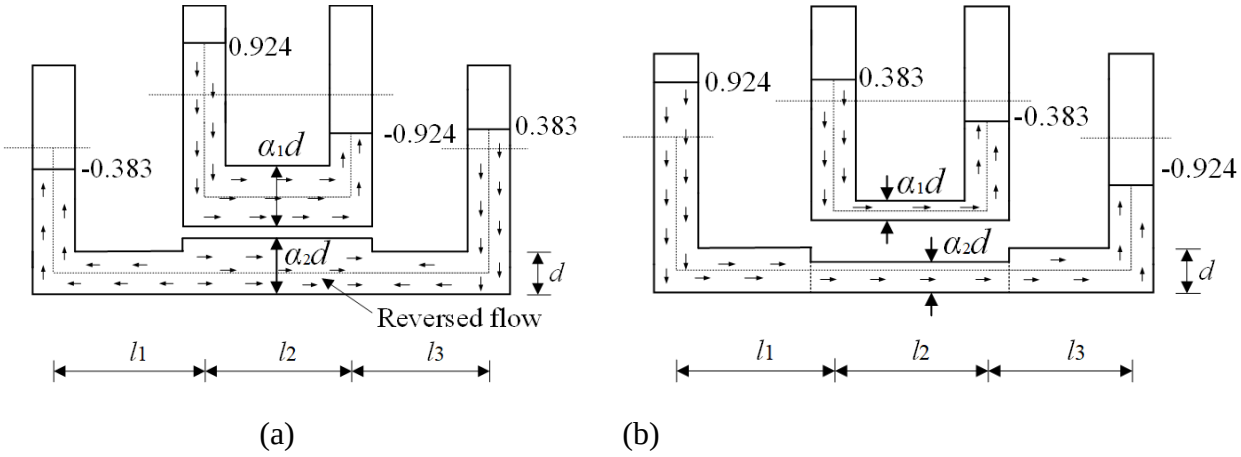

Figure 4.12 *The 4-column TLMCD's mode shapes: (a) the first mode shape; and (b) the second mode shape*

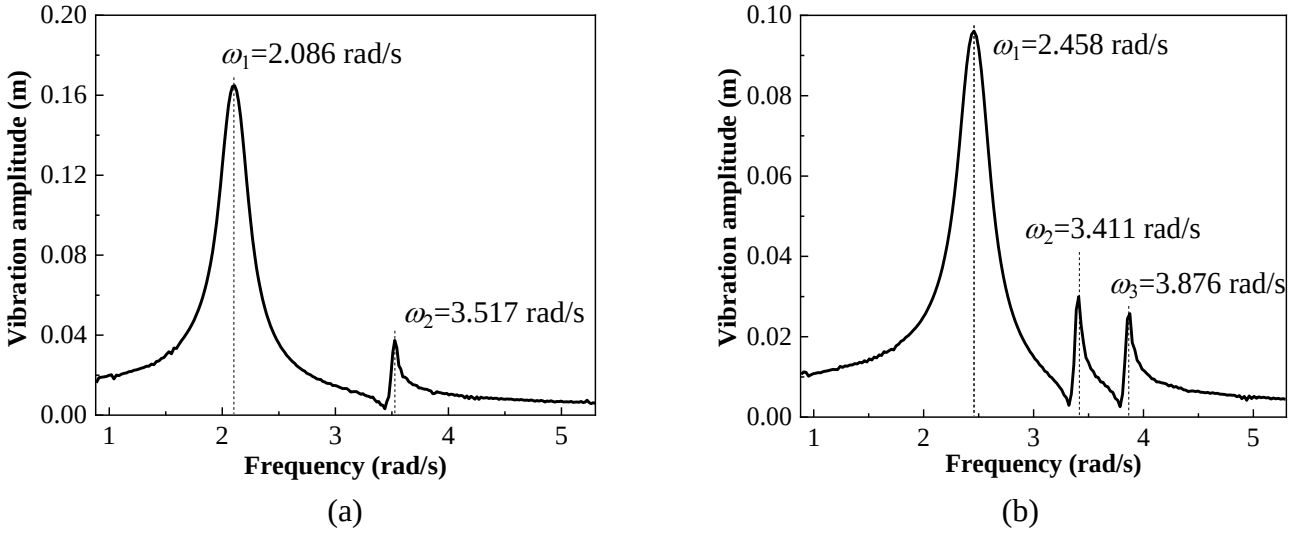

Figure 4.13 *Frequency response curves of x_1 for 4-column TLMCDs. (a) a symmetric case (case 2 in Table 4.3); and (b) an asymmetric case (case 5 in Table 4.3)*

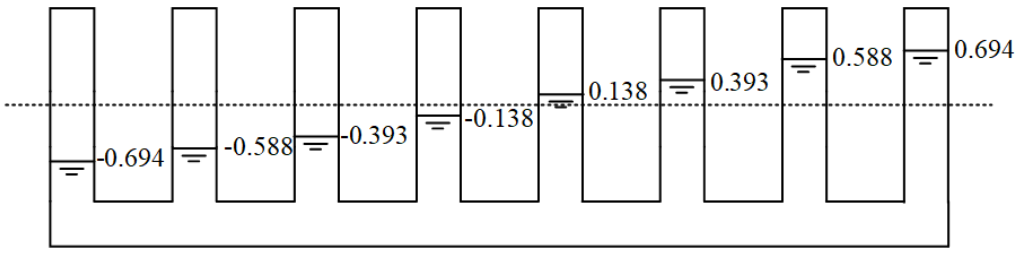

Figure 4.14 *The fundamental mode shape of the 8-column TLMCD*

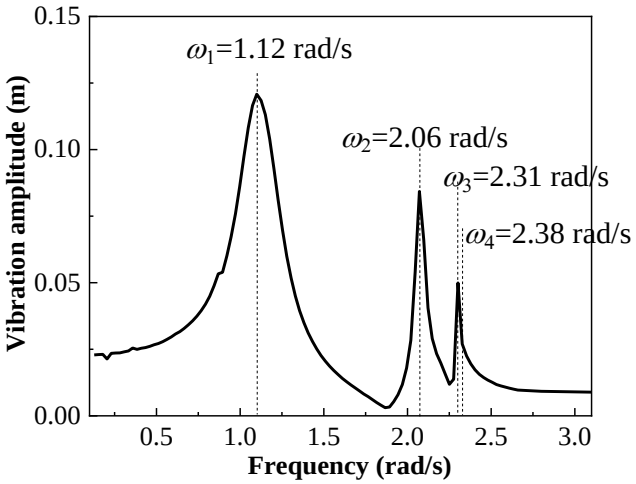

Figure 4.15 *The x_1 frequency response for the 8-column TLMCD ($\ddot{x}_g$ = 0.1 m/s^2, ψ = 20%)*

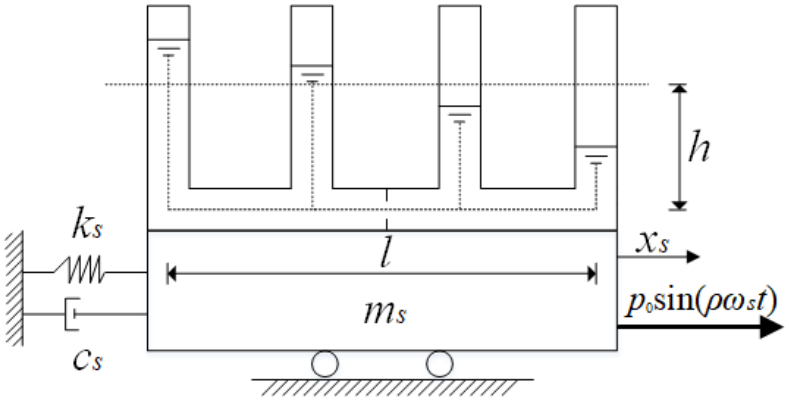

Figure 4.16 *SDOF system equipped with a TLMCD*

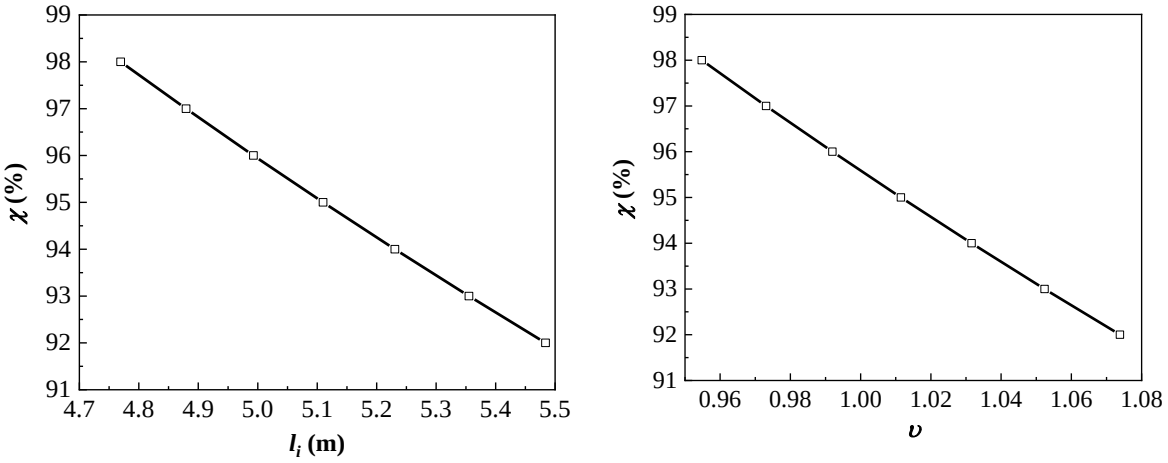

(a) (b)

Figure 4.17 *Effect of (a) column spacing l_i; and (b) cross-section area ratio υ on the tuning ratio*

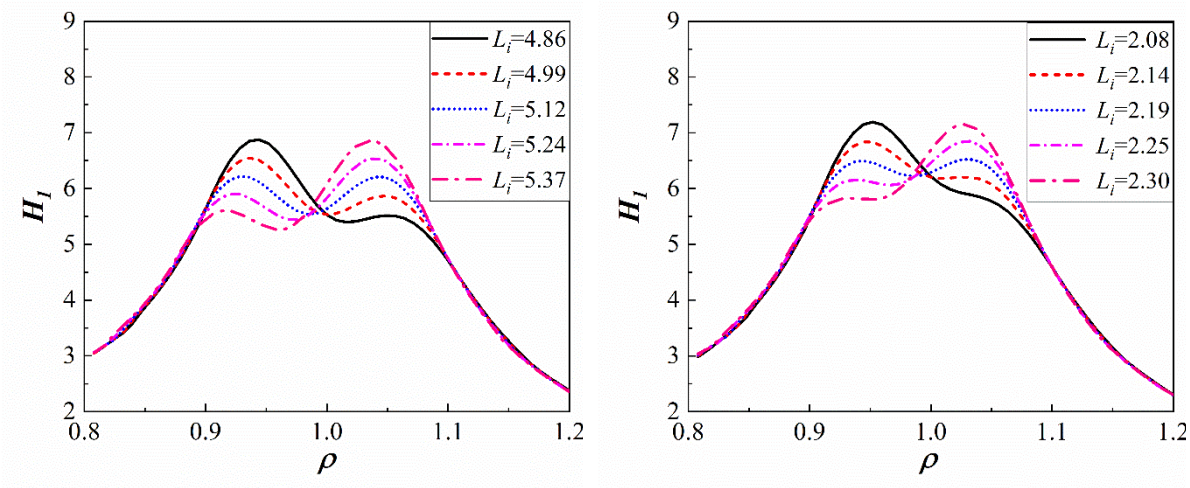

(a) (b)

Figure 4.18 *Effect of column spacing l_i for: (a) 4-column TLMCD; (b) 8-column TLMCD*

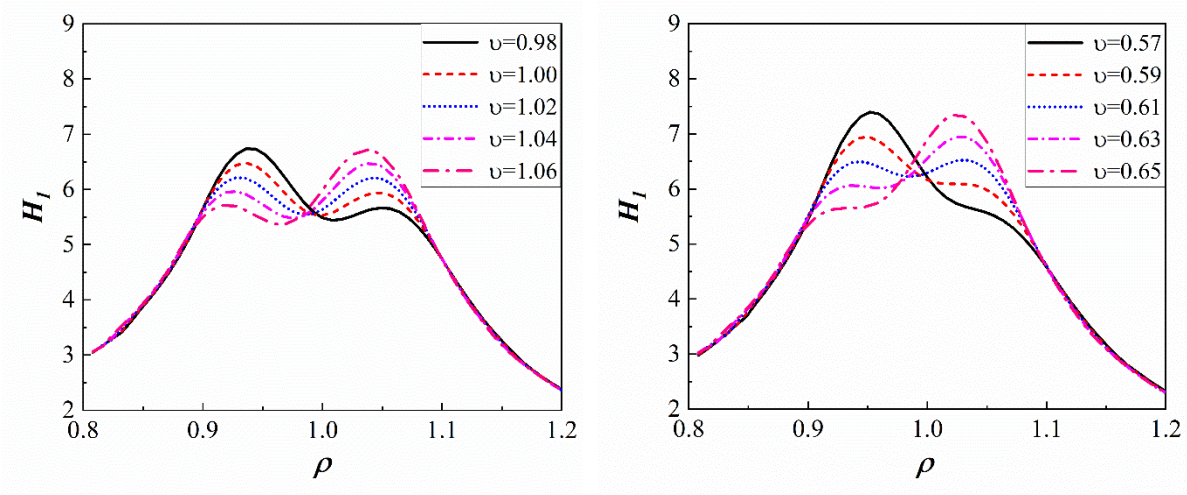

Figure 4.19 *Effect of cross-section area ratio υ for: (a) 4-column TLMCD; (b) 8-column TLMCD*

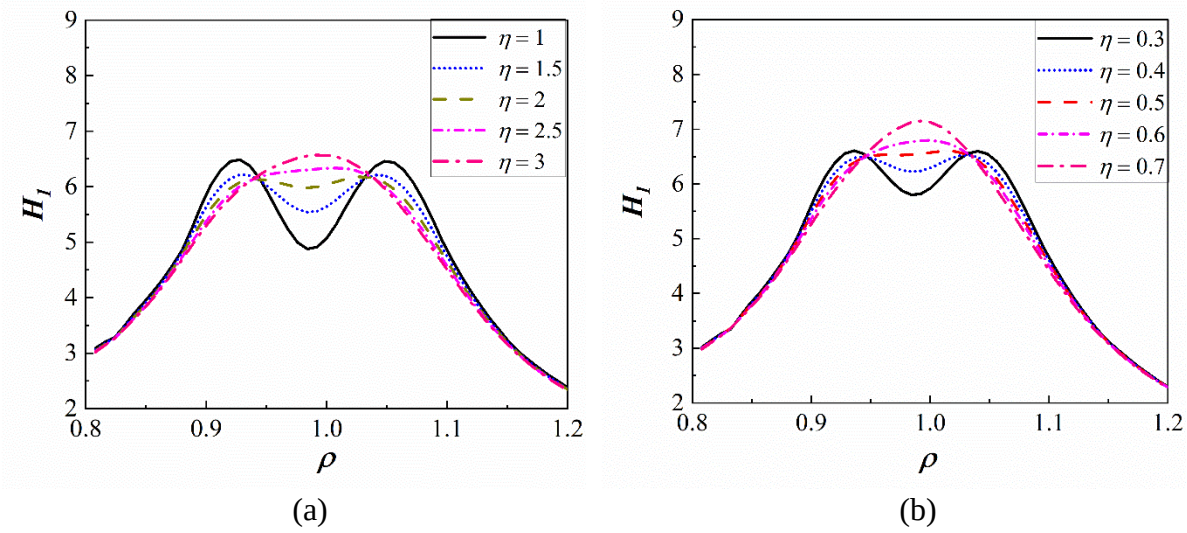

Figure 4.20 *Effect of orifice head loss coefficients η for: (a) 4-column TLMCD; (b) 8-column TLMCD*

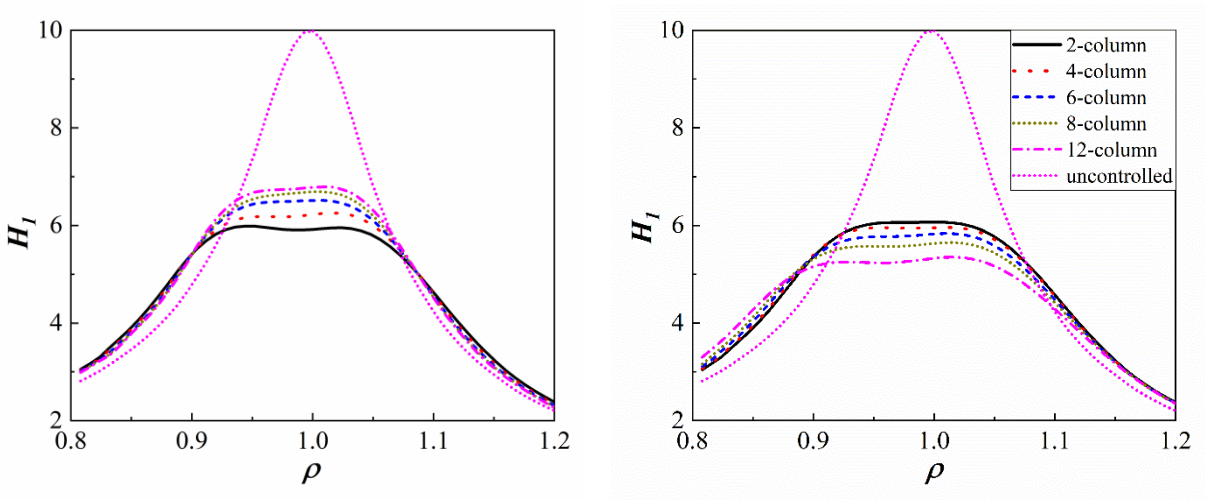

(a) (b)

Figure 4.21 *Comparison of the minimized transfer function curves under different column number N: (a) for equal mass; (b) for equal column size*

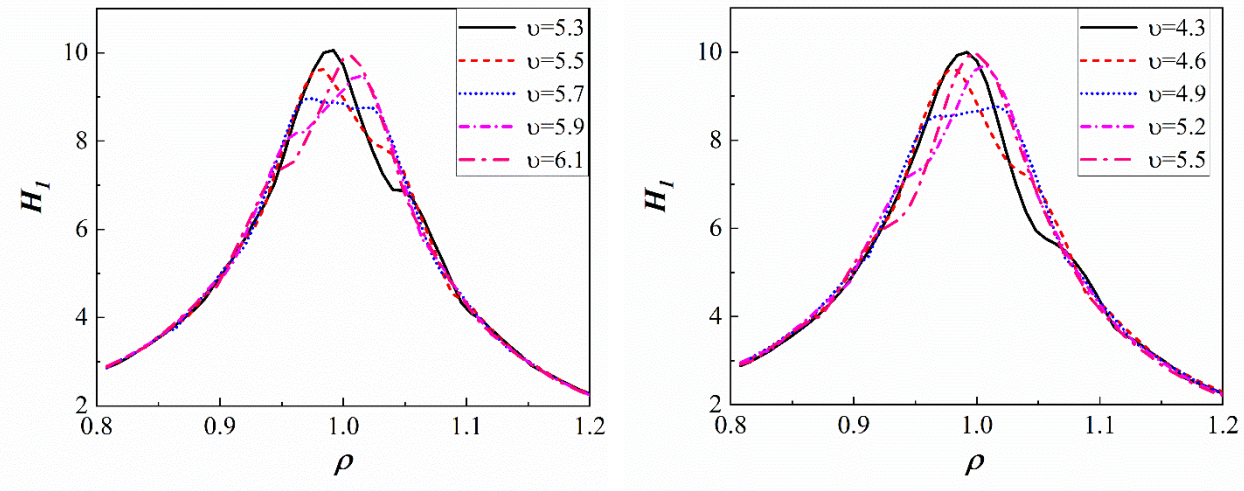

(a) (b)

Figure 4.22 *Transfer function curves using the second vibration mode for structural mitigation: (a) 4-column TLMCD; (b) 8-column TLMCD.*

CHAPTER 5. DYNAMIC TESTING OF A MULTIFUNCTIONAL PANEL WITH INTERNAL LIQUID DAMPING

A paper prepared to be submitted to *Journal of Structural Engineering*

Hao Wu, Simon Laflamme, An Chen

5.1 Abstract

In this study, we present a series of dynamic tests for a liquid-filled multifunctional reinforced concrete panel. The filled-in liquid can function as thermal exchanger that controls housing temperature as well as a damping device that dissipate vibration energy from wind or seismic hazard. The concrete panel has an internal structure of multiple vertical capillaries connected by a horizontal capillary at the lower part. The physical model of the liquid damping system is termed as tuned liquid multiple columns damper (TLMCD), which consists of multiple vertical tubes filled with oscillating liquid and generate liquid damping from liquid flow through orifices. In the dynamic tests, the reinforced concrete panel is connected to a fixed steel base by steel springs and has a one-directional motion guided by rails, making it a single-degree-of-freedom (SDOF) vibration system. The natural frequencies of the internal TLMCD are determined by the initial liquid height, and the optimal damping effect is achieved when the first natural frequency of the TLMCD is tuned to that of the SDOF structure at a frequency ratio of 98%. Free vibration tests with and without the internal TLMCD are performed to assess the increased damping due to the oscillating liquid. Test results indicate that the included liquid with 1.7% of the structure's total mass can cause the structure's equivalent damping ratio to increase by 9%.

Keywords: Tuned liquid column damper, dynamic loading, free vibration, shake table test

5.2 Introduction

Buildings nowadays are expected to not only be safe, but also environment-friendly, comfortable and even intelligent. Multifunctional structural components can meet the increasingly demanding requirements of modern structures (Hao et al. 2018; Sairajan et al. 2016). In this paper, we propose a reinforced concrete multifunctional panel that can resist lateral structural load as normal concrete panels, adjust room temperature, and protect the building from wind or seismic hazard. The concrete panel has an internal multi-capillary structure that can be filled with liquid. The multiple capillaries are connected at the bottom area of the panel to enable liquid flow freely though each capillary. Liquid exchange with outside sources can control room temperature, and liquid oscillation inside the panel can absorb vibration energy during severe wind or earthquake events. In this study, we focus on experimental testing on the vibration suppression capability of this concrete panel.

Previous studies often treat damping devices as individual structural components. Various types of dampers have been installed on the floors or roofs of buildings to provide additional damping. However, some hollow structural members can include liquid inside their internal space to enhance their damping performance. For instance, Ye et al. (2008) proposed a novel cast-in-situ hollow floor slabs that utilizes the high hollow volume in modern hollow floor slabs to fill water, making it an internal tuned liquid damper (TLD). The water sloshing effect can raise the damping ratio of the floor slabs by approximately 2%. Matia and Gat (2015) analyzed the solid-fluid interaction force in an elastic beam embedded with a fluid-filled parallel-channel network. Their findings indicate that the pressure and friction acting on the liquid will greatly reduce the elastic beam’s deformation caused by external dynamic forces. The above studies show that the interaction between structural components and liquid can contribute a significant amount of damping in structure control.

Tuned liquid multiple columns dampers (TLMCD) (Wu et al. 2019, Coudurier et al. 2018) are extensions of a classical tuned liquid column dampers (TLCD), which is a liquid-filled U-shapes tube and a single-degree-of-freedom (SDOF) system (Sakai et al. 1989, Di Matteo et al. 2015). Compared to conventional TLCDs, TLMCDs has multiple capillaries (columns) and is more suited to place in structural panels since they can efficiently occupy the narrow vertical space by including more columns than TLCDs. Also, a TLMCD is multiple-degree-of-freedom (MDOF) structures and has multiple natural frequencies, which could help suppress more than one vibration modes of the main structure.

There are many existing dynamic tests method to identify a structure's inherent damping. For example, free vibration method is a commonly used technique to identify the damping of structures by measuring the amplitude decay ratio (Botelho et al. 2005). The analytical solutions are also easy to obtain once the type of the structure's damping is specified (Chopra et al. 2016). Besides free vibration tests, shake table tests with various excitations such as frequency sweep, white noise type, seismic ground motions, etc., are also good techniques to evaluate a structure' damping performance (Symans et al. 1997; White and Pinnington 1982).

The paper mainly focusses on experimental study of the proposed reinforced concrete multifunctional panel. The included multiple-capillary liquid damping system, which can be described as a TLMCD, enhances the primary system's damping. As a result, we conduct free vibration tests to access the increased damping effect due to the internal liquid motion. The equivalent damping ratio of the concrete panel can be indirectly obtained from its displacement curve. The remaining paper is organized as the following: Section 5.3 describes the shake table test setup including the reinforced concrete panel configuration and how to

measure the natural frequencies of the internal TLMCD. Section 5.4 analyzes several free vibrations tests of the internal TLMCD and the concrete panel with and without liquid damping. Section 5.4 discusses the calculation of the expected damping forces using a nonlinear analytical model and numerical simulation of the test results. The final section concludes the paper.

5.3 Test Setup

The dynamic tests are conducted in the Structural Lab of Iowa State University. The geometry dimension of the RC multifunctional panel is 152 cm x 61 cm x 10 cm and has an internal hollow multi-capillary plastic tubes imbedded, as shown in Figure 5.1. Two layers of No.2 rebars are embedded in the concrete panel to provide bending and axial stiffness, as shown in Fig. The vertical and the horizontal reinforcement ratios of the RC panel are 0.41% and 0.25%, respectively, which is larger than the minimum reinforcement ratio required in ACI-318 code (2014).

Liquid is filled inside the RC panel during the test procedure to provide internal liquid damping. Specially manufactured plastic hollow tubes are embedded in the RC panel before casting concrete to create the required geometry space for the filled-in liquid. The plastic tubes consist of six vertical circular tubes with an inner diameter of 5.08 cm, and one horizontal square tube with a 10.16 cm × 5.08 cm (height × width) inner dimension. The filled-in water can flow from any vertical tube to another one through the horizontal tube. Orifices of 15% blocking ratio are installed in the middle of each spacing between the vertical columns. Water flow through the orifices will result in a viscous damping force that is proportional to the square of its liquid velocity, which is the main source of damping in the RC panel.

The RC panel is placed on the top of a cart with rigid steel casters, which are guided by the rails on a base plate, as illustrated in Figure 5.3. The RC panel and the large steel channel that it sits in are connected by four identical steel springs with a stiffness of 2.259 kN/m. The panel, cart and spring constitute a SDOF system with the following structural parameters: m_s = 302.55 kg, and k_s = 9.036 kN/m. To measure the structure's displacements and accelerations, two LVDTs and two accelerometers are installed at the two flanges of the T-sectioned panel. The sampling rate of sensors is 2000 Hz. During the test, the difference between the two LVDTs are found to be less than 1%, which indicates that there is no lateral motion or rotation for the RC panel and that the displacement in the panel-spring system is one-dimensional.

5.4 Free Vibration Tests

Three free vibration tests are conducted to investigate the internal damping system in the concrete panel.

5.4.1 Free vibration of liquid in the multi-capillary tube

The first one is the free vibration test of the internal plastic tube filled with water, as is shown in Figure 5.2 c. This test is conducted before the plastic tube is embedded in the concrete panel. The liquid surface displacement of the 1st column is illustrated in Figure 5.4 and correlates very well to an analytical solution, which will be introduced later in Section 5.5. Free vibration analysis shows that when the liquid height varies from 15.2 cm to 25.4 cm, the range of the natural frequency of the internal liquid damper is 0.83-0.89 Hz. Typically, the filled-in liquid is water due to its low cost, and the internal liquid weight corresponding to a liquid height of 20 cm is 5.36 kg, which is approximately 1.7 % of the total mass of the concrete panel.

5.4.2 Free vibration of the main structure

The main structure consists of a wheeled cart connected to a fixed base by steel springs and can move in a horizontal direction guided by rails in the fixed base. The cart-spring-rail system is to simulate a SDOF system, where the horizontal displacement of the cart is the single DOF. The main damping source of the structural system is the rotational friction force between the cart's wheels and its rails, which can be modeled as a constant coulomb friction force with the direction contrary to that of the SDOF structure's velocity. The dynamic equations of motion for the SDOF structure is expressed as:

$$m_s\ddot{x} + k_s x + \mu m_s \mathrm{g}\,\mathrm{sign}\left(\dot{x}\right) = 0 \tag{5-1}$$

where x denotes the structural displacement, μ is the constant rotational friction coefficient, g is the gravitational acceleration and $\mathrm{sign}\left(\dot{x}\right)$ is the sign of the structural velocity. The coulomb frictional coefficient extracted from a static test is 0.018. If the coulomb friction damping is converted into a linearly proportional damping based on the amplitude of the first two cycles of the free vibration test, the equivalent damping ratio is ξ_s = 1.51 %. The analytical solution of Eq. (5-1) and the actual free vibration displacement are illustrated in Figure 5.5. From the results, the coulomb friction damping model is quite accurate to describe the main structure's motion. The damped structure natural frequency is 0.87 Hz.

5.4.3 Free vibration of the main structure with liquid damping

The third free vibration test is to evaluate the enhanced damping effect provided by the internal liquid system. The test is conducted after the multi-capillary plastic tube is embedded in the concrete panel. The enhanced liquid damping of the internal TLMCD is indirectly measured by comparing the displacement decaying rate of free vibration tests between the cases when the concrete panel is filled with water and when it is not. Various

liquid heights are applied, with the maximum damping happens when the water height is 20.3 cm. At this height, the natural frequency of the internal damper is approximately 98% of that the primary SDOF structure. The displacement curves of the SDOF structure with/without the 20.3 cm internal liquid is shown in Figure 5.6. From the comparison, we find that the displacement of the first cycle decease by 5.7% compared to the free vibration test without the filled liquid. The RC panel's equivalent damping ratio increases from 1.51% to 1.64% due to included oscillating liquid.

5.5 Mitigation of Structure Motion with TLMCD

The schematic drawing of the internal TLMCD is illustrated in Figure 5.7, where $\ddot{x}_g$ is the acceleration transmitted from the primary structure, x_i is the liquid surface displacement in the i^{th} column, h is the uniform initial vertical liquid surface height in each column, l_i is the horizontal centre-to-centre distance between the i^{th} and $i+1^{\text{th}}$ columns, ψ_i is blocking ratio of the i^{th} orifice, A is the vertical column's cross-section area, and υ is the vertical/horizontal cross-section area ratio. The TLMCD is modeled as an NDOF system for DOFs x_i.

The dynamic model of the above system under free vibration can be derived using Lagrange equations and the final equations of motion are expressed as the following (Wu et al. 2019):

$$\begin{aligned}&\sum_{j=1}^{i}\left(\sum_{k=1}^{N-1}x_k-h-\sum_{k=i}^{N-1}\upsilon l_k\right)\ddot{x}_j+\sum_{j=i+1}^{N-1}\left(\sum_{k=1}^{N-1}x_k-h-\sum_{k=j}^{N-1}\upsilon l_k\right)\ddot{x}_j-\left(h+x_i\right)\ddot{x}_i+\frac{1}{2}\left(\sum_{k=1}^{N-1}\dot{x}_k\right)^2-\frac{1}{2}\dot{x}_i^2\\&-\mathrm{g}x_i-\mathrm{g}\sum_{k=1}^{N-1}x_k=\mu\left|\dot{x}_i\right|\dot{x}_i\left(h+x_i\right)+\mu\left|\sum_{k=1}^{N-1}\dot{x}_k\right|\left(\sum_{k=1}^{N-1}\dot{x}_k\right)\left(h-\sum_{k=1}^{N-1}x_k\right)+\sum_{k=i}^{N-1}\upsilon\left(\mu l_k+\frac{1}{2}\eta_k\right)\left|\sum_{j=1}^{k}\dot{x}_j\right|\sum_{j=1}^{k}\dot{x}_j\\&+\ddot{x}_g\left(t\right)\sum_{k=i}^{N-1}l_k,\ \left(i=1,2,...,5\right)\end{aligned}\tag{5-2}$$

$$m_s\ddot{x}_s+\rho A\left(Nh+\sum_{i=1}^{N-1}l_i/\upsilon\right)\ddot{x}_s+\rho A\sum_{i=1}^{N-1}\left(\ddot{x}_i\sum_{j=1}^{i}l_j\right)+\mu m_s g\ \mathrm{sign}\left(\dot{x}_s\right)+k_s x_s=0\tag{5-3}$$

where ρ is the liquid density, g is gravitational acceleration, and μ is the frictional head loss coefficient caused by the friction between the inner surface of the internal tube and liquid.

The relationship between the blocking ratio and the head loss coefficient is given by (Idelchik and Fried 1986):

$$\eta = \left(\psi + 0.707\psi^{0.375}\right)^2 \left(1-\psi\right)^{-2} \tag{5-4}$$

In the test, the orifices in the concrete panel have an identical blocking ratio of 15%, which corresponds to a head loss coefficient of 0.342 by Eq. (5-4). The inner surface of the plastic tube is smooth, and the friction head loss coefficient is set as a small number of 0.02.

To solve the equations, an initial structure displacement/velocity and the external excitation force is needed. Runge-Kutta method with a recommended time step of 10^{-3} of the liquid free vibration period can be used to compute the numerical solutions.

Using the above equations, the free vibration motion of the SDOF concrete panel system equipped with an internal TLMCD can be solved numerically. The comparison of the numerical solutions and experimental results of the concrete panel's displacements is shown in Figure 5.8, showing that the test result and the analytical result are very similar. The equivalent damping ratio increased from 1.51% to 1.62 % when the liquid damping is considered in the analytical model. The analytical damping increase is slightly less than that in the test, and this is potentially caused by the fact that there is other minor liquid damping not considered in the analytical model.

5.6 Conclusions

A reinforced concrete multifunctional panel with an internal multi-capillary tube system is manufactured. When liquid is filled in the internal multi-capillary tube, it can function as thermal exchanger and a TLMCD. The damping mechanism of TLMCD is

illustrated by a nonlinear model that takes the orifice head loss as the main source of damping. Free vibration tests of both the multi-capillary tube and the SDOF concrete panel are conducted. The first free vibration test can identify the natural frequency and damping of the internal TLMCD system, which validates the analytical TLMCD model. The second free vibration test is the SDOF concrete panel system that evaluates the enhanced damping effect due to the internal TLMCD. When the concrete panel is filled with liquid of a 20.8 cm height, which equals to 1.7% of the concrete panel's total mass, the equivalent damping ratio of the panel will increase by 9%, from 1.51% to 1.64%.

Further tests should include shake table tests where the SDOF structure is excited by accelerations of around the internal TLMCD's natural frequency, in which case larger liquid motion and liquid damping can be expected due to the resonance of water motion.

5.7 References

ACI Committee. (2014). Building code requirements for structural concrete:(ACI 318-14); and commentary (ACI 318-14). *American Concrete Institute*.

Botelho, E. C., Campos, A. N., De Barros, E., Pardini, L. C., and Rezende, M. C. (2005). "Damping behavior of continuous fiber/metal composite materials by the free vibration method." *Composites Part B: Engineering*, 37(2–3), 255–263.

Chopra, A. K. (2016). Dynamics of Structures: Theory and Applications to Earthquake Engineering. 5th ed. Pearson.

Coudurier, C., Lepreux, O., and Petit, N. (2018). "Modelling of a tuned liquid multi-column damper. Application to floating wind turbine for improved robustness against wave incidence." *Ocean Engineering*, Elsevier Ltd, 165(March), 277–292.

Di Matteo, A., Lo Iacono, F., Navarra, G., and Pirrotta, A. (2015). "Innovative modeling of Tuned Liquid Column Damper motion." *Communications in Nonlinear Science and Numerical Simulation*, Elsevier B.V., 23(1–3), 229–244.

Hao, D., Zhang, L., Yu, J., and Mao, D. (2018). "Mechanical properties of multifunctional structure with viscoelastic components based on FVE model." *Acta Astronautica*, Elsevier Ltd, 143(October 2017), 255–262.

Idelchik I. E., Fried, E. (1986). Handbook of hydraulic resistance, 2nd ed, Hemisphere Publishing Corp., Washington DC.

Matia, Y., and Gat, A. D. (2015). "Dynamics of Elastic Beams with Embedded Fluid-Filled Parallel-Channel Networks." *Soft Robotics*, 2(1), 42–47.

Sairajan, K. K., Aglietti, G. S., and Mani, K. M. (2016). "A review of multifunctional structure technology for aerospace applications." *Acta Astronautica*, Elsevier, 120, 30–42.

Sakai, F., Takaeda, S., Tamaki, T., (1989) "Tuned liquid column damper-new type device for suppression of building vibrations." *International Conference on Highrise Buildings*, 25-27.

Symans, M. D., Constantinou, M. C. (1997). "Seismic testing of a building structure with a semi-active fluid damper control system." *Earthquake Engineering and Structural Dynamics*, 26(7), 759-777.

White, R. G., Pinnington, R. J. (1982). "Practical application of the rapid frequency sweep technique for structural frequency response measurement." *The Aeronautical Journal*, 86(855), 179-199.

Wu H., Laflamme S., Chen A., (2019) "A nonlinear dynamic model for tuned liquid multiple columns damper," *Journal of Sound and Vibration*

Ye, L., Lu, X., Qu, Z., and Hou, J. (2008). "Distributed TLDs in RC floors and their vibration reduction efficiency." *Earthquake Engineering and Engineering Vibration*, 7(1), 107–112.

(a) (b)

Figure 5.1 *The RC multifunctional panel (a) dimensions (b) the internal plastic tubes and the reinforcement layer*

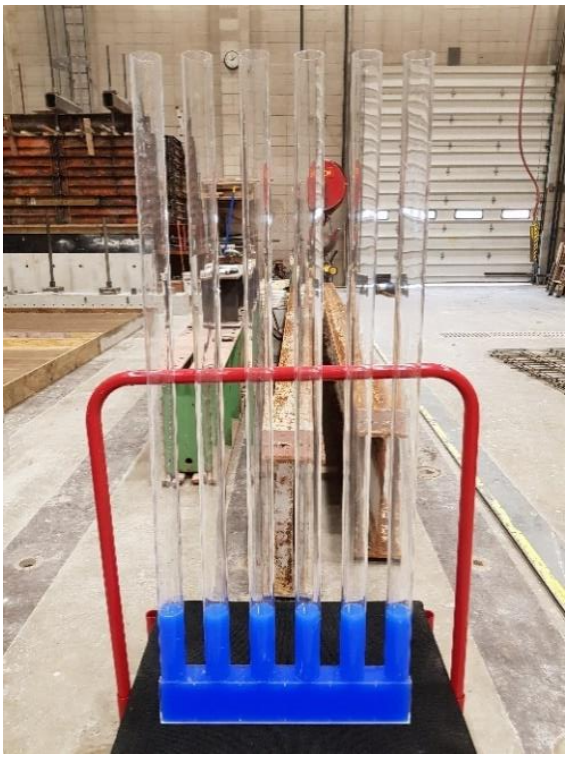

(a)

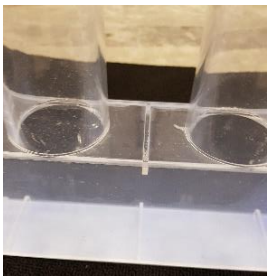

(b)

(c)

Figure 5.2 *The internal plastic tubes of the RC multifunctional panel (a) the whole configuration; (b) the orifices in the horizontal tube; (c) the first vibration mode of filled in water*

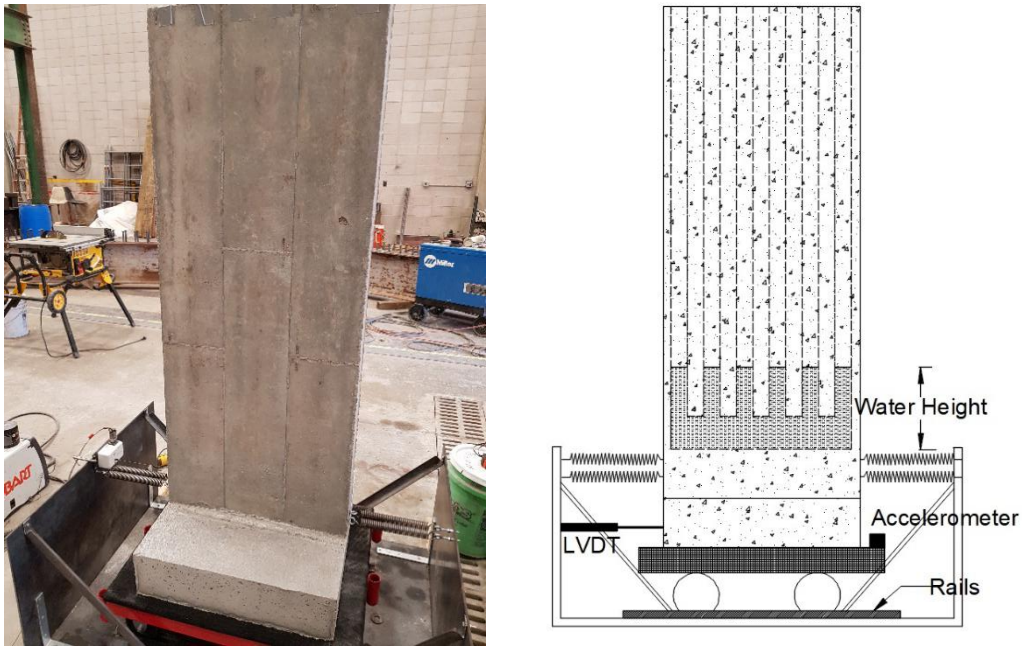

(a) (b)

Figure 5.3 *The RC multifunctional panel SDOF system (a) test setup (b) schematic drawing of the sensors and their locations*

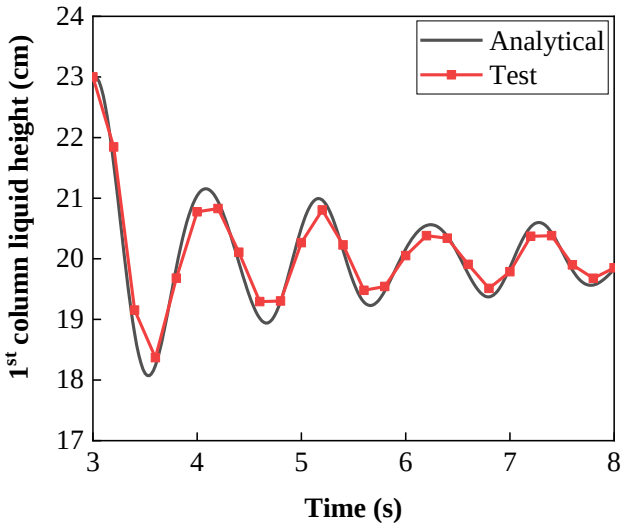

Figure 5.4 *The 1st tube liquid surface motion of the internal TLMCD*

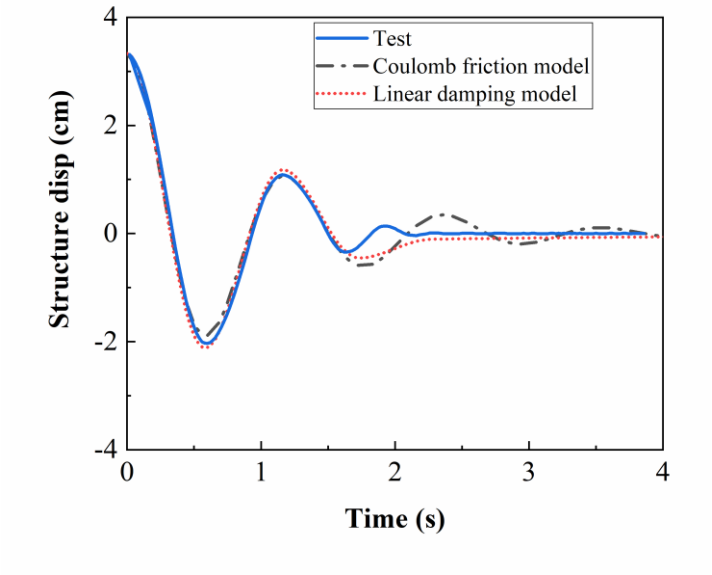

Figure 5.5 *The time series of RC panel SDOF structure free vibration displacement*

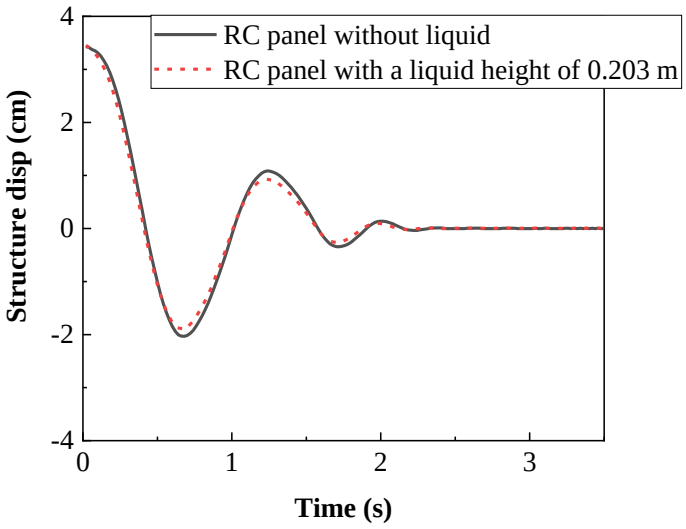

Figure 5.6 *The time series of RC panel SDOF structure free vibration displacement with liquid damping*

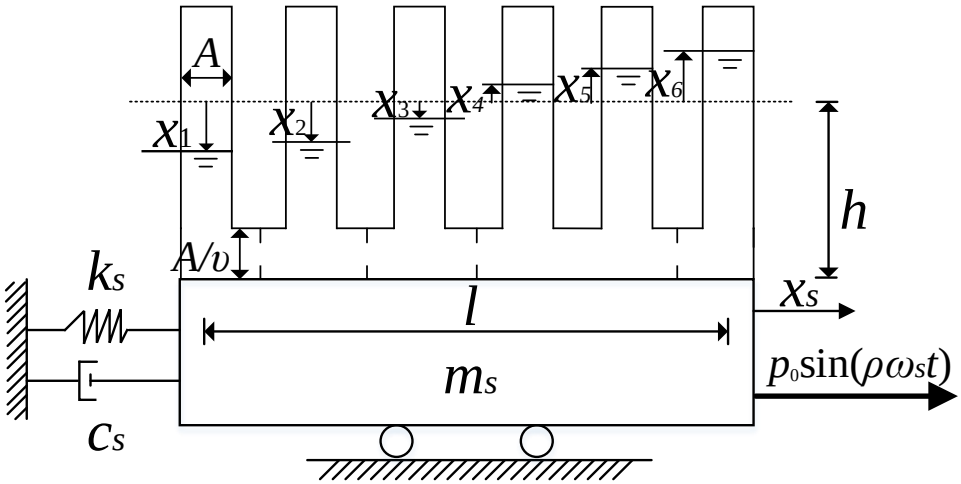

Figure 5.7 *Schematic drawing of a TLMCD on a SDOF structure*

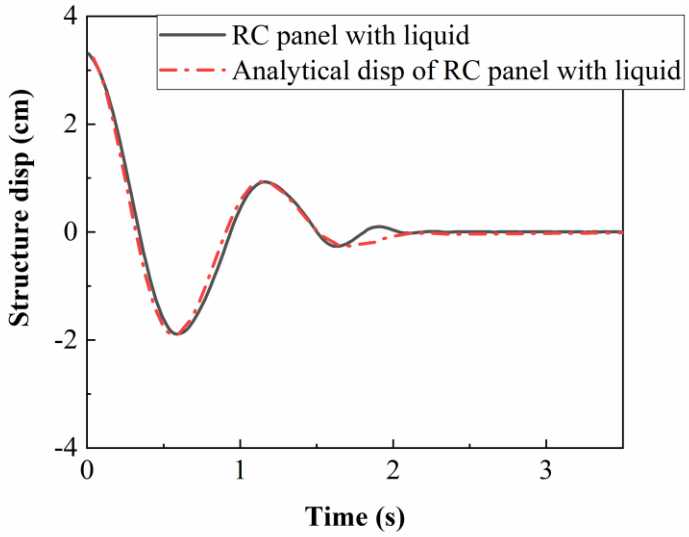

Figure 5.8 *Comparisons of numerical and test results for the concrete panel displacements with liquid damping.*

CHAPTER 6. OPTIMIZATION OF TUNED LIQUID MULTIPLE COLUMNS DAMPER FOR SUPPRESSING STRUCTURAL VIBRATION

A paper to be submitted to *Journal of Sound and Vibration*

Hao Wu, Simon Laflamme and An Chen

6.1 Abstract

This study focuses on the characteristics of tuned liquid multiple columns dampers (TLMCDs) in mitigating primary structures' vibration under harmonic or random external forces. A TLMCD consists of multiple vertical tubes connected via a horizontal one, and it can dissipate vibration energy by filled-in liquid oscillating through orifices in the horizontal tube. A TLMCD has multiple vibration modes, contrasting with a conventional tuned liquid column damper (TLCD), which is U-shaped and a single-degree-of-freedom (SDOF) system. Analytical models depict TLMCDs as weakly nonlinear systems that can be linearized under random and harmonic excitations. The damping and stiffness of TLMCDs can be controlled by the orifices and column spacings between the vertical columns, respectively. In this paper, we optimize the damping and geometry of TLMCDs using a genetic algorithm when they are attached to various primary structures. All the parameters are optimized simultaneously under a fixed horizontal/vertical length ratio. Results show that with proper chosen orifice damping and geometry configuration, a TLMCD can better mitigate a multi-degree-of-freedom (MDOF) primary structure than single TLCD or multiple TLCDs with the same mass.

Keywords: Tuned liquid multiple column damper, structure control, damping system, optimization, MDOF dampers

6.2 Introduction

Supplemental damping systems have gained popularity to improve structural motion performance. In particular, passive energy dissipation systems are now widely accepted and deployed in the field (Symans et al. 2008 [1]). Of interest to this paper are tuned mass dampers (TMDs), which leverages inertial forces to reduce vibrations over a typical bandwidth of $\pm$ 15% of their tuned frequency (Connor and Laflamme 2014 [2]). TMD systems have been widely studied and applied for a diverse range of structures including tall buildings (Lu et al. 2017 [3]), bridges (Debnath et al. 2016 [4]) and wind turbines (Stewart and Lackner 2014 [5]). An extension of TMDs are the tuned liquid column dampers (TLCDs) that, instead of a moving mass, leverage a liquid oscillating in a U-shaped tube. TLCD can be advantageous over TMDs by being easier to implement, less costly to maintain, and useful for water storage (Di Matteo et al.2015 [6]). More recently, variations of TLCDs with multiple columns, termed as tuned liquid multiple column damper (TLMCD) were proposed to address various limitations of classical TLCDs. For instance, a retuning multi-celled TLCD that allows cells blocked/opened after TLCD installation improve the tuning accuracy (Min et al. 2016 [7]); a four column bidirectional TLCD can better mitigate structural vibrations coming in orthodoxy directions (Rozas et al. 2015 [8]); a star-shaped or a triangle-shaped TLCD increases the robustness against wave incidence for floating wind turbine (Coudurier et al. 2018 [9]). TLMCDs offer the promise of enhanced design flexibility through the variation of additional geometries, enabling more compact configurations or higher control reachability (Wu et al. 2018 [10]).

In prior work, the authors have presented an analytical model for a TLMCDs (Wu et al. 2018 [10]). The objective was to develop a mathematically trackable method that could be used in the study of TLMCD systems of arbitrary configurations. Here, work is extended to

enable design optimization. A critical challenge in design optimization of TLMCDs is in the high nonlinearity of the device. Similar challenges have been addressed in work on TMDs. While theory for design and optimization TMD systems is well established (Connor and Laflamme 2014 [2]), it is yet an active area of research for inertia systems of various principles and complexity. Traditional approaches include the minimization of the maximum response (H_∞ norm) (Cheung et al. 2011 [11], Chun et al. 2015 [12]), and the overall energy dissipation (H2 norm) (Tang et al. 2016 [13], Sun et al. 2017 [14]) for various TMD configurations. Venanzi 2015 [15] evaluated the effect of probability distributions in design parameters on damping performance. Lin et al. 2017 [16] studied design based on mitigation performance robustness over the frequency spectrum leveraging multiple single degree-of-freedom TMDs. Ubertini 2017 et al. [17] investigated reliability-based optimization of TMDs with the multi-objective of optimizing robustness against frequency mistuning while minimizing probability of failure. Greco et al. 2016 [18] also conducted multi-objective TMD optimization but considering economic and mitigation performance criteria.

Work discussed above focused on SDOF or multiple SDOF TMDs, while TLMCDs are inherently MDOF configurations. Gradient-based methods, such as those based on the H∞ and H2 norms, have been employed to optimize a 2DOF TMD (Zuo and Nayfeh 2006 [19]). However, the higher dimensional nature of TLMCDs along with their nonlinear dynamics makes the application of gradient optimization methods difficult. Non-gradient-based methods have been employed to solve multiple inertia damper optimization problems, for example using genetic (Hadi and Arfiadi 1998 [20], Poh'sié et al. 2015 [21]), particle swarm (Leung et al. 2009 [22], Thanh and Parnichkun 2008 [23]), and simulated annealing (Febbo et al. 2012 [24], Liu 2017 et al. [25]) algorithms.

The above works are all conducted on TMDs, which are often rigid objects. The TLMCD is a MDOF liquid damper that offers larger design flexibility, for that liquid is shapeless and follows its container's geometry. The number of DOFs and damping coefficients can be altered easily by using containers of different shapes. In this paper, we study the application of a genetic algorithm to optimize the design of a TLMCD applied to both an SDOF and a 2DOF structures. The H_∞ norm is selected as the optimization goal of interest. The genetic algorithm is used to search for the near-optimum solutions. The genetic algorithm is a population-based optimization process that derived from natural biological evolution. It repeatedly updates the individual solution based on crossover and mutation methods. At each step, a new generation of populations are generated with the traits of their "parents". Over certain generations, the optimization stops when the error of tolerance is small enough or the maximum iteration number is reached (Sivanandam and Deepa 2008 [26]).

The remaining of this paper is organized as following: Section 2 introduces the analytical model for a TLMCD and a linearization method for this damper under harmonic or white noise type of excitations, Section 3 presents the equations of motion for a TLMCD on a MDOF of structure and the methodology to obtain the H_∞ norm with genetic algorithm. Section 4 compares the optimization results of both TLMCD and multiple TLCDs (MTLCDs) on various primary structures. The last section concludes the paper.

6.3 Analytical Modeling

This section summarizes the TLMCD's analytical nonlinear model presented in previous work (Wu et al. 2018 [9]) and a linearization process based on the nonlinear model.

6.3.1 Review of the nonlinear dynamic model

Consider an *N*-column TLMCD system illustrated in Figure 6.1, where $\ddot{x}_g$ is the acceleration transmitted from the primary structure, x_i is the liquid surface displacement in the i^{th} column, h is the uniform initial vertical liquid surface height in each column, l_i is the horizontal centre-to-centre distance between the i^{th} and $i+1^{\text{th}}$ columns, ψ_i is blocking ratio of the i^{th} orifice, Q_{oi}, Q_{fi}, Q_{ei} are the nonconservative forces acting on the i^{th} DOF, A is the vertical column's cross-section area, and υ is the vertical/horizontal cross-section area ratio. The TLMCD is modeled as an *N*-DOF system for DOFs x_i.

The equations governing the liquid motion are constructed using Lagrange equations:

$$\frac{\mathrm{d}}{\mathrm{d}t}\left(\frac{\partial T}{\partial \dot{x}_i}\right)-\frac{\partial T}{\partial x_i}+\frac{\partial V}{\partial x_i}=Q_{oi}+Q_{fi}+Q_{ei},\quad (i=1,2,...,N-1) \tag{6-1}$$

$$V=\frac{1}{2}\rho A\mathrm{g}\sum_{i=1}^{N}x_i^2\,, \tag{6-2a}$$

$$T=\frac{1}{2}\rho A\left\{\sum_{i=1}^{N}\dot{x}_i^2\left(h+x_i\right)+\sum_{i=1}^{N-1}\upsilon l_i\left(\sum_{j=1}^{i}\dot{x}_j\right)^2\right\} \tag{6-2b}$$

where t is time, T and V are respectively the system's kinematic and potential energy, ρ is the liquid density, and g is gravitational acceleration.

Similar to a TLCD, the nonconservative forces acting on a TLMCD system can be categorized into three types: 1) the orifice damping force Q_{oi}; 2) the friction force Q_{fi} between the liquid and column's inner surface; and 3) the liquid inertia force Q_{ei} acting on the i^{th} DOF. As is established in literature on TLCD (Gao et al. [27], Min et al. [28]), the damping force due to the orifices on the horionztal column is quadratic and its direction is oposite to that of the liquid velocity:

$$Q_{oi} = \sum_{k=i}^{N-1} \rho_l A \upsilon \left\{ \frac{1}{2} \eta_k \left| \sum_{j=1}^{k} \dot{x}_j \right| \left(\sum_{j=1}^{k} \dot{x}_j \right) \right\} \tag{6-3}$$

The frictional force is also assumed to be quadratic nonlinear forces:

$$Q_{fi} = \rho_l A \mu \left\{ \left| \dot{x}_i \right| \dot{x}_i \left(h + x_i \right) + \left| \sum_{j=1}^{N-1} \dot{x}_j \right| \left(\sum_{j=1}^{N-1} \dot{x}_j \right) \left(h - \sum_{j=1}^{N-1} x_j \right) + \sum_{k=i}^{N-1} \left(\upsilon l_k \left| \sum_{j=1}^{k} \dot{x}_j \right| \left(\sum_{j=1}^{k} \dot{x}_j \right) \right) \right\} \tag{6-4}$$

The inertia force acts only on the horizontal columns since the vertical mass of TLMCD is constant:

$$Q_{ei} = \rho_l A \ddot{x}_g \left(t \right) \sum_{k=i}^{N-1} l_k \tag{6-5}$$

Combining the above equations, the liquid motion of a N-column TLMCD is expressed as:

$$\begin{aligned} &\sum_{j=1}^{i} \left(\sum_{k=1}^{N-1} x_k - h - \sum_{k=i}^{N-1} \upsilon l_k \right) \ddot{x}_j + \sum_{j=i+1}^{N-1} \left(\sum_{k=1}^{N-1} x_k - h - \sum_{k=j}^{N-1} \upsilon l_k \right) \ddot{x}_j - \left(h + x_i \right) \ddot{x}_i + \frac{1}{2} \left(\sum_{k=1}^{N-1} \dot{x}_k \right)^2 - \frac{1}{2} \dot{x}_i^2 \\ &- \mathrm{g} x_i - \mathrm{g} \sum_{k=1}^{N-1} x_k = \mu \left| \dot{x}_i \right| \dot{x}_i \left(h + x_i \right) + \mu \left| \sum_{k=1}^{N-1} \dot{x}_k \right| \left(\sum_{k=1}^{N-1} \dot{x}_k \right) \left(h - \sum_{k=1}^{N-1} x_k \right) + \sum_{k=i}^{N-1} \upsilon \left(\mu l_k + \frac{1}{2} \eta_k \right) \left| \sum_{j=1}^{k} \dot{x}_j \right| \sum_{j=1}^{k} \dot{x}_j \\ &+ \ddot{x}_g \left(t \right) \sum_{k=i}^{N-1} l_k, \ \left(i = 1, 2, ..., N-1 \right) \end{aligned} \tag{6-6}$$

which numerical solutions can be obtained using the Runge-Kutta integration method. Prior work [9] used a numerical step size of 10^{-3} time of the expected liquid displacement amplitude to solve the equations. This nonlinear model is also referred as the general model in this paper since it applies to a TLMCD of any configuration.

6.3.2 Linearization of symmetrical TLMCDs

The nonlinear dynamic model presented above is difficult to utilize for analyzing the dynamic behavior and could be computationally time consuming in an optimization framework. Prior work [10] found that numerical solutions exhibited weak nonlinearities,

and that there exist stable resonant frequencies, in particular for geometrically symmetric configurations under harmonic and white noise excitation. Under these conditions, it was found that the liquid motion was largely restricted among opposite column pairs, i.e., $x_1 \approx x_N, x_2 \approx x_{N-1},$ etc. Under this assumption, the number of DOFs in an *N*-column TLMCD can be reduced to *N*/2, and the governing equations can be greatly simplified. These simplified equations are shown in Eq. (6-7), where the only nonlinear parts are in the quadratic damping forces.

$$\mathbf{M}_C\ddot{\mathbf{x}} + \mathbf{C}_C\mathbf{v} + \mathbf{K}_C\mathbf{x} = \boldsymbol{\alpha}\ddot{x}_g \tag{6-7}$$

where $\mathbf{x} = \begin{bmatrix} x_1 & x_2 & \cdots & x_{N/2} \end{bmatrix}^T$, $\ddot{\mathbf{x}} = \begin{bmatrix} \ddot{x}_1 & \ddot{x}_2 & \cdots & \ddot{x}_{N/2} \end{bmatrix}^T$,

$\mathbf{v} = \begin{bmatrix} |\dot{x}_1|\dot{x}_1 & |\dot{x}_2|\dot{x}_2 & |\dot{x}_3|\dot{x}_3 & \cdots & |\dot{x}_{N/2}|\dot{x}_{N/2} \end{bmatrix}$,

$$\mathbf{M}_C = \rho A \begin{bmatrix} \upsilon\left(2\sum_{k=1}^{N/2} l_k - l_{N/2}\right) + 2h & \upsilon\left(2\sum_{k=2}^{N/2} l_k - l_{N/2}\right) & \upsilon\left(2\sum_{k=3}^{N/2} l_k - l_{N/2}\right) & \cdots & \upsilon l_{N/2} \\ \upsilon\left(2\sum_{k=2}^{N/2} l_k - l_{N/2}\right) & \upsilon\left(2\sum_{k=2}^{N/2} l_k - l_{N/2}\right) + 2h & \upsilon\left(2\sum_{k=3}^{N/2} l_k - l_{N/2}\right) & \cdots & \upsilon l_{N/2} \\ \upsilon\left(2\sum_{k=3}^{N/2} l_k - l_{N/2}\right) & \upsilon\left(2\sum_{k=3}^{N/2} l_k - l_{N/2}\right) & \upsilon\left(2\sum_{k=2}^{N/2} l_k - l_{N/2}\right) + 2h & \cdots & \upsilon l_{N/2} \\ \vdots & \vdots & \vdots & \ddots & \vdots \\ \upsilon l_{N/2} & \upsilon l_{N/2} & \upsilon l_{N/2} & \cdots & \upsilon l_{N/2} + 2h \end{bmatrix}_{N/2\times N/2},$$

$$\mathbf{K}_C = \rho A \begin{bmatrix} 2\mathrm{g} & 0 & \cdots & 0 \\ 0 & 2\mathrm{g} & \cdots & 0 \\ \vdots & \vdots & \ddots & \vdots \\ 0 & 0 & \cdots & 2\mathrm{g} \end{bmatrix}_{N/2\times N/2},$$

$$\mathbf{C}_C = \rho A \begin{bmatrix} 2\upsilon(\eta_1 + \mu l_1) + 2\mu h & 2\upsilon(\eta_2 + \mu l_2) & 2\upsilon(\eta_3 + \mu l_3) & \cdots & \upsilon(\eta_{N/2} + \mu l_{N/2}) \\ 0 & 2\upsilon(\eta_2 + \mu l_2) + 2\mu h & 2\upsilon(\eta_3 + \mu l_3) & \cdots & \upsilon(\eta_{N/2} + \mu l_{N/2}) \\ 0 & 0 & 2\upsilon(\eta_3 + \mu l_3) + 2\mu h & \cdots & \upsilon(\eta_{N/2} + \mu l_{N/2}) \\ \vdots & \vdots & \vdots & \ddots & \vdots \\ 0 & 0 & 0 & \cdots & \upsilon(\eta_{N/2} + \mu l_{N/2}) + 2\mu h \end{bmatrix}_{N/2\times N/2},$$

$$\boldsymbol{\alpha} = \left[2\left(\sum_{i=1}^{N/2} l_i\right) - l_{N/2} \quad 2\left(\sum_{i=2}^{N/2} l_i\right) - l_{N/2} \quad 2\left(\sum_{i=3}^{N/2} l_i\right) - l_{N/2} \quad \cdots \quad l_{N/2} \right]^T .$$

In TLCD literature, there are two ways to linearize the quadratic liquid orifice damping force $\frac{1}{2}\eta|\dot{x}|\dot{x}$. Under white noise type excitation, the quadratic damping force can be linearized by minimizing the mean variance of error between the nonlinear damping force and a linear damping force (Xu et al. 1992 [29]; Yalla and Kareem 2000 [30]):

$$\frac{1}{2}\eta|\dot{x}|\dot{x} \approx \sqrt{\frac{2}{\pi}}\eta\sigma_{\dot{x}}\dot{x} \tag{6-8}$$

where $\sigma_{\dot{x}}$ is the standard deviation of liquid velocity $\dot{x}$. Under harmonic excitation, an equivalent viscous damping force can be obtained in terms of the amplitude of the liquid displacement in one harmonic cycle by equating the total energy dissipated in a harmonic cycle to the equivalent linear damping force (Gao et al. 1999 [27]):

$$\frac{1}{2}\eta|\dot{x}|\dot{x} \approx \frac{4}{3}\pi\eta\hat{x}\omega\dot{x} \tag{6-9}$$

where $\hat{x}$ is the amplitude of *x* under harmonic load and ω is the excitation harmonic frequency.

In both cases, the quadratic nonlinear damping matrix $\mathbf{C}_C$ can be rewritten as:

$$\mathbf{M}_C\ddot{\mathbf{x}} + \mathbf{C}_C'\mathbf{x} + \mathbf{K}_C\mathbf{x} = \boldsymbol{\alpha}\ddot{x}_g \tag{6-10}$$

$$\mathbf{C}_C\mathbf{v} \approx \mathbf{C}_C'\mathbf{x} \tag{6-11}$$

where

$$\mathbf{C}_C^{\cdot} = \rho A \begin{bmatrix} \upsilon\left(2\sum_{k=1}^{N/2} c_k - c_{N/2}\right) + \mu_1 & \upsilon\left(2\sum_{k=2}^{N/2} c_k - c_{N/2}\right) & \upsilon\left(2\sum_{k=3}^{N/2} c_k - c_{N/2}\right) & \cdots & \upsilon c_{N/2} \\ \upsilon\left(2\sum_{k=2}^{N/2} c_k - c_{N/2}\right) & \upsilon\left(2\sum_{k=2}^{N/2} c_k - c_{N/2}\right) + \mu_2 & \upsilon\left(2\sum_{k=3}^{N/2} c_k - c_{N/2}\right) & \cdots & \upsilon c_{N/2} \\ \upsilon\left(2\sum_{k=3}^{N/2} c_k - c_{N/2}\right) & \upsilon\left(2\sum_{k=3}^{N/2} c_k - c_{N/2}\right) & \upsilon\left(2\sum_{k=2}^{N/2} c_k - c_{N/2}\right) + \mu_3 & \cdots & \upsilon c_{N/2} \\ \vdots & \vdots & \vdots & \ddots & \vdots \\ \upsilon c_{N/2} & \upsilon c_{N/2} & \upsilon c_{N/2} & \cdots & \upsilon c_{N/2} + \mu_{N/2} \end{bmatrix}_{N/2 \times N/2},$$

$$\mathbf{x} = [\dot{x}_1, \dot{x}_2, \dot{x}_3, ..., \dot{x}_n]',$$

$$c_k = \sqrt{\frac{\pi}{2}}\left(\mu l_k + \frac{1}{2}\eta_k\right)\sigma_{\sum_{j=1}^{k}\dot{x}_j},\ \mu_k = 2\sqrt{\frac{\pi}{2}}\mu h \sigma_{\sum_{j=1}^{k}\dot{x}_j} \quad \text{(white noise excitation).}$$

$$c_k = \frac{4}{3}\pi\left(\mu l_k + \frac{1}{2}\eta_k\right)\omega A_{\left(\sum_{j=1}^{k} x_j\right)},\ \mu_k = \frac{8}{3}\pi\mu h\omega A_{\left(\sum_{j=1}^{k} x_j\right)} \quad \text{(harmonic excitation).}$$

where $\sigma_{\sum_{j=1}^{k}\dot{x}_j}$ and $A_{\left(\sum_{j=1}^{k} x_j\right)}$ are the standard deviation of $\sum_{j=1}^{k}\dot{x}_j$ and the amplitude of $\sum_{j=1}^{k} x_j$, respectively.

During a TLMCD design process, the value of the liquid friction coefficient μ is often taken as constant and pre-determined by the pipe material and roughness. It follows that the only damping parameters that can be designed are orifice head loss coefficients η_k, which are controlled by orifice opening ratios on the horizontal column. The relationship between η_k and the orifice opening ratio ψ_k can be illustrated with a hydraulic equation (Idelchik and Fried 1986 [31]), which can be determined through an iterative process. If c_k is a known design parameter, an initial set of η_k can be selected. The standard deviation of the system response is then computed, and Eq. (6-11) can be used to update η_k until it is stable.

In what follows, the performance of the linearization is demonstrated on a symmetric TLMCD subjected to non-simultaneous white noise and harmonic excitations. Consider a 4-

column TLMCD with the following parameters: $l_1 = l_2 = l_3 = 2$ m, $h = 1$ m, and $\eta_1 = \eta_2 = \eta_3 = 3$. The white noise acceleration signal is taken with a bandwidth of 0.5-2 Hz, and the harmonic excitation acceleration is taken as $\ddot{x}_g = 0.1\sin(t)\ \text{m/s}^2$. Figure 6.2 (a) and (b) compares results from the numerical solutions of the general dynamic model (Eq. (6-6)), symmetric model (Eq. (6-7)), and the final linearized model (Eq. (6-10)) under the harmonic and white noise excitation, respectively. Results show that there is basically no difference between the nonlinear model and the symmetric model, and a slight difference occurs when the nonlinear damping forces are linearized. The largest displacement difference between the linear and nonlinear models under the white noise excitation is 2% of the initial height, which is acceptable considering the large amplitude of liquid motion. The difference becomes even smaller under the harmonic loading. It is also noted that the assumption that the liquid motion is symmetric under stationary excitations is validated as well, as shown in Figure 6.3 where the displacements of the nonlinear model's all four columns are compared.

In the following study, unless declared, the linearized model is applied to investigate the optimal damping effect of a TLMCD on different primary structures.

6.4 Methodology

This section presents the methodology used to conduct the simulations, including the numerical model for a structure equipped with a TLMCD and the parameters of the example structures.

6.4.1 Numerical model

If the primary structure is a MDOF building that has *m* stories and equips with an *N*-column TLMCD on the top, which is shown in Figure 6.4, the equations of motion are modified as:

$$\left[\begin{array}{c|c} \mathbf{M}_C & \begin{matrix} & \boldsymbol{\alpha} & \mathbf{0} \end{matrix} \\ \hdashline \begin{matrix} \boldsymbol{\alpha} \\ \mathbf{0} \end{matrix} & \begin{bmatrix} m_d & \cdots & 0 \\ \vdots & \ddots & \vdots \\ 0 & \cdots & 0 \end{bmatrix} + \mathbf{M}_S \end{array}\right] \begin{bmatrix} \ddot{\mathbf{x}} \\ \ddot{\mathbf{x}}_s \end{bmatrix} + \begin{bmatrix} \mathbf{C}_C^{'} & \mathbf{0} \\ \mathbf{0} & \mathbf{C}_S \end{bmatrix} \begin{bmatrix} \dot{\mathbf{x}} \\ \dot{\mathbf{x}}_s \end{bmatrix} + \begin{bmatrix} \mathbf{K}_C & \mathbf{0} \\ \mathbf{0} & \mathbf{K}_S \end{bmatrix} \begin{bmatrix} \mathbf{x} \\ \mathbf{x}_s \end{bmatrix} = \begin{bmatrix} \mathbf{0} \\ \mathbf{F} \end{bmatrix} \quad (6\text{-}12)$$

where $\mathbf{x}_s \in \mathbb{R}^{m\times 1}$, $\mathbf{M}_s \in \mathbb{R}^{m\times m}$, $\mathbf{K}_s \in \mathbb{R}^{m\times m}$, $\mathbf{C}_s \in \mathbb{R}^{m\times m}$ are respectively the *m*-dimensional primary structure's mass, stiffness and damping matrices, $\boldsymbol{\alpha}$ is the horizontal mass matrix mentioned in Section 2, m_d is the TLMCD's total mass, $\mathbf{x} \in \mathbb{R}^{N/2\times 1}$, $\mathbf{M}_c \in \mathbb{R}^{N/2\times N/2}$, $\mathbf{K}_c \in \mathbb{R}^{N/2\times N/2}$, $\mathbf{C}_c \in \mathbb{R}^{N/2\times N/2}$, are respectively the displacement, mass, stiffness and damping matrices of the TLMCD, and $\mathbf{F} \in \mathbb{R}^{m\times 1}$ is the external force matrix that acting on different locations of the primary structure.

For a special case, the equations of motion of an SDOF structure equipped with an *N*-column TLMCD can be written as:

$$\begin{bmatrix} \mathbf{M}_C & \boldsymbol{\alpha} \\ \rho A \boldsymbol{\alpha}^T & m_s + m_d \end{bmatrix} \begin{bmatrix} \ddot{\mathbf{x}} \\ \ddot{x}_s \end{bmatrix} + \begin{bmatrix} \mathbf{C}_C^{'} & \mathbf{0} \\ \mathbf{0} & c_s \end{bmatrix} \begin{bmatrix} \dot{\mathbf{x}} \\ \dot{x}_s \end{bmatrix} + \begin{bmatrix} \mathbf{K}_C & \mathbf{0} \\ \mathbf{0} & k_s \end{bmatrix} \begin{bmatrix} \mathbf{x} \\ x_s \end{bmatrix} = \begin{bmatrix} \mathbf{0} \\ F \end{bmatrix} \quad (6\text{-}13)$$

where m_s, k_s, and c_s are the primary structure's mass, stiffness and linear viscous damping coefficient, respectively.

In both cases, they are linear systems, and matrices are used to denote the above two equations:

$$\mathbf{M}_p \ddot{\mathbf{p}} + \mathbf{C}_p \dot{\mathbf{p}} + \mathbf{K}_p \mathbf{p} = \mathbf{B}_d \mathbf{F} \quad (6\text{-}14)$$

where $\mathbf{p} = \begin{bmatrix} \mathbf{x} & \mathbf{x_s} & \dot{\mathbf{x}} & \dot{\mathbf{x}}_\mathbf{s} \end{bmatrix}^T \in \mathbb{R}^{(N+2m)\times 1}$, and $\mathbf{B_d} \in \mathbb{R}^{(N+2m)\times m}$ is the external force location matrix.

This equation can be further written as control system in State-Space form, with the external force amplitude as the input and the primary structure's displacement as the output:

$$\dot{\mathbf{p}} = \mathbf{A}_1\mathbf{p} + \mathbf{B}_1\mathbf{F}$$
$$\mathbf{z} = \mathbf{C}_1\mathbf{p} + \mathbf{D}_1\mathbf{F} \tag{6-15}$$

where $\mathbf{A}_1 = \begin{bmatrix} \mathbf{0} & \mathbf{I} \\ -\mathbf{M}_p^{-1}\mathbf{K}_p & -\mathbf{M}_p^{-1}\mathbf{C}_p \end{bmatrix}_{(N+2m)\times(N+2m)}$,

$$\mathbf{B}_1 = \begin{bmatrix} \mathbf{0} \\ \mathbf{M}_p^{-1}\mathbf{B}_d \end{bmatrix}_{(N+2m)\times m},$$

$$\mathbf{C}_1 = \left[\mathbf{0}_{1\times N/2} \; \overbrace{\underbrace{1 \;\; 0 \;\; \ldots \;\; 0}_{\text{location can vary}}}^{m \text{ dimension}} \; \mathbf{0}_{1\times(N/2+m)} \right]_{1\times(N+2m)},$$

$$\mathbf{D}_1 = \mathbf{0}_{1\times m}.$$

6.4.2 Optimization objective

The H_∞ norm of the control system is chosen to be the optimization goal:

$$\mathbf{H}(j\omega) = \mathbf{C_c}\left((j\omega)\mathbf{I} - \mathbf{A_c}\right)^{-1}\mathbf{B_c} + \mathbf{D_c} \tag{6-16}$$

$$\|H\|_\infty^2 = \sup_{\omega\in R} \sigma_{\max}^2\left(\mathbf{H}(j\omega)\right) \tag{6-17}$$

where $\sigma_{\max}$ is the maximum singular value, *H(jω)* is the transfer function of the State-Space system. H_∞ norm optimization method is a commonly used technique to optimize a damper's configuration. For Single-Input-Single-Output (SISO) systems, the H_∞ norm is the largest magnitude of steady frequency response under harmonic excitation.

In this study, we apply genetic algorithm optimization to search for the near-optimum solutions. The genetic algorithm is encoded in the Optimization Tool Box of MATLAB. If an N-column TLMCD is attached to an m-dimension primary structure, the suggested population size of the optimization process is 20 (N+m).

6.5 Optimization Results

6.5.1 Sing-degree-of-freedom primary structures

In either TLCD or TLMCD design, the liquid mass in the horizontal column is considered more "effective" than that in the vertical column, since the TLCDs/TLMCDs only suppress horizontal vibration of the primary structure and the interaction force between the damper and structure is transferred by the inertia of the horizontal liquid mass. Under the same total mass, the larger percentage is the horizontal mass, the more horizontal motion is transferred from structure to the liquid damper. The length ratio of a TLCD or a TLMCD is defined as:

$$\gamma = \frac{l}{2h + l} \tag{6-18}$$

Thus, a large horizontal/vertical length ratio, which corresponds to a large percentage horizontal liquid mass, will always lead to a higher efficiency for a liquid damper. However, in practice, due to space limitation and the fact that the liquid displacement should not be lower than the initial vertical height, the design of TLCD/TLMCD often begins with a presumed horizontal/vertical length ratio, typically ranging from 0.7 to 0.9 (Shum 2009 [32]).

For a TLMCD, the H_∞ norm is a function of column spacings l_i, length ratio γ, orifice head loss coefficients c_i, and horizontal/vertical area ratio υ. Following the practice of the TLCD/TLMCD optimal design, a mass ratio of 5% and a length ratio of 0.9 is presumed, and the remaining parameters are optimized simultaneously.

Consider a SDOF structure with the following structural parameters: m_s =1, ω_s = 1.1 rad/s, ξ_s =0.02, m_d/m_s = 0.05, γ = 0.9. The optimized parameters of a TLCD and a TLMCD are listed in Table 6.1.

A comparison between transfer functions of structures attached with the optimized TLCD and TLMCD is conducted. The TLCD optimization result shows that the highest efficiency is achieved when the horizontal and vertical columns have the same cross-section area ($\upsilon = 1$), and this agrees with the conclusion in literature (Wu et al. 2005 [33]). Based on the H_∞ norm optimization result, a TLMCD does not perform better than a TLCD under the same mass ratio and the same length ratio. In fact, the relationship between optimized H_∞ norm and column spacing ratio (Figure 6.5) shows that the optimized H_∞ norm of the 4-column TLMCD will be larger than the optimized TLCD's H_∞ norm under all column spacing ratios, though the difference is small (less than 5%). If the column spacings are equal, the comparisons of transfer functions of TLCD and the equally-spaced TLMCD are illustrated in Figure 6.6. When the first column spacing reduces to zero, the 4-column TLMCD regresses into the optimized TLCD. The explanation for the phenomenon is that the effective mass of a TLCD is more concentrated into one vibration mode than a TLMCD, while only the first vibration mode of the TLMCD is involved in suppressing the primary structure. Though some researchers (Zuo and Nayfey [19]) found 2-DOF mass dampers could have better efficiency than SDOF mass dampers in damping SDOF structures when the structure's natural frequency falls between the damper's first two natural frequencies. This phenomenon is not observed in this optimization process because the two natural frequencies of a TLMCD are always far apart unless the TLMCD has a small percentage of horizontal mass, under which situation the TLMCD does not have enough effective mass in the first vibration mode. Thus, a TLCD is considered always more effective than a TLMCD under the restriction of the same mass ratio and length ratio.

6.5.2 Two-degree-of-freedom primary structures

In control of a 2-DOF primary system, when the output are the two primary structure displacements at each DOF and the input is a n-dimension force, the H_∞ norm is the singular value of n x 2 transfer functions. However, engineers are often more concerned about the maximum value of the two displacements rather than the singular value of the whole system. As a result, when evaluating the damping performance of dampers on a 2-DOF primary system, we prefer to define the optimization criteria as the larger of the two SISO H_∞ norm:

$$\text{Sys 1: } \mathbf{B}_d\mathbf{F} = [0 \quad 0 \quad 1 \quad 0], \mathbf{C} = [0 \quad 0 \quad 1 \quad 0]; \tag{6-19}$$

$$\text{Sys 2: } \mathbf{B}_d\mathbf{F} = [0 \quad 0 \quad 0 \quad 1], \mathbf{C} = [0 \quad 0 \quad 0 \quad 1];$$

Optimization objective = max [$\left(H_\infty\right)_1$ norm, $\left(H_\infty\right)_2$ norm]

In each SISO control system, the input is the unit harmonic force acting on the first/second DOF of the primary structure, and the output is the structure displacement of that DOF.

A 2-storey structure has the following structure parameters:

$$\mathbf{M}_S = \begin{bmatrix} 1 & 0 \\ 0 & 2 \end{bmatrix}, \mathbf{K}_S = \begin{bmatrix} 1 & -1 \\ -1 & 3.5 \end{bmatrix}, \mathbf{C}_S = \begin{bmatrix} 0.032 & 0.048 \\ 0.048 & 0.112 \end{bmatrix} \tag{6-20}$$

The damping coefficients correspond to a 5% damping ratio in the first vibration mode and a 2% damping ratio in the second vibration mode. We will compare the optimized damping performance of a 4-column symmetric TLMCD, a single TLCD and two individual TLCDs when they are attached to the second floor, as shown in Figure 6.7.

Like the last section, when we do the optimization task, the length ratio γ is fixed as 0.9 for the TLMCD as well as the two TLCDs. Genetic algorithm optimization is performed with all dampers having the same total mass. The individual column spacing of the TLMCD,

horizontal lengths of each TLCD, and various orifice damping coefficients are varied in the optimization process. All these parameters are optimized simultaneously, with the optimized results listed in Table 6.2.

The two SISO transfer functions of the two TLCDs and the 4-column TLMCD on suppressing the 2-DOF structure is shown in Figure 6.8. When the input excitation is acting on the first DOF of the primary structure, the maximum displacement is at the first floor, as shown in Figure 6.8 (a); and the same is for input excitation acting on the second floor, as shown in Figure 6.8 (b). The optimized results ensure that the larger of the two transfer functions' peak values is minimized. In the optimized results, the 4-column TLMCD's two natural frequencies match the two natural frequencies of the primary structure, with two tuning ratios as $\chi_1 = \omega_1 / \omega_{s1} = 0.935$, and $\chi_2 = \omega_2 / \omega_{s2} = 0.997$. The second tuning ratio is closer to 1 because the transfer function curves at the second frequency are very steep. Generally, the 4-column TLMCD performs better than single TLCD or any other combination of two TLCDs. Single TLCD has the worst damping effect since it cannot control two vibration modes at the same time. For two TLCDs, if they have an equal mass, the TLMCD's optimized H_∞ norm is 21% large than that of optimized multiple TLCDs. The difference can be reduced to 5% if the mass ratio of the two TLCDs is optimized (Table 6.3).

6.6 Conclusions

TLMCD is an extension of classical TLCDs into MDOF domains. The general TLMCD model is a complex nonlinear system, but for a symmetrical TLMCD. But the nonlinear equations of motion in the analytical model can be linearized using the energy equivalent method. Numerical calculations showing that the linear model is a good approximation for predicting the liquid motion inside a symmetrical TLMCD under white

noise and harmonic excitation accelerations. With the linearized model, the equations of motion of a TLMCD are rewritten into State-Space form, and H_∞ norm is selected as the optimization goal of interest. Multiple parameters, including the column spacings, orifice blocking ratios, and vertical/horizontal cross-section area ratios, can be optimized simultaneously using a genetic optimization algorithm. Optimization results show that when attached to a SDOF primary structure, the TLMCD's damping performance is comparable although slightly less effective than that of TLCD with the same mass and length ratio. Only the first vibration mode of the 4-column TLMCD is effective. The effective mass of the first mode of TLMCD is always smaller than that of the optimized TLCD under these restrictions, since its mass is distributed into other vibration modes. In the optimal case, all column spacings except one reduces to zero, which regresses into a TLCD.

However, for MDOF structures, optimization results indicate that the TLMCD can outperform single TLCD and MTLCDs with the same liquid mass and length ratio. This is attributed to that, in a TLMCD, the sum of the effect masses of various modes can exceed the actual total mass. As a result, there exists a situation where TLMCD has larger effective masses in all vibration modes than the optimized MTLCDs.

6.7 References

[1] M.D. Symans, F.A. Charney, A.S. Whittaker, M.C. Constantinou, C.A. Kircher, M.W. Johnson, R.J. Mcnamara, Energy Dissipation Systems for Seismic Applications: Current Practice and Recent Developments, J. Struct. Eng. 134 (2008) 3–21. https://doi:10.1061/(ASCE)0733-9445(2008)134:1(3).

[2] J. Connor, S. Laflamme, Structural motion engineering, Springer, New York, 2014.

[3] X. Lu, Q. Zhang, D. Weng, Z. Zhou, S. Wang, S.A. Mahin, S. Ding, F. Qian, Improving performance of a super tall building using a new eddy-current tuned mass damper, Struct. Control Heal. Monit. 24 (2017) 1–17. doi:10.1002/stc.1882.

[4] N. Debnath, S.K. Deb, A. Dutta, Multi-modal vibration control of truss bridges with tuned mass dampers under general loading, Journal Vib. Control. 22 (2016) 4121–4140. doi:10.1177/1077546315571172.

[5] G.M. Stewart, M.A. Lackner, The impact of passive tuned mass dampers and wind-wave misalignment on offshore wind turbine loads, Eng. Struct. 73 (2014) 54–61. doi:10.1016/j.engstruct.2014.04.045.

[6] A. Di Matteo, F. Lo Iacono, G. Navarra, A. Pirrotta, Innovative modeling of Tuned Liquid Column Damper motion, Commun. Nonlinear Sci. Numer. Simul. 23 (2015) 229–244. doi:10.1016/j.cnsns.2014.11.005.

[7] K.W. Min, C.S. Park, J. Kim, Easy-to-tune reconfigurable liquid column vibration absorbers with multiple cells, Smart Mater. Struct. 24 (2015). doi:10.1088/0964-1726/24/6/065041.

[8] L. Rozas, R. L. Boroschek, A. Tamburrino, M. Rojas, A bidirectional tuned liquid column damper for reducing the seismic response of buildings, Struct. Control Health Monit. 23 (2016) 621-640. https://doi: 10.1002/stc.1784

[9] C. Coudurier, O. Lepreux, N. Petit, Modelling of a tuned liquid multi-column damper. Application to floating wind turbine for improved robustness against wave incidence, Ocean Eng. 165 (2018) 277–292. doi:10.1016/j.oceaneng.2018.03.033.

[10] H. Wu, S. Laflamme, A. Chen, A nonlinear dynamic model for tuned liquid multiple columns damper, J. Sound Vib. (2019) (under review)

[11] Y.L. Cheung, W.O. Wong, H-infinity optimization of a variant design of the dynamic vibration absorber - Revisited and new results, J. Sound Vib. 330 (2011) 3901–3912. doi:10.1016/j.jsv.2011.03.027.

[12] S. Chun, Y. Lee, T.H. Kim, H∞ optimization of dynamic vibration absorber variant for vibration control of damped linear systems, J. Sound Vib. 335 (2015) 55–65. doi:10.1016/j.jsv.2014.09.020.

[13] X. Tang, Y. Liu, W. Cui, L. Zuo, Analytical Solutions to H_2 and H_∞ Optimizations of Resonant Shunted Electromagnetic Tuned Mass Damper and Vibration Energy Harvester, J. Vib. Acoust. 138 (2015) 011018. doi:10.1115/1.4031823.

[14] H. Sun, Y. Luo, X. Wang, L. Zuo, Seismic control of a SDOF structure through electromagnetic resonant shunt tuned mass-damper-inerter and the exact H2optimal solutions, J. Vibroengineering. 19 (2017) 2063–2079. doi:10.21595/jve.2017.18256.

[15] I. Venanzi, Robust optimal design of tuned mass dampers for tall buildings with uncertain parameters, Struct. Multidiscip. Optim. 51 (2015) 239–250. doi:10.1007/s00158-014-1129-4.

[16] C.-C. Lin, G.-L. Lin, K.-C. Chiu, Robust Design Strategy for Multiple Tuned Mass Dampers with Consideration of Frequency Bandwidth, Int. J. Struct. Stab. Dyn. 17 (2017) 1750002. doi:10.1142/S021945541750002X.

[17] F. Ubertini, G. Comanducci, S. Laflamme, A parametric study on reliability-based tuned-mass damper design against bridge flutter, Journal Vib. Control. 23 (2017) 1518–1534. doi:10.1177/1077546315595304.

[18] R. Greco, G. C. Marano, A. Fiore, Performance–cost optimization of tuned mass damper under low-moderate seismic actions, Struct. Design Tall Spec. Build. 25(2016) 1103-1122. doi: 10.1002/al.1300

[19] L. Zuo, S.A. Nayfeh, The Two-Degree-of-Freedom Tuned-Mass Damper for Suppression of Single-Mode Vibration Under Random and Harmonic Excitation, J. Vib. Acoust. 128 (2006) 56. doi:10.1115/1.2128639.

[20] M.N.S. Hadi, Y. Arfiadi, Optimum Design of Absorber for MDOF Structures, J. Struct. Eng. 124 (1998) 1272–1280. doi:10.1061/(ASCE)0733-9445(1998)124:11(1272).

[21] G. Hervé Poh'sié, C. Chisari, G. Rinaldin, M. Fragiacomo, C. Amadio, A. Ceccotti, Application of a Translational Tuned Mass Damper Designed by Means of Genetic Algorithms on a Multistory Cross-Laminated Timber Building, J. Struct. Eng. 142 (2016) E4015008. doi:10.1061/(ASCE)ST.1943-541X.0001342.

[22] A.Y.T. Leung, H. Zhang, Particle swarm optimization of tuned mass dampers, Eng. Struct. 31 (2009) 715–728. doi:10.1016/j.engstruct.2008.11.017.

[23] B.T. Thanh, M. Parnichkun, Balancing control of bicyrobo by particle swarm optimization-based structure-specified mixed H2/H∞ control, Int. J. Adv. Robot. Syst. 5 (2008) 395–402. doi:10.5772/6235.

[24] M. Febbo, Optimal Parameters and Characteristics of a Three Degree of Freedom Dynamic Vibration Absorber, J. Vib. Acoust. 134 (2012) 021010.doi:10.1115/1.4004667.

[25] M. Liu, W. Liang, Y. Lin, Simulated annealing optimization of tuned mass dampers for vibration control of seismic-excited buildings, Proc. 9th Int. Conf. Appl. Oper. Res. 9 (2017) 1–9.

[26] Sivanandam, S. N., and Deepa, S. N. (2008). Genetic algorithm optimization problems. In Introduction to Genetic Algorithms (pp. 165-209). Springer, Berlin, Heidelberg.

[27] H. Gao, K.S.C. Kwok, B. Samali, Characteristics of multiple tuned liquid column dampers in suppressing structural vibration, Eng. Struct. 21 (1999) 316–331. doi:10.1016/S0141-0296(97)00183-1.

[28] K.W. Min, Y.W. Kim, J. Kim, Analytical and experimental investigations on performance of tuned liquid column dampers with various orifices to wind-excited

structural vibration, J. Wind Eng. Ind. Aerodyn. 139 (2015) 62–69. doi:10.1016/j.jweia.2015.01.014.

[29] Y.L. Xu, B. Samali, K.C.S. Kwok, Control of along-wind response of structures by mass and liquid dampers, J. Eng. Mech. 118(1992) 20–39.

[30] S.K. Yalla, A. Kareem, Optimum Absorber Parameters for Tuned Liquid Column Dampers, J. Struct. Eng. 126 (2000) 906–915. doi:10.1061/(ASCE)0733-9445(2000)126:8(906).

[31] E. Idelchik, E. Fried, Handbook of hydraulic resistance, second ed., Hemisphere, Washington DC, 1986.

[32] K.M. Shum, Closed form optimal solution of a tuned liquid column damper for suppressing harmonic vibration of structures, Eng. Struct. 31 (2009) 84–92. doi:10.1016/j.engstruct.2008.07.015.

[33] J.C. Wu, M.H. Shih, Y.Y. Lin, Y.C. Shen, Design guidelines for tuned liquid column damper for structures responding to wind, Eng. Struct. 27 (2005) 1893–1905. doi:10.1016/j.engstruct.2005.05.009.

Table 6.1 *Comparisons of a 4-column TLMCD and a TLCD on suppressing vibration of a SDOF primary structure (all damper masses = 0.05)*

Dampers	Optimized Parameters	Results
4-column TLMCD of equal spacing	Uniform column spacing l_i	8.643
	First orifice damping coefficient c_1	4.473
	Second orifice damping coefficient c_2	0.720
	Vertical/horizontal mass ratio υ	0.511
Single TLCD	Length l	16.04
	Orifice damping c	39.4
	Vertical/horizontal area ratio υ	1.001

Table 6.2 *Comparisons of optimum parameters of a 4-column TLMCD, single TLCD, and two TLCDs on suppressing vibration of a 2DOF primary structure (all damper masses = 0.05)*

Dampers	Optimized Parameters	Results
4-column TLMCD	First column spacing l_1	8.45
	Second column spacing l_2	22.24
	First orifice damping coefficient c_1	0.125
	Second orifice damping coefficient c_2	3.05
	Vertical/horizontal area ratio υ	0.898
Two TLCDs with optimized mass ratio	First TLCD length l_1	37.66
	Second TLCD length l_2	9.32
	First orifice damping coefficient c_1	5.54
	Second orifice damping coefficient c_2	2.52
	Mass distribution	83% : 17 %
Two TLCDs with equal mass ratio	First TLCD length l_1	37.62
	Second TLCD length l_2	9.30
	First TLCD orifice damping c_1	8.56
	Second TLCD orifice damping c_2	0.60
Single TLCD	Length l	49.66
	Orifice damping c	61.58
	Vertical/horizontal area ratio υ	1.000

Table 6.3 *Comparisons of effective masses at each vibration mode*

Effective mass at each vibration mode	First vibration mode	Second vibration mode
Optimized 4-column TLMCD	0.0462	0.0108
Two TLCDs of optimized mass ratio	0.0414	0.0086

Table 6.4 *H_∞ Comparisons of a 4-column TLMCD, single TLCD, and two TLCDs on suppressing vibration of a 2DOF primary structure*

Mounted Dampers	$(H_\infty)_1$ norm	$(H_\infty)_2$ norm	$\max\left[(H_\infty)_1 \text{ norm}, (H_\infty)_2 \text{ norm}\right]$
4-column TLMCD	6.71	6.65	6.71
TLCDs with equal mass	7.89	7.86	7.89
Two TLCDs optimized mass	6.89	6.86	6.89
Single TLCD	7.82	7.74	7.82

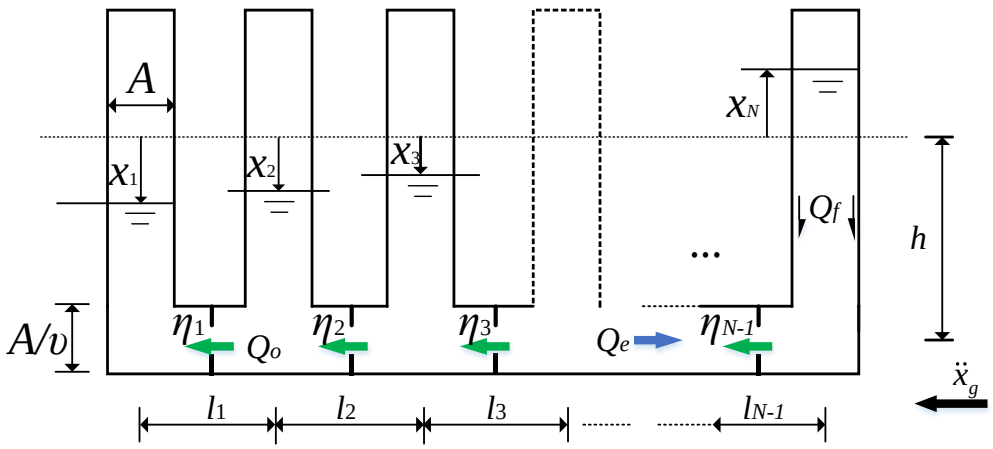

Figure 6.1 *Schematic drawing of a N-column TLMCD*

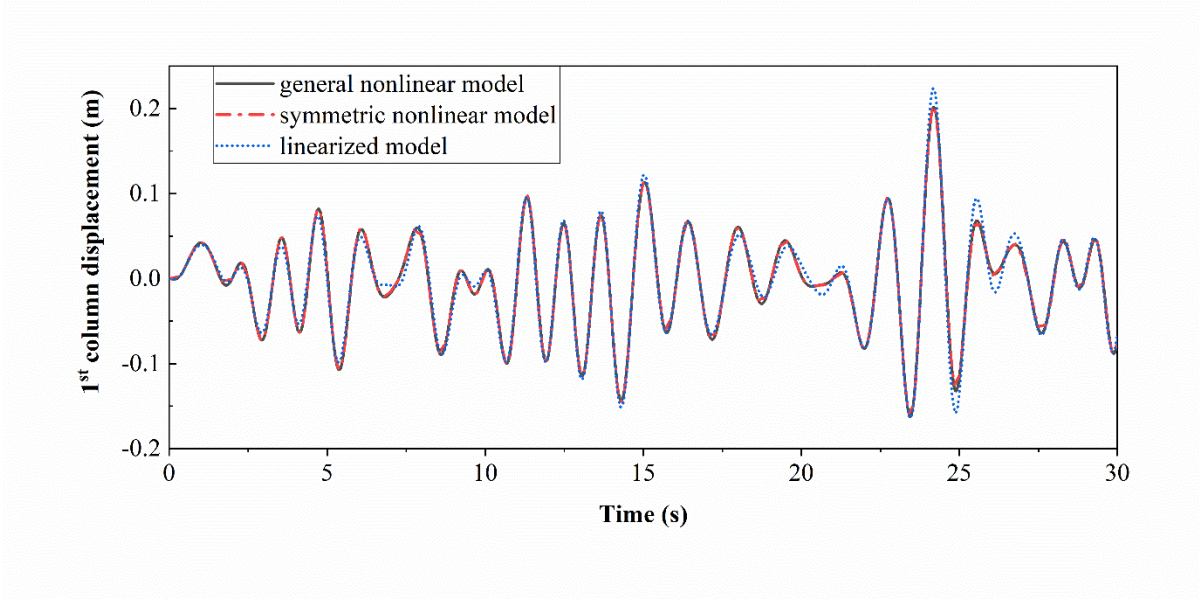

(a)

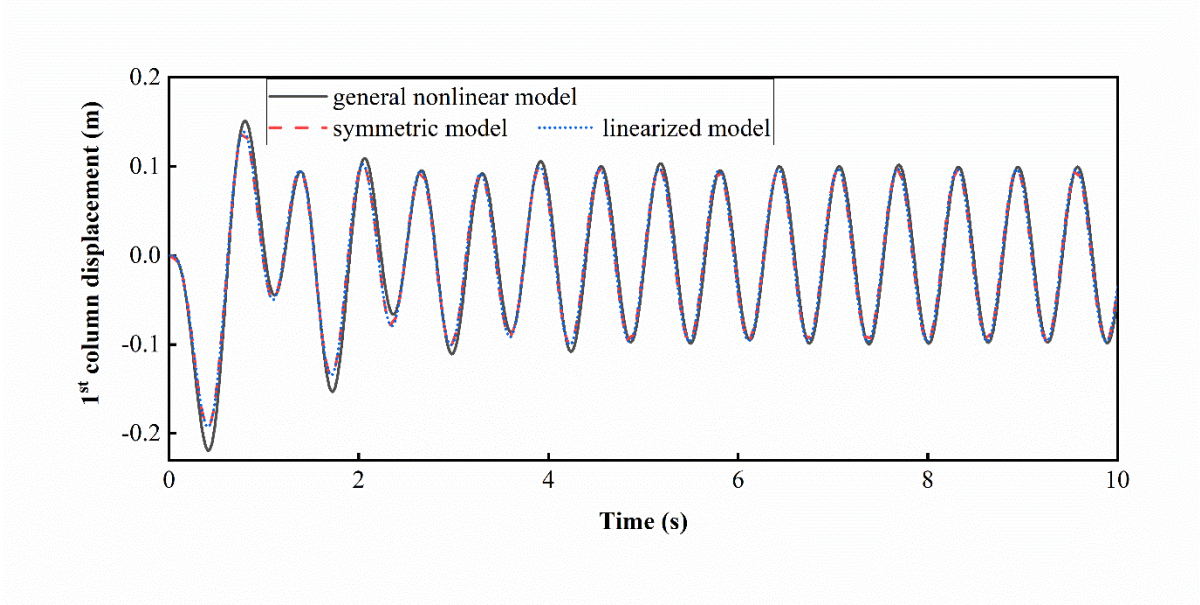

(b)

Figure 6.2 *Comparisons of the numerical solutions for the 1st column displacement under (a) white noise excitation; and (b) harmonic excitation.*

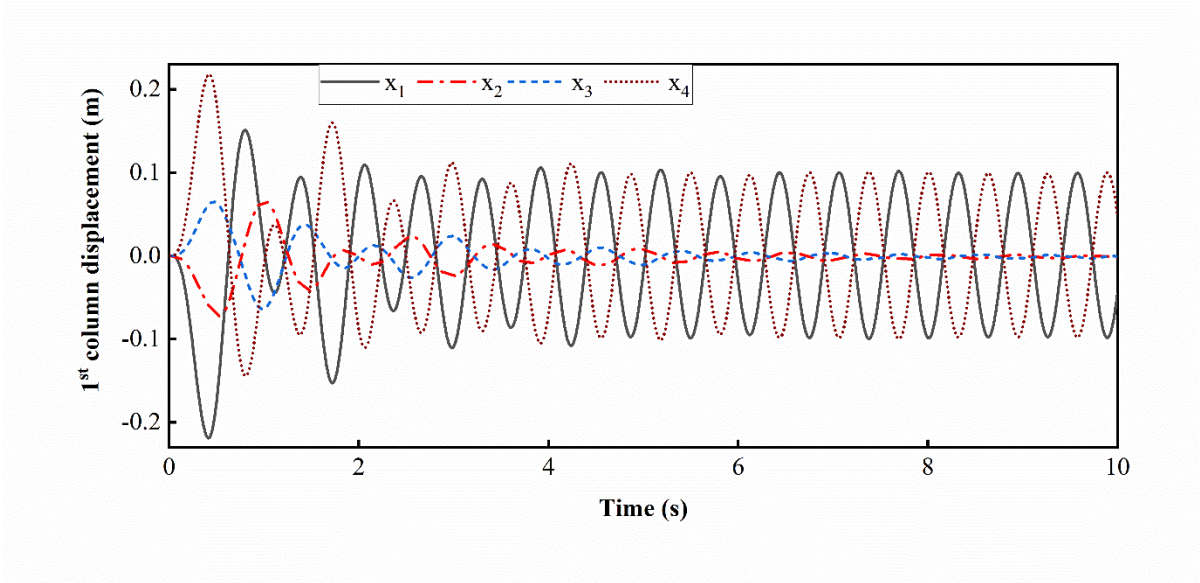

Figure 6.3 *Validation of the symmetricity assumption by the nonlinear model*

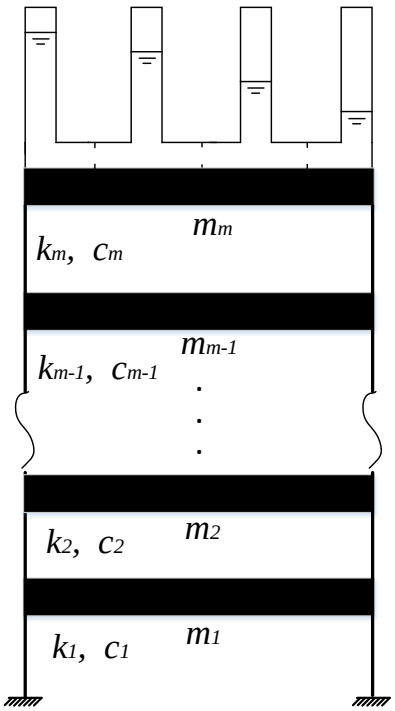

Figure 6.4 *TLMCD mounted on the top of a MDOF structure*

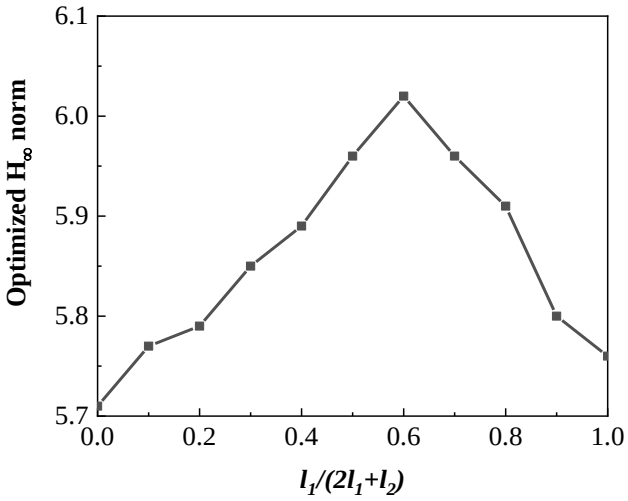

Figure 6.5 *The influence of 4-column TLMCD's column spacing ratios on the optimized H_∞ norm*

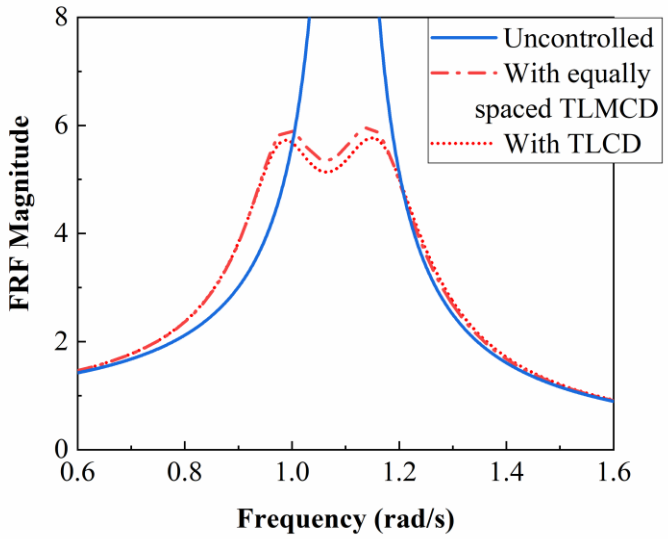

Figure 6.6 *Transfer function of a SDOF primary structure attached with an optimized TLCD and an optimized 4-column TLMCD of equal spacing*

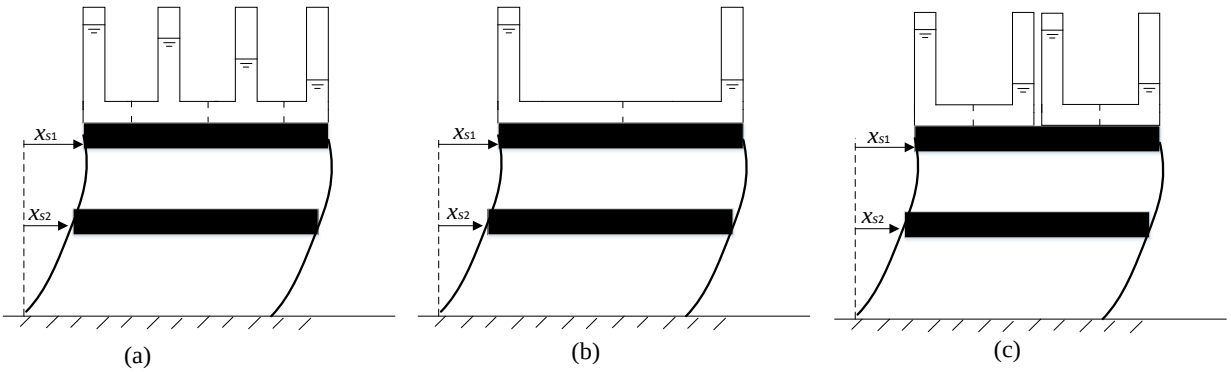

Figure 6.7 *Comparison of (a) a 4-column TLMCD, (b) single TLCD, and (c) two TLCDs on suppressing vibration of a 2-DOF primary structure*

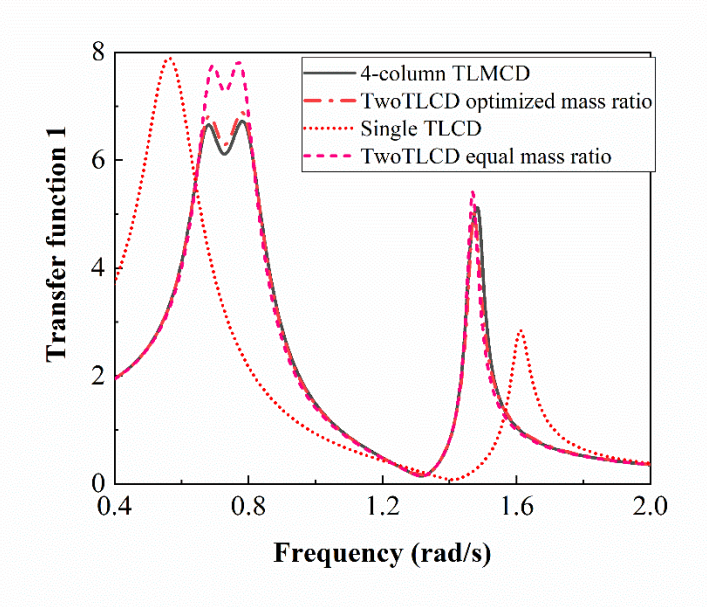

(a)

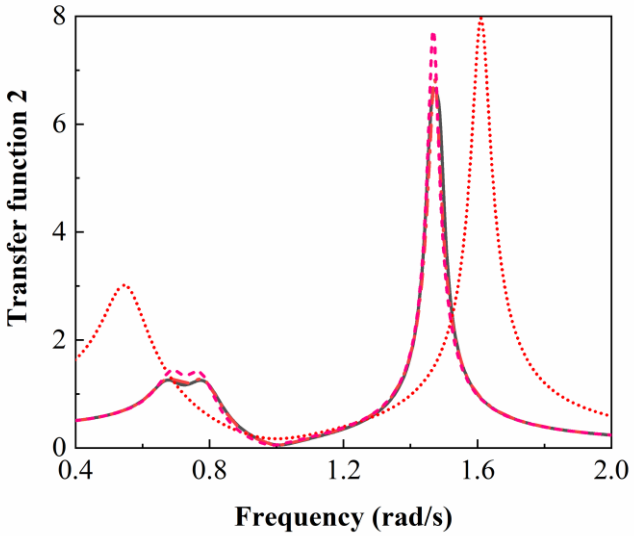

(b)

Figure 6.8 *Transfer functions of 4-column TLMCD, single TLCD, and two TLCDs attached on a 2DOF primary structure (a) with input and output at the first DOF (b) with input and output at the second DOF*

CHAPTER 7. SEMI-ACTIVE TUNED LIQUID MULTIPLE COLUMNS DAMPER FOR MITIGATION OF WIND HAZARD

A paper to be submitted to *Journal of Wind Engineering and Industrial Aerodynamics*

Hao Wu, Yongqiang Gong, Simon Laflamme and An Chen

7.1 Abstract

A tuned liquid multiple columns damper (TLMCD) is a multiple-tubes system filled with oscillating liquid to dissipate vibration energy against wind or seismic hazard. It consists of multiple vertical tubes connected by a horizontal tube with internal orifices, and liquid flow through these orifices will generate viscous damping that slows liquid motion. This study investigates the enhanced damping effect when the orifices of a TLMCD are replaced by semi-actively controlled valves. The semi-active control forces provided by the controllable valves are determined by a sliding mode control method with a self-defined weight matrix. If wind load is modeled as a harmonic force, the transfer function of a SDOF structure equipped with a semi-active TLMCD shows that significant improvement is achieved when comparing the semi-active case versus its passive counterpart. When stochastic wind hazards are applied to a 20-story benchmark building with a semi-active TLMCD placed on the top, numerical simulations conclude that the semi-active design has smaller average inter-story drifts and average acceleration compared to a passive TLMCD or an optimized passive tuned liquid column damper (TLCD) of equal mass.

Keywords: semi-active, tuned liquid column damper, sliding mode control, wind hazard, transfer function.

7.2 Introduction

The increasing height and flexibility of modern buildings leads to their vulnerability to wind and earthquake loads, which could cause malfunction, discomfort and even structural failure. Enhancing structural damping to mitigate structural vibration is a widely investigated topic for civil engineers and researchers. Generally, the devices and techniques for increasing structural damping can be categorized into three types, the passive, semi-active and active ones. Passive damping devices, such as passive tuned mass dampers (TMDs) and tuned liquid dampers (TLDs), are often viewed as reliable and easy to implement mainly due to no requirement of external power. However, passive damping is not always effective in all situations, and semi-active and active dampers, which has the ability to determine the present state of the structure and respond in a controllable manner, have better efficiency and offer solutions to a wide range of problems (Symans and Constantinou 1999). The difference between semi-active and active dampers is that semi-active only requires a small amount of energy to change the structural properties and always produces a damping force contrary to the structure motion. As a result, semi-active dampers never destabilize a structural system (Conner and Laflamme 2014). In this study we are investigating a semi-active tuned liquid multiple columns damper (TLMCD) with liquid damping controlled by internal valves.

Tuned liquid column dampers (TLCDs) is a popular type of TLDs that utilizes the liquid motion in a U-shaped tube to mitigate the main structure's vibration under external load. The stiffness is provided by gravity in the two vertical columns, and the damping is induced by the liquid flow through an internal orifice in the horizontal column. Because of its cost-effectiveness, low maintenance and easy installation, it has been widely used in high-rise buildings (Sakai et al. 1989, Chakraborty et al. 2012). A TLMCD is an extension of classical TLCDs, which are single-degree-of-freedom (SDOF) systems. A TLMCD consists

of a multiple-tubes system filled with oscillating liquid and is also a multiple-degrees-of-freedom (MDOF) system. The multiple vertical tubes are connected by a horizontal tube, and liquid flow through one vertical tube to another will pass through orifices in the horizontal tube, generating viscous damping forces (Wu et al. 2017). Comparing to TLCDs, TLMCDs have space efficiency due to the multiple-tubes feature. Also, since TLMCDs have multiple vibration modes, they are more effective in suppressing the vibrations of MDOF structures.

For active TLCDs, propellers can be used to change the TLCD's stiffness (Chen and Ko 2003), which will consume a large amount of energy. For semi-active TLCDs/TLMCDs, since the container holding the liquid has a fixed geometry, only the liquid damping needs to be controlled with a small force. As a result, semi-active TLCDs are stable systems since the liquid damping force is always contrary to the liquid motion. There are two ways to control the liquid damping: one is using a controllable valve that can adjust the opening ratio in the horizontal column, and the other one is magneto-rheological (MR) fluids controlled by external magnetic fields (Sun et al. 2016, Wang et al. 2005). Shinozuka et al. (1992) first introduced a two-stage semi-active fluid damper that was controlled by a solenoid valve, which could be opened and closed by an electrical signal. Yalla and Kareem (2001,2003) compared three control strategies of semi-active tuned liquid column dampers: continuous LQR/LQG type control, simple on-off control and fuzzy control though numerical examples, concluding that semi-active dampers can improve the performance of passive dampers by 15-25%, and continuously varying control algorithm does not provide a significant improvement over the simple on-off strategy. Coudurier et al. (2015) conducted a simulation on the performance of semi-active TLCDs on offshore floating wind turbine using the classic LQR control method. Wang et al. (2003) investigated the effectiveness of MR-TLCDs in

mitigating the wind-induced response of high-rise buildings, showing that they are capable of achieving much better vibration reduction than normal TLCDs.

TLMCDs, similar to TLCDs, can use controllable valves as a semi-active control mechanism to better mitigate structural vibration. In this paper, we are applying the sliding mode control (SMC) method to enhance the damping capacity of passive TLMCDs. SMC is a widely used nonlinear control method, which is constructed using the concept of Lyapunov stability. It forces the system to "slide" along a surface of the system's normal behavior, where the error exponentially converges to zero. The feedback control law is not a continuous function of time because it changes sign when the sliding surface changes sign (Edwards and Spurgeon 1998). The two objectives of this paper include two parts: (1) when the wind load is modeled as a harmonic force, the transfer function of a semi-active TLMCD attached to a SDOF structure is used to investigate the performance of a semi-active TLMCD and its comparison with passive TLMCDs and TLCDs; (2) when the wind load is modeled as stochastic pressure on the surface of a benchmark building of a 20-storey steel frame, the maximum inter-story drift ratio and the maximum acceleration is used to evaluate the effectiveness of the semi-active TLMCD mitigating structural vibration against wind hazards.

7.3 Analytical Modeling

7.3.1 Passive tuned liquid multiple column dampers

The analytical model of passive TLMCD is constructed using Lagrange equations. A N-column TLMCD is a N-1 DOFs system, where the liquid surface motion in each column is considered as an individual DOF. The liquid motion in a TLMCD is illustrated in Figure 7.1, where $\ddot{x}_g$ is the acceleration transmitted from the primary structure, x_i is the liquid surface displacement in the i^{th} column, h is the initial vertical liquid surface height, l_i is the horizontal

column spacing between the i^{th} and $i+1^{\text{th}}$ columns, η_i is the head loss coefficient of the i^{th} orifice.

The equations governing the liquid motion are:

$$\frac{\mathrm{d}}{\mathrm{d}t}\left(\frac{\partial T}{\partial \dot{x}_i}\right)-\frac{\partial T}{\partial x_i}+\frac{\partial V}{\partial x_i}=Q_{oi}+Q_{fi}+Q_{ei},\quad (i=1,2,...,N-1) \tag{7-1}$$

$$V=\frac{1}{2}\rho A\mathrm{g}\sum_{i=1}^{N}x_i^2\,, \tag{7-2a}$$

$$T=\frac{1}{2}\rho A\left\{\sum_{i=1}^{N}\dot{x}_i^2\left(h+x_i\right)+\sum_{i=1}^{N-1}\upsilon l_i\left(\sum_{j=1}^{i}\dot{x}_j\right)^2\right\} \tag{7-2b}$$

where t is time, Q_{oi}, Q_{fi}, Q_{ei} are respectively the quadratic orifice damping forces, the quadratic friction damping forces and the liquid inertia force acting on the i^{th} DOF, T and V are respectively the system's kinematic and potential energy, ρ is the liquid density, A is the vertical column's cross-section area, g is gravitational acceleration and υ is the vertical versus horizontal cross-section area ratio. Substitute Eq. (7-2) into Eq. (7-1) yields the governing equations of the liquid motion in a N-column TLMCD (Wu et al. 2017):

$$\begin{aligned}&\sum_{j=1}^{i}\left(\sum_{k=1}^{N-1}x_k-h-\sum_{k=i}^{N-1}\upsilon l_k\right)\ddot{x}_j+\sum_{j=i+1}^{N-1}\left(\sum_{k=1}^{N-1}x_k-h-\sum_{k=j}^{N-1}\upsilon l_k\right)\ddot{x}_j-\left(h+x_i\right)\ddot{x}_i+\frac{1}{2}\left(\sum_{k=1}^{N-1}\dot{x}_k\right)^2-\frac{1}{2}\dot{x}_i^2\\&-\mathrm{g}x_i-\mathrm{g}\sum_{k=1}^{N-1}x_k=\mu\left|\dot{x}_i\right|\dot{x}_i\left(h+x_i\right)+\mu\left|\sum_{k=1}^{N-1}\dot{x}_k\right|\left(\sum_{k=1}^{N-1}\dot{x}_k\right)\left(h-\sum_{k=1}^{N-1}x_k\right)+\sum_{k=i}^{N-1}\upsilon\left(\mu l_k+\frac{1}{2}\eta_k\right)\left|\sum_{j=1}^{k}\dot{x}_j\right|\sum_{j=1}^{k}\dot{x}_j\\&+\ddot{x}_g\left(t\right)\sum_{k=i}^{N-1}l_k,\ \left(i=1,2,...,N-1\right)\end{aligned} \tag{7-3}$$

The above model is difficult to solve, and the vibration modes are unclear since the mass, stiffness and damping matrices are all nonlinear. A simplification method is needed. In TLMCD design, the geometry is often designed as symmetric, i.e., column spacings and the orifices are mirrored about the central line, because the seismic or wind load can happen in

either direction. For these TLMCDs, the liquid motion under random stationary excitations are symmetric as well. By simply assuming symmetricity, the number of DOFs in a N-column symmetrical TLMCD can be reduced from *N*-1 to *N*/2, and the governing equations are greatly simplified, as shown in Eq. (7-4). The only nonlinear terms in these equations are the quadratic damping forces.

$$\mathbf{M}_C\ddot{\mathbf{x}}+\mathbf{C}_C\mathbf{v}+\mathbf{K}_C\mathbf{x}=\boldsymbol{\alpha}\ddot{x}_g \tag{7-4}$$

where $\mathbf{x}=\begin{bmatrix}x_1 & x_2 & \cdots & x_{N/2}\end{bmatrix}^T$, $\ddot{\mathbf{x}}=\begin{bmatrix}\ddot{x}_1 & \ddot{x}_2 & \cdots & \ddot{x}_{N/2}\end{bmatrix}^T$,

$\mathbf{v}=\begin{bmatrix}|\dot{x}_1|\dot{x}_1 & |\dot{x}_2|\dot{x}_2 & |\dot{x}_3|\dot{x}_3 & \cdots & |\dot{x}_{N/2}|\dot{x}_{N/2}\end{bmatrix}$,

$$\mathbf{M}_C=\rho A\begin{bmatrix}\upsilon\left(2\sum_{k=1}^{N/2}l_k-l_{N/2}\right)+2h & \upsilon\left(2\sum_{k=2}^{N/2}l_k-l_{N/2}\right) & \upsilon\left(2\sum_{k=3}^{N/2}l_k-l_{N/2}\right) & \cdots & \upsilon l_{N/2}\\ \upsilon\left(2\sum_{k=2}^{N/2}l_k-l_{N/2}\right) & \upsilon\left(2\sum_{k=2}^{N/2}l_k-l_{N/2}\right)+2h & \upsilon\left(2\sum_{k=3}^{N/2}l_k-l_{N/2}\right) & \cdots & \upsilon l_{N/2}\\ \upsilon\left(2\sum_{k=3}^{N/2}l_k-l_{N/2}\right) & \upsilon\left(2\sum_{k=3}^{N/2}l_k-l_{N/2}\right) & \upsilon\left(2\sum_{k=2}^{N/2}l_k-l_{N/2}\right)+2h & \cdots & \upsilon l_{N/2}\\ \vdots & \vdots & \vdots & \ddots & \vdots\\ \upsilon l_{N/2} & \upsilon l_{N/2} & \upsilon l_{N/2} & \cdots & \upsilon l_{N/2}+2h\end{bmatrix}_{N/2\times N/2},$$

$$\mathbf{K}_C=\rho A\begin{bmatrix}2\mathrm{g} & 0 & \cdots & 0\\ 0 & 2\mathrm{g} & \cdots & 0\\ \vdots & \vdots & \ddots & \vdots\\ 0 & 0 & \cdots & 2\mathrm{g}\end{bmatrix}_{N/2\times N/2},$$

$$\mathbf{C}_C=\rho A\begin{bmatrix}2\upsilon(\eta_1+\mu l_1)+2\mu h & 2\upsilon(\eta_2+\mu l_2) & 2\upsilon(\eta_3+\mu l_3) & \cdots & \upsilon(\eta_{N/2}+\mu l_{N/2})\\ 0 & 2\upsilon(\eta_2+\mu l_2)+2\mu h & 2\upsilon(\eta_3+\mu l_3) & \cdots & \upsilon(\eta_{N/2}+\mu l_{N/2})\\ 0 & 0 & 2\upsilon(\eta_3+\mu l_3)+2\mu h & \cdots & \upsilon(\eta_{N/2}+\mu l_{N/2})\\ \vdots & \vdots & \vdots & \ddots & \vdots\\ 0 & 0 & 0 & \cdots & \upsilon(\eta_{N/2}+\mu l_{N/2})+2\mu h\end{bmatrix}_{N/2\times N/2},$$

$$\boldsymbol{\alpha}=\begin{bmatrix}2\left(\sum_{i=1}^{N/2}l_i\right)-l_{N/2} & 2\left(\sum_{i=2}^{N/2}l_i\right)-l_{N/2} & 2\left(\sum_{i=3}^{N/2}l_i\right)-l_{N/2} & \cdots & l_{N/2}\end{bmatrix}^T.$$

7.3.2 Semi-active tuned liquid multiple column dampers

The control force **u** of the semi-active TLMCD proposed in this paper is provided by the orifice damping force. Consider the equation of motion for an n-story building equipped with n_d-column semi-active TLMCD on the top, the equations of motion are expressed below:

$$\mathbf{M}\ddot{\mathbf{x}} + \mathbf{C}\dot{\mathbf{x}} + \mathbf{K}\mathbf{x} = -\mathbf{M}\mathbf{B}_g a_g + \mathbf{B}_f \mathbf{F} + \mathbf{B}_u \mathbf{u} \tag{7-5}$$

where $\mathbf{M} = \begin{bmatrix} \mathbf{M}_C & \vdots & \boldsymbol{\alpha} & \mathbf{0} \\ \cdots & \cdots & \cdots & \cdots \\ \boldsymbol{\alpha} & \vdots & \begin{bmatrix} m_d & \cdots & 0 \\ \vdots & \ddots & \vdots \\ 0 & \cdots & 0 \end{bmatrix} + \mathbf{M}_S \\ \mathbf{0} & & \end{bmatrix}$, $\mathbf{C} = \begin{bmatrix} \mathbf{0} & \mathbf{0} \\ \mathbf{0} & \mathbf{C}_S \end{bmatrix} \begin{bmatrix} \dot{\mathbf{x}} \\ \dot{\mathbf{x}}_s \end{bmatrix}$, $\mathbf{K} = \begin{bmatrix} \mathbf{K}_C & \mathbf{0} \\ \mathbf{0} & \mathbf{K}_S \end{bmatrix}$,

$\mathbf{x} \in \mathbb{R}^{(\mathrm{n}+\mathrm{n}_d)\times 1}$ is the displacement vector, $\mathbf{E}_g \in \mathbb{R}^{(n_d+n)\times 1}$, $\mathbf{E}_f \in \mathbb{R}^{(n_d+n)\times 1}$ and $\mathbf{E}_u \in \mathbb{R}^{(n_d+n)\times n_d}$ are the location matrices for the acceleration input a_g, force loading input vector $\mathbf{F} \in \mathbb{R}^{n\times 1}$, and control force input vector $\mathbf{u} \in \mathbb{R}^{n_d \times 1}$, respectively, $\mathbf{M}_S \in \mathbb{R}^{(n_d+n)\times(n_d+n)}$, $\mathbf{C}_S \in \mathbb{R}^{(\mathrm{n}+\mathrm{n}_d)\times(\mathrm{n}+\mathrm{n}_d)}$, and $\mathbf{K}_S \in \mathbb{R}^{(n_d+n)\times(n_d+n)}$ are the primary structure mass, damping, and stiffness matrices, and $\mathbf{M} \in \mathbb{R}^{(n_d+n)\times(n_d+n)}$, $\mathbf{C} \in \mathbb{R}^{(\mathrm{n}+\mathrm{n}_d)\times(\mathrm{n}+\mathrm{n}_d)}$, and $\mathbf{K} \in \mathbb{R}^{(n_d+n)\times(n_d+n)}$ are the system mass, damping, and stiffness matrices, respectively. The control forces **u** are the liquid damping forces controlled by controllable valves.

The state-space representation of Eq. (3.1) is given by

$$\dot{\mathbf{X}} = \mathbf{A}\mathbf{X} + \mathbf{B}_g a_g + \mathbf{B}_f \mathbf{F} + \mathbf{B}_u \mathbf{u} \tag{7-6}$$

where $\mathbf{X} = \begin{bmatrix} \mathbf{x} & \dot{\mathbf{x}} \end{bmatrix} \in \mathbb{R}^{2(n_d+n)\times 1}$ is state vector and the constant coefficient matrices are defined as follows

$$\mathbf{A}=\begin{bmatrix}\mathbf{0} & \mathbf{I}\\ \mathbf{-M^{-1}K} & \mathbf{-M^{-1}C}\end{bmatrix}_{2(n+n_d)\times 2(n+n_d)};\ \mathbf{B}_g=\begin{bmatrix}\mathbf{0}\\ \mathbf{-E}_g\end{bmatrix}_{(n+n_d)\times 1};\tag{7-7}$$

$$\mathbf{B}_f=\begin{bmatrix}\mathbf{0}\\ \mathbf{M}^{-1}\mathbf{E}_f\end{bmatrix}_{(n+n_d)\times n};\ \text{and}\ \mathbf{B}_u=\begin{bmatrix}\mathbf{0}\\ \mathbf{M}^{-1}\mathbf{E}_u\end{bmatrix}_{(n+n_d)\times n_d}$$

The numerical algorithm has the discrete form of the Duhamel integral:

$$\mathbf{X}(t+\Delta t)=e^{\mathbf{A}\Delta t}\mathbf{X}(t)+\mathbf{A}^{-1}(e^{\mathbf{A}\Delta t}-\mathbf{I})\left[\mathbf{B}_g a_g(t)+\mathbf{B}_f\mathbf{F}(t)+\mathbf{B}_u\mathbf{u}(t)\right]\tag{7-8}$$

where Δt is the simulation time interval and $\mathbf{I}\in\mathbb{R}^{2(n+n_d)\times 2(n+n_d)}$ is the identity matrix. The required control force $\mathbf{u}_{req}$ for the damper is computed based on a sliding model controller (SMC) assuming full-state feedback.

7.4 Control Methodology

In the semi-active control algorithm, the damping forces of the semi-active TLMCD is viewed as the control forces. The orifice blocking ratio ψ and the orifice head loss coefficient damping η has the following relationship (Idelchik and Fried 1986):

$$\eta=\left(\psi+0.707\psi^{0.375}\right)^2\left(1-\psi\right)^{-2}\tag{7-9}$$

Hence, the blocking ratios of the controllable valves can be determined by the required orifice head loss coefficients, which are further determined by the required control force $\mathbf{u}_{req}$. The minimum and maximum blocking ratios for the controllable valves are 0%, 90% respectively. As a result, if the required control forces exceed the maximum damping forced that can be provided by the valves, the required control forces are set to a cap value, which equals to the damping forces when the valves are 90% blocked.

The slide mode control (SMC) algorithm is used in this study to determine the control forces provided by the orifices. First, a sliding mode controller is established by defining a sliding surface $\mathbf{S}\in\mathbb{R}^{n_d\times 1}$

$$\mathbf{S} = \mathbf{PX} = \mathbf{0} \tag{7-10}$$

where $\mathbf{P} \in \mathbb{R}^{2(n+n_d)\times n_d}$ is a user-defined weight matrix to be determined such that the motion on the sliding surface is stable. A Lyapunov function **V** based on the surface error is used to design such that the sliding surface $\mathbf{S} = \mathbf{0}$:

$$\mathbf{V} = \frac{1}{2}\mathbf{S^T S} \tag{7-11}$$

The sufficient condition for the sliding surface $\mathbf{S} = \mathbf{0}$ to occur as $t \to \infty$ is

$$\dot{\mathbf{V}} = \mathbf{S}^T\dot{\mathbf{S}} \le 0 \tag{7-12}$$

Substituting the state-space representation into Eq. (3.7) yields

$$\begin{aligned}\dot{\mathbf{V}} &= \mathbf{S}^T\mathbf{P}\dot{\mathbf{X}} \\ &= \mathbf{S}^T\mathbf{P}(\mathbf{AX} + \mathbf{B}_g a_g + \mathbf{B}_f\mathbf{F} + \mathbf{B}_u\mathbf{u}) \\ &= \mathbf{S}^T\mathbf{PB}_u\left[\mathbf{u} + \left(\mathbf{PB}_u\right)^{-1}\mathbf{P}(\mathbf{AX} + \mathbf{B}_g a_g + \mathbf{B}_f\mathbf{F})\right]\end{aligned} \tag{7-13}$$

Eq. (3.8) is rewritten using $\boldsymbol{\lambda}$ and $\mathbf{G}$

$$\begin{aligned}\dot{\mathbf{V}} &= \boldsymbol{\lambda}(\mathbf{u} - \mathbf{G}) \le 0 \\ &= \sum_{i=1}^{n_d}\lambda_i(\mathrm{u}_i - \mathrm{G}_i) \le 0\end{aligned} \tag{7-14}$$

with

$$\boldsymbol{\lambda} = \mathbf{S}^T\mathbf{PB}_u \text{ and } \mathbf{G} = \left(\mathbf{PB}_u\right)^{-1}\mathbf{P}(\mathbf{AX} + \mathbf{B}_g a_g + \mathbf{B}_f\mathbf{F}) \tag{7-15}$$

where λ_i, G_i and u_i is the i^{th} element of the vectors $\boldsymbol{\lambda}_{n_d\times 1}$, $\mathbf{G}_{n_d\times 1}$ and $\mathbf{u}_{n_d\times 1}$, respectively.

The required control force vector **u** is then obtained as

$$\mathbf{u}_{req} = \mathbf{G} - \boldsymbol{\Delta}\boldsymbol{\lambda}^T \tag{7-16}$$

where $\boldsymbol{\Delta}$ is the diagonal matrix with user-defined sliding margin $\delta_i > 0$ at its i^{th} diagonal element. The effectiveness of the semi-active control is determined by the selection of the weight matrix **P** and time step matrix $\boldsymbol{\Delta}$.

7.5 Mitigation of SDOF Structures against Harmonic Wind Hazard

SDOF structures refer to structures whose first vibration mode is dominant over other vibration modes. The performance of a semi-active TLMCD mitigating SDOF structures' vibration against wind load can be illustrated using transfer functions, where the input is the amplitude of external harmonic wind force acting on the SDOF structure, and the output is the amplitude of the displacement or the acceleration under that external load. Numerical simulation of the transfer function can be done by subjecting the SDOF structure into a harmonic frequency sweep force of the same amplitude (here assume the amplitude as 0.001 $M_s\, g$). The passive and the semi-active TLMCDs have the same geometry, whose undamped first natural frequency is tuned to 96% of the that of the primary structure.

Assume that a SDOF structure has a structural mass, stiffness and damping ratio of m_s = 3.86 ×10^5 kg, ω_s = 1.1 rad/s, and ξ_s = 0.02 respectively. The attached TLMCD has an equal column spacings of l_i = 5.35 m and a liquid height of h = 0.89 m. The user-defined weight matrix and time step matrix of the sliding mode control algorithm are selected as the following:

$$\mathbf{P} = \begin{bmatrix} 100 & 1 & 0 & 10 & 0 & 0 \\ 200 & 0 & 0 & 50 & 1 & 0 \end{bmatrix} \left(10^5\right),\ \Delta = [10^5 \quad 10^5], \tag{7-17}$$

A harmonic frequency sweep excitation of the amplitude 0.001$M_s\, g$ yields the transfer function of the displacement versus excitation frequency for the SDOF structure equipped with the semi-active TLMCD, as shown in Figure 7.2.

If minimizing the peak values of the transfer function of passive dampers is the optimization goal, this optimization method is called H_∞ norm type optimization. And the optimized results for the main structure equipped with both passive TLCDs and TLMCDs are

also illustrated in Figure 7.2. Comparisons between the semi-active TLMCD, its passive counterpart and the passive TLCD show: (1) The optimized passive TLMCD and TLCD only have a small difference in transfer functions, mainly because both their first natural frequencies are similar and tuned to that of the main structure; (2) The semi-active TLMCD has a much better mitigation effect than the passive TLMCD, and the maximum displacement amplitude decreased by 18% due to the controlled damping forces. A sharp turn around the frequency ratio of 1 is observed in the transfer function curve.

The same method is applied to study the transfer function of maximum acceleration versus frequency for the main SDOF structure equipped with semi-active TLMCD. The comparison between the semi-active TLMCD, its passive counterpart and the passive TLCD is illustrated in Figure 7.3. A significant reduction of the main structure's displacement is achieved by equipping the semi-active TLMCD.

To better understand the mechanism of the semi-active TLMCD, the time series of the actual control forces provided by the orifice head loss, the required control force and the maximum control forces are shown in Figure 7.4. As mentioned in the last section, the blocked ratio limit of the controllable valves is set as 90%, the maximum control forces are acquired by the head loss coefficient corresponding to 90% valves blocking ratio and the actual liquid velocity at the valves. From the comparison results, it is noted that the actual control forces are in the same phase of the required control forces, though at a much smaller amplitude. The actual control forces are approximately 70% of their maximum limit, corresponding to an 81% blocking ratio of the valves at its largest.

7.6 Mitigation of MDOF Structures against Stochastic Wind Hazard

In this section we conduct numerical simulation on a 20-story primary building attached with semi-active TLMCDs for mitigation of stochastic wind hazard.

7.6.1 Primary building

A steel moment-resisting frame residential building, located in Los Angeles, CA, is selected to demonstrate the effect of semi-active TLMCD mitigating wind hazard. After obtaining the modal parameters, this building is modeled as a lumped-mass shear system with dynamic properties listed in Table 7-1. The inherent structural damping ratio of the first vibration mode is assumed to be ξ_s = 0.02. This simplified lumped-mass model is used to evaluate stochastic dynamic response controlled by a semi-active TLMCD based on the assumption that wind loading is applied on the discrete lumped masses at each floor, as illustrated in Figure 7.5. The effectiveness of vibration reduction by three types of liquid dampers including a semi-active TLMCD, a passive TLMCD and a passive TLCD are examined; in all three cases, the total mass of the damper is set as 1% of that of the primary structure.

7.6.2 Wind load

We adopt the wind load model from Simiu and Scanlan (1996) to simulate the stochastic wind hazard on the benchmark structure. The simulation of the time-varying wind load can be summarized as the following. The wind flow can be viewed as a combination of a steady component and a fluctuating wind component. The wind force acting on the lateral surface is given by

$$P_d(t) = \frac{1}{2}\rho C_d A\left(V + v(t)\right)^2 \tag{7-18}$$

where C_d is the drag coefficient, ρ is the air density, A is the distributed area exposed to the wind pressure, V is the mean wind speed, and $v(t)$ is the fluctuation of wind flow around its mean wind speed V.

The design value for steady component V is computed from a 3-second wind gust speed V_0 that can be obtained from wind hazard maps (ASCE-7, 2010):

$$V = 0.13V_0 \frac{v_*}{v_{*0}} \ln\left(z / z_*\right) \tag{7-19}$$

where z_* is the surface roughness length of the building's terrain, V_0 is the 3-second wind gust design speed, and v_* and v_{*0} are the shear velocities of wind flow of the building and open terrain, respectively.

The wind fluctuation $v(t)$ at the height z is modeled as a stochastic process characterized by the following power spectral density function (PSD) at the excitation frequency of Ω (Simiu and Scanlan 1996), which can further be numerically simulated as a zero-mean Gaussian stationary process:

$$S_v\left(z,\Omega\right) = \frac{1}{2}\frac{200}{2\pi} v_*^2 \frac{z}{V}\left[1+50\frac{\Omega z}{2\pi V}\right]^{-\frac{5}{3}} \tag{7-20}$$

The wind loading parameters are determined based on the building location's terrain and the wind hazard map in ASCE 7-10 (2010). The following parameters are used in the wind load simulation: the ratio of shear velocity of wind flow v_*/ v_{*0} = 1.15, the surface roughness length z_* = 0.3 m, the air density ρ =1.229 kg/m^3, the basic wind speed selected with a 3-second gust speed at a reference height of 10 m and at a return period of 50 years V_0 = 38 m/s, and the drag coefficient C_d = 1.4. The total area exposed to wind pressure at each floor is A = 210 m^2.

Based on the above parameters, the mean static wind load at the top of the building is calculated to be P_n =1.86 × 10^5 N.

7.6.3 Inter-story drifts

The inter-story drift ratios, which is defined as the displacement different of a floor and ceiling divided by the story height, are illustrated in the Figure 7.6. The inter-story drift ratio is the largest at the first floor and gradually decrease with the floor number. This trend corresponds to the shear forces acting on each floor due to the wind loads.

From the comparison between the passive TLCD, the passive TLMCD and the semi-active TLMCD, it is found that the semi-active TLMCD has the lowest average inter-story drift ratio, while the passive TLCD and the passive TLMCD are comparable. The average decrease of inter-story drift ratios at all floors compared to the uncontrolled structure is 13% for the semi-active case, while the reduction percentages of the inter-story drift for the passive TLCD and TLMCD are 9.8% and 9.6%, respectively. Considering that the semi-active TLMCD has only 1% of the total mass of the structure, the damping effect is significant.

7.6.4 Maximum acceleration

One of the most significant factor that impacts the comfortability of living inside a high-rise building is the acceleration amplitude. An overlarge acceleration will cause the occupants great discomfort. Here we compare the maximum accelerations at each floor when the 20-story building is equipped with the passive TLCD, the passive 4-column TLMCD and the semi-active 4-column TLMCD, respectively, as illustrated with Figure 7.7. From the acceleration distribution across the building height, it is found that the vibration of the building is dominated by its first vibration mode. The maximum acceleration generally increases with the floor number, with the highest acceleration at the top of the building. The semi-active TLMCD still achieves the largest decrease of average acceleration amplitude reduction for the high-rise building, though at high levels the damping effect of all the three

types of liquid dampers are similar. The semi-active design performances the best at the 6-10 floors of the building.

7.7 Conclusions

This paper investigates the mitigation effect of semi-active TLMCD on tall buildings against wind hazard. The semi-active TLMCD is controlled by liquid damping forces controlled by internal openable valves in the horizontal column of the TLMCD.

First, when wind load is modeled as a harmonic force acting on the main structure, transfer functions can be used to evaluate the damping performance of semi-active TLMCDs. The transfer function of displacement and acceleration amplitude versus excitation frequency show that a semi-active TLMCD has a much better damping capacity compared to its passive counterpart or a passive TLCD. The semi-active TLMCD can lower the maximum structure displacement by 26% compared to the passive case.

Next, a 20-story building, modeled as a lumped mass system, is equipped with a semi-active TLMCD at the top of the building. Stochastic wind pressure on each floor is applied corresponding to its height. Numerical simulations of the building's response under the wind pressure evaluate both the inter-story drift ratio and the maximum acceleration at each floor. The results show that the semi-active TLMCD can lower the average building inter-story drift ratio by 13%, considerably larger than its passive counterpart or a passive TLCD. The comparison of maximum acceleration reduction also has a similar result for the three types of dampers. Since external power needed for control of the internal valves is small and the achieved damping effect is significant, semi-active TLMCDs can be considered as an economical and safe option when a liquid damper is needed to mitigate wind hazard on tall buildings.

7.8 References

ASCE-7, 2010. Minimum Design Loads for Buildings and Other Structures, American Society of Civil Engineering, Reston, VA, asce/sei 7-10 edition.

Chakraborty, S., Debbarma, R., Marano, G.C., 2012. Performance of tuned liquid column dampers considering maximum liquid motion in seismic vibration control of structures. J. Sound Vib. 331, 1519–1531. https://doi.org/10.1016/j.jsv.2011.11.029

Chen, Y.H., Ko, C.H., 2003. Active tuned liquid column damper with propellers. Earthq. Eng. Struct. Dyn. 32, 1627–1638. https://doi.org/10.1002/eqe.295

Connor J., Laflamme, S., 2014. Structural motion engineering, Springer, New York.

Coudurier, C., Lepreux, O., Petit, N., 2015. Passive and semi-active control of an offshore floating wind turbine using a tuned liquid column damper. IFAC-PapersOnLine 28, 241–247. https://doi.org/10.1016/j.ifacol.2015.10.287

Edwards, C., and Spurgeon, S., 1998. Sliding mode control: theory and applications. Crc Press, London.

Idelchik E., Fried E., 1986. Handbook of hydraulic resistance (2nd Ed), Hemisphere Publishing Corp., Washington DC.

Sakai, F., Takaeda, S., Tamaki, T., 1989. Tuned liquid column damper-new type device for suppression of building vibrations, Int. Conf. on Highrise Buildings, 25-27.

Shinozuka, M., Constantinou, M. C., Ghanem, R., 1992. Passive and active fluid dampers in structural applications. In Proc. US/China/Japan Workshop on Struct. Control, 507-516.

Simiu E., Scanlan R. H., 1996. Wind effects on structures: fundamentals and applications to design. Wiley, New York.

Sun, H.X., Wang, X.Y., 2016. An investigation on a semi-active magnetorheological tuned liquid column damper (MR-TLCD) 979933, 979933.https://doi.org/10.1117/12.2222152

Symans, M.D., Constantinou, M.C., 1999. Semi-active control systems for seismic protection of structures: A state-of-the-art review. Eng. Struct. 21, 469–487. https://doi.org/10.1016/S0141-0296(97)00225-3

Wang, J.Y., Ni, Y.Q., Ko, J.M., Spencer, B.F., 2005. Magneto-rheological tuned liquid column dampers (MR-TLCDs) for vibration mitigation of tall buildings: Modelling and analysis of open-loop control. Comput. Struct. 83, 2023–2034. https://doi.org/10.1016/j.compstruc.2005.03.011

Wu, H., Cao, L., Chen, A., Laflamme, S., 2017. A novel tuned liquid wall damper for multi-hazard mitigation. SPIE Smart Structures and Materials+ Nondestructive Evaluation and Health Monitoring, International Society for Optics and Photonics, 1016433-1016433

Yalla, S.K., Kareem, A., Kantor, J.C., 2001. Semi-active tuned liquid column dampers for vibration control of structures. Eng. Struct. 23, 1469–1479. https://doi.org/10.1016/S0141-0296(01)00047-5

Yalla, S.K., Kareem, A., 2003. Semiactive Tuned Liquid Column Dampers: Experimental Study. J. Struct. Eng. 129, 960–971. https://doi.org/10.1061/(ASCE)0733-9445(2003)129:7(960)

Table 7.1 *Dynamic properties of a 20-story building model*

floor	height (m)	mass (kg)	stiffness (kN/m)	floor	height (m)	mass (kg)	stiffness (kN/m)
20		563,000	100,576	10	3.96	552,000	265,888
19	3.96	552,000	133,952	9	3.96	552,000	270,592
18	3.96	552,000	164,416	8	3.96	552,000	273,952
17	3.96	552,000	178,752	7	3.96	552,000	277,088
16	3.96	552,000	197,568	6	3.96	552,000	279,552
15	3.96	552,000	200,928	5	3.96	552,000	275,072
14	3.96	552,000	203,392	4	3.96	552,000	297,920
13	3.96	552,000	232,064	3	3.96	552,000	299,712
12	3.96	552,000	236,096	2	3.96	552,000	304,192
11	3.96	552,000	244,832	1	5.49	584,000	225,568

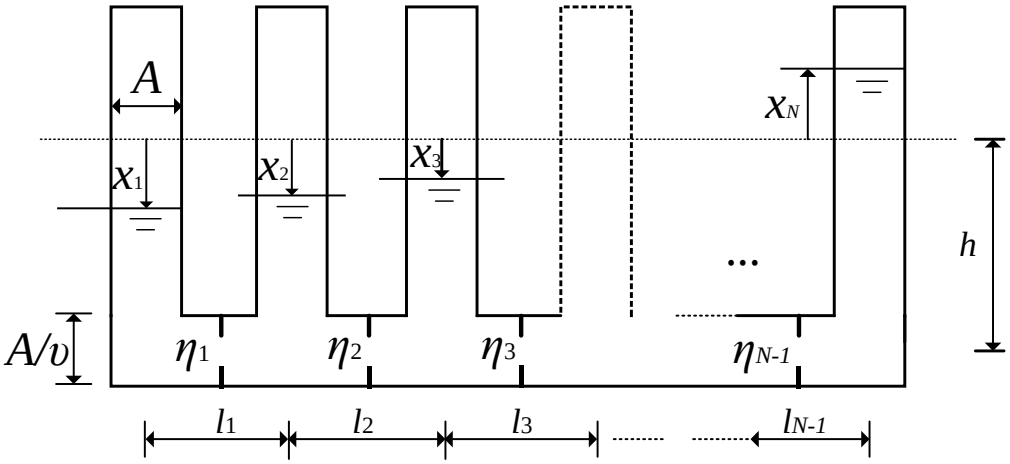

Figure 7.1 *Schematic drawing of a N-column TLMCD*

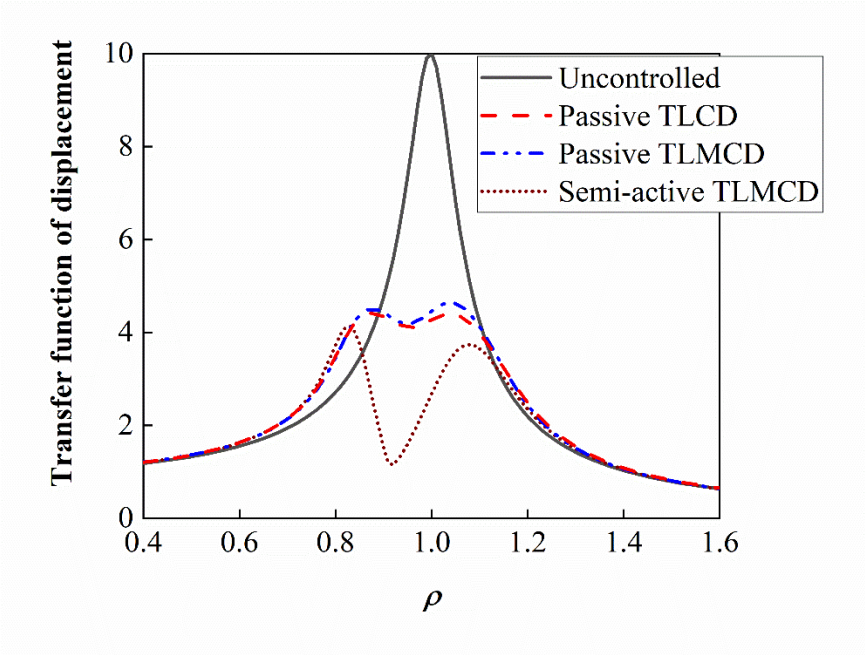

Figure 7.2 *Transfer function of the main structure's maximum displacement versus excitation frequency ratio*

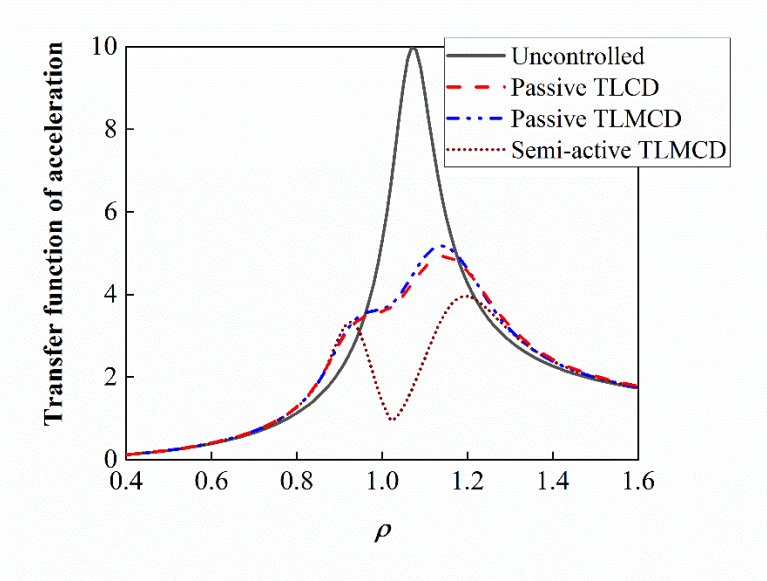

Figure 7.3 *Transfer function of the main structure's maximum acceleration versus excitation frequency ratio*

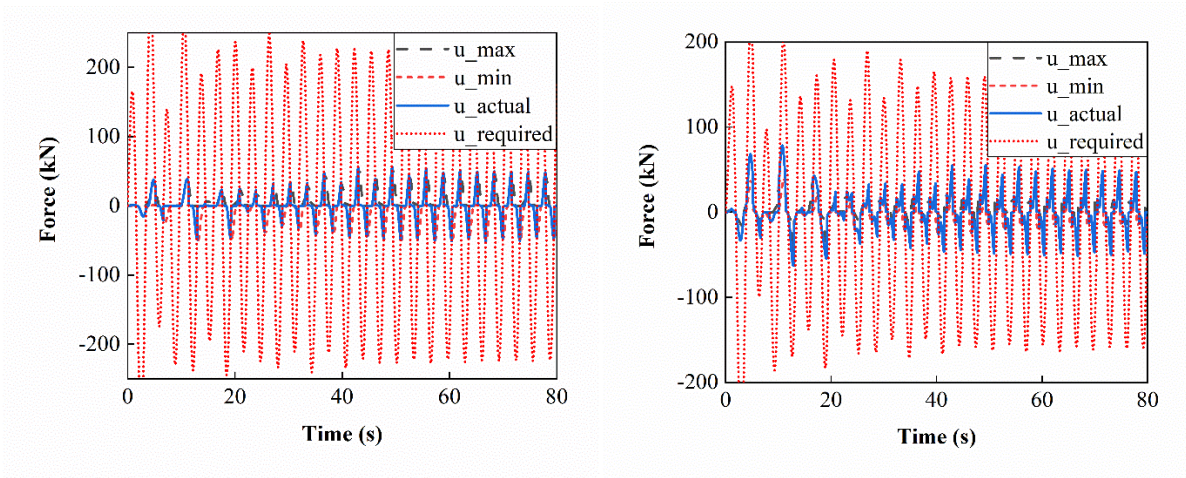

(a) (b)

Figure 7.4 *The actual control force, the maximum available control force, and the required control force for semi-active TLMCD (a) at the first orifice (b) at the second orifice.*

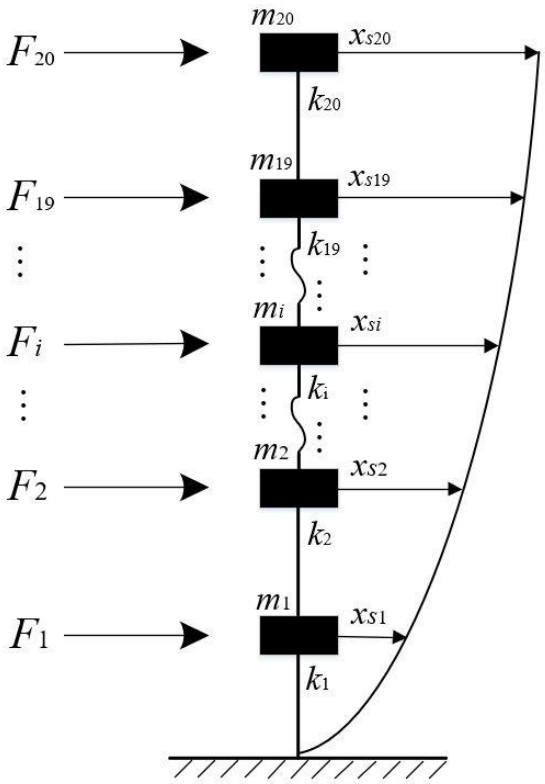

Figure 7.5 *Wind load on lumped-mass model of a 20-DOF structure*

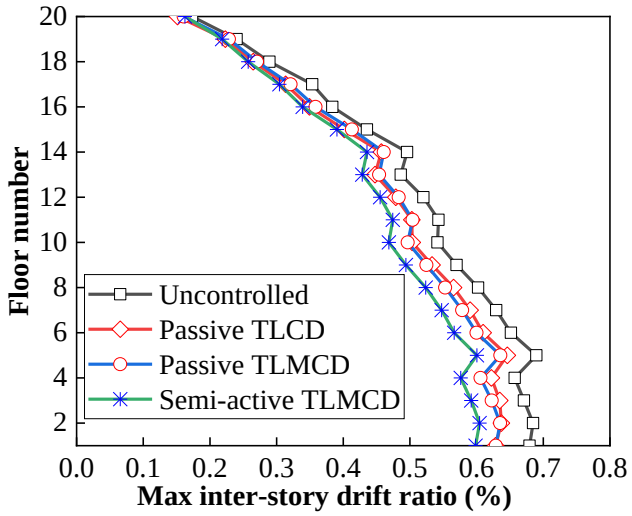

Figure 7.6 *The inter-story drift ratio of the 20-story prototype building*

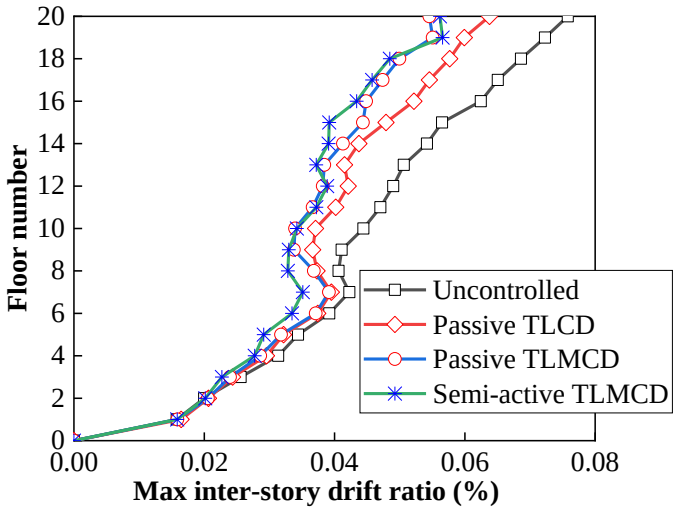

Figure 7.7 *The max acceleration amplitude of the 20-story prototype building*

CHAPTER 8. CONCLUSIONS AND FUTURE WORK

In this dissertation, a novel multifunctional panel that integrals structural load bearing, thermal exchange and storage, and vibration mitigation against wind or earthquake hazards is presented. The multifunctional panel consists a structural wall with multiple capillaries that are filled with liquid, which can adjust building temperature as well as provide supplemental damping against seismic or wind hazards. The main objective of this study is to assess the structural damping capability of this type of panels.

8.1 Summary for Major Conclusions

8.1.1 Multifunctional GFRP panel

One of the potential ways to manufacture multifunctional panels is using pultruded GFRP. Pultruded GFRP is strong and light and can easily make structural panels of various hollow sections.

In Chapter 2, the dynamic load resistance of the multi-celled pultruded GFRP panel is evaluated using comprehensive shake table tests. A steel block is attached on the top of the panel to simulate the supported seismic mass. Test results show that the GFRP panel can sustain a peak ground acceleration of 2.1 g without being damaged. FEA analysis also shows that GFRP panels have comparable drifts and stress levels as solid reinforced concrete walls when they function as shear walls in low-rise buildings. The low stiffness of GFRP walls is compensated by its low self-weight and elastic behavior. However, due to the lightweight and elastic behavior, the multi-celled GFRP panels may have good potentials in seismic regions.

In Chapter 3, we find that the multi-celled GFRP panel can be easily adapted to include a liquid damping system by cutting out part of the cell separations, which allows free

liquid exchange between the cells. GFRP panels have elastic behavior and high strength, but the hysteretic curves under seismic load show that they have low energy dissipation capability. Shake table tests are conducted to measure the vibration reduction percentage of the GFRP panels when different combinations of cells are utilized. Comparisons show that the GFRP panel can reduce its steady vibration amplitude by as much as 26% due to the liquid motion. Generally, the reduction percentage increases with the total liquid volume inside the panel. The liquid damping forces are calculated by approximating the liquid system to a TLCD, which is further verified by CFD simulations. This shake table test concludes that it is viable to include liquid in a multi-celled structure to increase its damping.

8.1.2 Analytical modeling of TLMCDs

The physical model for the internal liquid damping system in a multi-capillary/multi-celled structure is termed as tuned liquid multiple columns damper (TLMCD). The analysis of this model reveals that a TLMCD may have several advantages over classical TLCDs.

In Chapter 4, a nonlinear dynamic model for a TLMCD is constructed using Lagrange equations where the liquid surface movement in each capillary is modeled as an individual DOF. Both the friction and orifice viscous damping forces are considered in the model. Numerical solutions of the liquid surface movements under both free vibration and forced harmonic vibration are validated by CFD simulations. Parametric studies of the nonlinear model show that there exists optimum orifice damping coefficients for a TLMCD. A numerical procedure to design a TLMCD for a SDOF structure is provided. The results show that a TLMCD does not perform better than a TLCD with the same mass. But under the same geometry size, the TLMCD has a larger damping effect since it makes better use of the limited occupying space due to more vertical columns.

In Chapter 6, a linearization method for the nonlinear analytical model of TLMCD is presented. With the linearized model, the TLMCD-structure system becomes a linear system that can be optimized using the H_∞ norm method. Genetic algorithm is employed to search the optimum parameters of a TLMCD that will result in the minimum H_∞ norm. Comparing to classical TLCDs with the same mass, TLMCDs perform slightly worse in suppressing the vibrations of SDOF structures, with only less than 5% difference. For MDOF primary structures, a TLMCD could outperform single TLCD and multiple TLCDs of optimized ratio under the same length ratio restriction. This can be explained by the fact that a TLMCD can have larger effective masses at various vibration modes than multiple TLCDs.

In Chapter 7, the orifices of a TLMCD are replaced by controllable valves, making the TLMCD a semi-active device. Sliding mode control method is used to determine the control forces in TLMCDs. Significant improvement on the damping capability is achieved when the controllable valves are installed compared to the passive case through transfer function analysis under harmonic wind load. Stochastic wind loads are simulated on a 20-storey building with a semi-active TLMCD of 1 % of the structure's total mass installed on the top. The average inter-story drifts are reduced by more than 30% from the installed semi-active TLMCD when compared with passive TLMCDs or passive TLCDs.

8.1.3 Reinforced concrete multifunctional panel dynamic test

In Chapter 5, a reinforced concrete multifunctional panel was manufactured to validate the analytical models presented in Chapter 4. A plastic 6-column tube was embedded in the reinforced concrete panel to represent the TLMCD damping system. Free vibration tests of the liquid motion inside the plastic tube show similar results to numerical solutions. The concrete panel is linked to a fixed base by steel springs to form a SDOF system.

Dynamic tests results show that an internal TLMCD with a mass ratio of 1.7% can increase the reinforced concrete multifunctional panel's damping ratio from 1.51% to 1.64%.

Both the GFRP panel and the reinforced concrete multifunctional panels can be viable solutions for buildings against seismic or wind hazards. GFRP panels has larger internal space, and thus they provide better mitigation effect by including higher amount of liquid. Reinforced concrete panels have stronger stiffnesses and can be applied in medium or high-rise buildings. A simple comparison of the two types of panels' damping capability is illustrated in Table 8.1. The increased equivalent damping ratio is estimated by comparing the amplitudes of primary structures' vibration at resonance.

Table 8.1 *Comparison of the damping capability of GFRP panels and reinforced concrete panels*

Per unit length (1 m) of wall	GFRP Panel	Reinforced Concrete Panel
Maximum included water (kg)	45.4	8.90
Increased equivalent damping ratio for main structures	0.32%	0.063%

8.2 Recommended Future Work

8.2.1 Robustness analysis

In design of TLMCDs, uncertainties including external loads, structural characteristics of the main structure exist. Thus, sensitivity of these factors on the TLMCD-structure system needs to be analyzed. It is possible that the multiple frequencies of a TLMCD will result in as an effective frequency range, where the natural frequency of the primary system is considered safe.

8.2.2 Capillary arrangement in different directions

This study only considers all the capillaries of the multifunctional panel arranged in the one direction. However, in a building system, multifunctional panels might be in different directions, and even intersection of panels can happen. A TLMCD with columns in different directions can be constructed using Lagrange equations as well. Interactions between liquid vibration in different directions will be a topic worth investigating.

8.2.3 Experimental study on semi-active TLMCDs

An experimental investigation of a semi-active TLMCD is necessary to verify the conclusions drew in Chapter 7. The control strategy will be decided by how the controllable valves function. It will be interesting to compare the continuously changing valves and open/closed dual-state valves in the experiments.